

The Key Laboratory of Weak Light Nonlinear Photonics,
Ministry of Education

Annual Report 2013



南开大学弱光非线性光子学
教育部重点实验室

Annual Report 2013

The Key Laboratory of Weak Light Nonlinear Photonics,
Ministry of Education

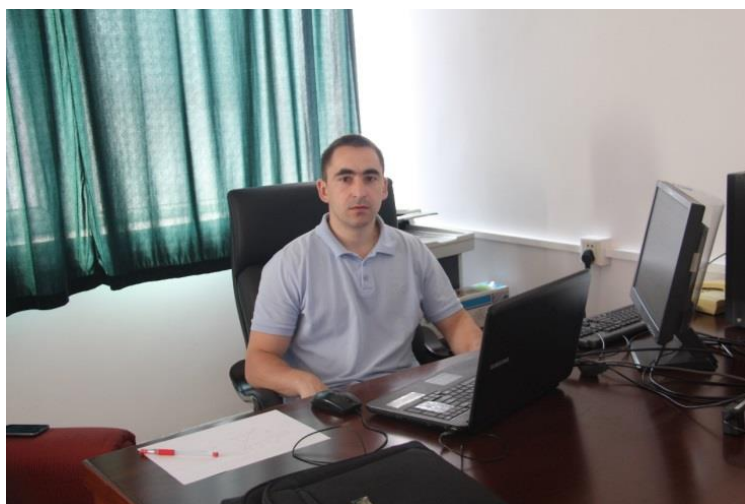


南开大学弱光非线性光子学
教育部重点实验室

▼ 教授部海外名师、德国奥斯纳布吕克大学 (Osnabrück University) 的 Peter Hertel 教授来华工作，在泰达应用物理学院和物理科学学院分别为研究生授课。 (2013.4.25-6.5)



▼ 乌克兰 Misha Gavrylyak 博士以博士后身份来弱光非线性光子学教育部重点实验室进行科研工作。 (2013.4.5-7.3)



▼ 卢布雅尔那大学 Lucija Coga 博士来弱光非线性光子学教育部重点实验室交流学习，与实验室学生进行讨论并进行了相关实验工作。 (2013.5.18-6.1)



▼ 泰达应用物理学院与物理科学学院举办南开首届物理学夏令营。 (2013.7.24-7.26)



▼ 德国 Osnabruck 大学研究生 Juliane Andrea Tschentscher 和 Pia Baeume 来弱光非线性光子学教育部重点实验室开展合作研究。 (2013.9.3-9.30)



▼ 乌克兰国家科学院 Andriy Ilyin 研究员来弱光非线性光子学教育部重点实验室进行访问和合作研究，来访期间应邀在天津理工大学作学术报告。 (2013.10.12-11.9)



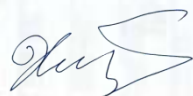
前 言/Preface

In 2013, the research mainstream at our lab was a more bit transferred to optical nonlinearities of optical microstructure systems and their applications in nonlinear optical manipulation of light. Especially this year we continue to achieve fruitful results in the novel nonlinear optical effects and their applications of the micro-structure optical systems. In addition, the national key project led by Prof. Huitian Wang has started this year, and the combinations of the optical field manipulation and the interaction between light and matter specifically optical microstructure materials has pushed a lot on our research in new nonlinear optics. And also some new members, such as Dr. Xiangfeng Zhou, Dr. Yi Hu et al, joined our lab. They surely will bring more fresh air into the lab. In this report, we present a short summary of our annual research progress in each line of activity.

All the activities summarized here have been done in the frame of international projects, cooperation agreements, and contracts with NSFC, MOE, MOST and Tianjin Municipal government. We also benefit a lot from our colleagues from other units all over world, who provide us advices and supports. Many thanks for their kind supports. In addition, our staff and students worked hard in order to make our research better and faster. Thanks a lot for their contributions and congratulations on their research achievements.

Hereby I would also like to stress that our lab is a happy family for all of us. We should keep our own excellent tradition and develop our research well in the horse year.

Prof. Dr. Jingjun Xu



Director,

The Key laboratory of Weak-Light Nonlinear Photonics

目 录/Contents

人员结构/Organization	1
承担课题/Projects under Researching.....	4
仪器设备平台/Facilities	12
研究工作报告/Scientific Report.....	13
发表论文/Publications in Journal.....	61
专利/Patents	69
国际合作与交流/International Cooperation and Exchange.....	71
国内、国际会议报告/Talks at Conferences	75
学术组织与期刊任职/Academic Service	80
获奖情况/Awards & Honors.....	82
学位论文/Dissertations.....	83

人员结构/Organization

实验室主任/Director

许京军 教授

实验室副主任/Deputy Directors

张国权 教授

孙 骞 教授

学术秘书/Academical Secretary

禹宣伊 副教授

研究方向负责人/Research Group Leaders

弱光非线性及量子相干光学 许京军 教授

非线性物理与光子技术 田建国 教授

光子学材料及先进制备技术 孔勇发 教授

光谱表征及传感技术 宋 峰 教授

光场调控及其应用 王慧田 教授

学术委员会/Academic Committee

主 任/Chairman

李树深 院 士 (中国科学院半导体研究所)

委 员/Committee Members

薛其坤 院 士 (清华大学)

孙昌璞 院 士 (中国科学院理论物理研究所)

许宁生 院 士 (中山大学)

龚旗煌 院 士 (北京大学)

陆 卫 研究员 (中国科学院上海技术物理研究所)

徐现刚 教 授 (山东大学)

资 剑 教 授 (复旦大学)

申德振 研究员 (中国科学院长春光学精密机械与物理研究所)

曾和平 教 授 (华东师范大学)

田建国 教 授 (南开大学)

王慧田 教 授 (南开大学)

许京军 教 授 (南开大学)

外籍学术顾问委员

D. Kip 教 授 德国 Clausthal 工业大学

L. Hessenlink 教 授 美国斯坦福大学物理系

R. A. Rupp 教 授 奥地利维也纳大学实验物理所

T. Volk 教 授 俄罗斯国家晶体研究所

Y. Tomita 教 授 日本电气通信大学

K. A. Nelson 教 授 美国麻省理工学院

杰出人才/Intelligent Staff

教育部“长江奖励计划”特聘教授

许京军（1999） 王慧田（1999） 陈志刚（2006）

国家杰出青年基金获得者

许京军（1998） 田建国（2001） 王慧田（2003） 李宝会（2009）

教育部“优秀青年教师资助计划”入选者

张国权（2002） 宋 峰（2003）

教育部“跨世纪优秀人才培养计划”入选者

许京军（1998） 田建国（2000） 孙 骞（2001） 孔勇发（2002）

教育部“新世纪优秀人才支持计划”入选者

张国权（2004） 宋 峰（2004） 宋 智（2004） 臧维平（2005）
李宝会（2005） 孙甲明（2007） 张心正（2008） 刘智波（2009）
陈 璟（2009） 顾 兵（2010） 楼慈波（2010） 张天浩（2011）
武 莉（2011） 周向锋（2012） 陈树琪（2013） 孙 军（2013）

首批新世纪百千万人才工程国家级人选

田建国（2004）

国家海外青年学者合作研究基金获得者

陈志刚（2005）

“天津市授衔专家”称号获得者

许京军（2005） 田建国（2005）

教育部“长江学者和创新团队发展计划”创新团队基金资助

弱光非线性光子学重点实验室人员名录/Name List

研究人员/Scientific Staff (52 人)

许京军 王慧田 田建国 Romano A. Rupp 陈志刚 张国权 孔勇发 孙 骞 宋 智
 宋 峰 臧维平 李宝会 舒永春 姚江宏 赵丽娟 曹亚安 孙甲明 张天浩 李玉栋
 徐晓轩 张心正 周文远 邢晓东 禹宣伊 余 华 吴 强 孙同庆 武 莉 楼慈波
 高 峰 刘智波 李祖斌 薄 方 齐继伟 叶 青 潘雷霆 蔡 卫 陈树琪 宋道红
 孙 军 张 玲(兼) 刘士国(兼) 李 威(兼) 陈 璟 李勇男 刘宏德 王 斌
 皮 彪 任梦昕 涂成厚 周向锋 胡 毅

技术人员/Technical Staff (4 人)

陈绍林 马玉祥 张 玲 刘士国

行政人员/administrative Staff (3 人)

梁 建 李 威 唐柏权

博士生/Ph.D Students (107 人)

邓志超 姜美玲 孙腾骞 李占成 刘文玮 于 萍 郑超逸 李 毅 郜向阳 陈旭东
 李健雄 姚 筠 李志莉 赵子宇 徐 建 赵 欣 孔翔天 应翠凤 王 槿 闫卫国
 杨 阳 杨 熹 张新星 刘 敏 王 蒙 黄森鹏 赵红艳 刘艳玲 于 音 崔文静
 张 俊 刘加东 李 伟 韦 晨 王凤箫 王立超 刘建基 窦宜领 洪佩龙 徐 雷
 韩 彬 王晓杰 黄礼刚 李志向 梁 毅 王午登 谭信辉 向吟啸 梁 毅 刘鹏翊
 杨 明 陈战东 王丕东 王 垒 石 彬 潘玉松 吴玉娥 张 斌 王 萌 潘崇佩
 李存波 罗维维 张明偲 夏 峰 王 聪 张文定 翟召辉 郝志强 陈宗强 谢 楠
 吴 限 田 甜 裴子栋 郑大怀 崔 娇 李青霄 徐纪华 闫亚斌 黄绍龙 张 鹏
 张新星 韩凌云 杨金凤 易 欢 高玲玲 葛新宇 刘 悦 诸 玲 彭永进 张荣纯
 赵明天 邱文娟 于彦龙 王景声 赵丹丹 曹丽萍 郭丽梅 刘 敏 龚 亮 娄 凯
 李思龟 钱升霞 任志成 董 校 孔令军 潘 岳 刘 瑞

硕士生/M.S. Students (179 人)

刘远泽 王晓婉 王 晨 郑 宇 齐鹏飞 高承敏 辛 巍 王 鹏 王 群 刘 楠
 高 赫 杨 娜 晏 敏 赵连云 陈春晖 陈伦杰 蔚浩义 赵 芳 刘瑞雪 马晨欣
 董 斌 蒋文帅 孙骥文 曾欢欢 李文华 雷 琴 李秀霞 马 跃 周玉波 门双仁
 高 原 彭秋明 王秋明 张 阳 高少华 刘 艳 戈 进 兰子鉴 吴婷婷 李昊宇
 周 亮 田万辉 孙希鹏 郭廷珂 赵春兰 郭 昊 安双新 宛文顺 陈展耀 巨丹丹
 任爱兵 王津津 张 俊 陈贵阳 郜慧斌 韩迎东 李 琼 王文艳 彭伟华 王晓欧
 高晓梅 许鹏伟 马增红 朱 葛 金小娜 赵 妍 赵国帅 张 虹 殷 毅 张永哲
 孙 哲 马腾飞 李利明 王 杰 杨 浩 李 莹 彭景阳 马寅星 云志强 易三铭
 杨淑英 陈庆全 李文华 崔 伟 曹天祥 刘 颖 聂 伟 冀志超 廖宏艳 王世彪
 左一平 赵 丽 蒋鹏翀 郑守君 黄 明 马 睿 陈慕灵 钟海涛 孔腾飞 李 慧
 李 清 乔晓龙 甄彦赞 谢桂娟 杨亚俊 古 瑶 周舰波 卢旭岑 张 菁 侯琼琼
 王肖珩 靳亚粉 李 娜 冯正茂 吴盈颖 崔晓彤 高少华 刘 艳 刘 畅 杨金凤
 张 华 王庆通 高 露 李 芳 张芳馨 商继芳 张亚梅 姬静远 孙少君 贾翠乐
 胡 伟 王 策 落爱青 吴增娜 王晓慧 张逍遥 解雅洁 张心铭 张冠南 单 排
 要佳莹 王力伟 秦娇夷 宋亚婷 陈艳红 郝金龙 谭庆志 黎 莎 武 迪 唐 悦
 韩中兴 高 飞 郝冰雪 张会平 王雄龙 栗瑜梅 司元春 刘 犇 刘晓芳 戈 进
 兰子鉴 吴婷婷 张勇军 徐海霞 王文庆 李清连 李小静 武丽伟 吴学谦 郭 辉
 常利芬 张 荣 高旭珍 王周祥 李萍萍 冯 丹 司 宇 蔡孟强 张会会

承担课题/Projects under Researching

序号	项 目 名 称	项 目 来 源	起 止 时 间	负 责 人
1	光子束超衍射纳米加工基本原理基础研究	973 项目	2010.1-2014.12	张心正
2	超快激光与硅表面相互作用机理研究	973 项目	2012.1-2014.8	姚江宏
3	空间结构光场与微结构的线性和非线性耦合效应	973 项目	2012.1-2016.12	田建国
4	纳/微结构中光学非线性增强机理及光调控研究	973 项目	2013.1-2017.12	张国权
5	硅基杂质与缺陷发光中心的构建及器件	973 项目	2013.1-2017.12	孙甲明
6	空间飞行器长寿命关键构件制备与服役中的基础问题	973 项目子课题	2010.01-2013.12	陈 璟 李勇男
7	新颖动量和角动量光场与微结构相互作用的量子效应	973 项目子课题	2012.1-2016.8	宋智
8	减反与广谱吸收的黑硅材料研究	973 项目子课题	2012.1-2013.12	吴强
9	纳米器件制备工艺创新与应用基础研究	973 项目子课题	2012.1-2014.12	李威
10	基于等离子激元结构的材料制备与红外光电转换增强效应研究	973 项目子课题	2013.1-2017.12	宋道红

11	介观结构新型氧化物紫外 / 深紫外光电探测及器件研究	973 项目子课题	2013.1-2017.12	孔勇发
12	关联光子学微结构的非线性光学特性与调控机理研究	国家重大科学研究计划	2010.1-2014.12	田建国
13	空间结构光场的调控机理、生成技术和新颖性质	国家重点基础研究发展计划子课题	2012.01-2016.08	王慧田
14	带电聚合物链构象与静电作用的耦合机制	国家自然科学基金重大项目(南开部分)	2010.1-2013.12	李宝会
15	多相聚合物溶液体系受限于软膜内的自组装行为研究	国家自然科学基金重大研究计划培育项目	2013.1-2015.12	李宝会
16	弱光非线性光子学材料的缺陷设计与构筑	国家自然科学基金重大研究计划培育项目	2013.1-2015.12	孔勇发
17	纳米切削基础理论及相关关键技术研究	国家自然科学基金重大研究计划子课题	2010.1-2013.12	徐晓轩
18	矢量光场的动态调控: 新方法、新效应和应用	国家自然科学基金重点项目	2010.1-2013.12	王慧田
19	大功率 DUV-DPL 热效应研究	国家自然科学基金重点项目子课题	2012.1-2015.12	宋峰
20	基于微纳器件的飞秒矢量光场及其微纳结构制备研究	国家重大仪器专项项目子课题	2013.1-2016.12	李勇男
21	氧化锌铝纳米粉体及靶材中试技术研究	863 计划	2012.1-2014.12	舒永春
22	高分子物理与高分子物理化学	国家自然科学基金杰出青年科学基金	2010.1-2013.12	李宝会

23	XXX	科技部	2012.7-2015.7	宋峰
24	新型聚合物纳米复合材料及其光子学微结构研究	国家国际科技合作专项	2012.1-2014.12	张心正
25	新型乳腺癌早期预警系统的建立及防治方法的合作研究	国家国际科技合作专项	2012.6.1-2015.5.31	田建国
26	非中心对称宽禁带氧化物高压光伏效应的合作研究	国家国际科技合作专项	2013.4-2015.12	孔勇发
27	Peter Hertel (MS2010NKDX023)	教育部“海外名师”项目	2010.1-2014.12	许京军
28	Airy 光束的传输特性及在光学微粒操控中的应用研究	国家自然科学基金	2011.1-2013.12	臧维平
29	光折变表面孤子及其应用研究	国家自然科学基金	2011.1-2013.12	张天浩
30	有序与无序金属亚波长微纳结构的表面增强非线性	国家自然科学基金	2011.1-2013.12	李祖斌
31	双掺杂 TiO ₂ 基可见光催化剂二元离子协同作用的研究	国家自然科学基金	2011.1-2013.12	曹亚安
32	超快激光构造黑硅材料的光电性能优化及微观机理研究	国家自然科学基金	2011.1-2013.12	姚江宏
33	基于非线性光学表面波的可调谐长程传播表面等离子激元及其应用研究	国家自然科学基金	2012.1-2015.12	张天浩
34	碳基纳米材料超快光学非线性及其非线性光学显微成像研究	国家自然科学基金	2012.1-2015.12	刘智波

35	高增益光子晶体自发辐射增强效应及其生物传感应用	国家自然科学基金	2012.1-2015.12	周文远
36	通过非均匀随机介质体系的图像传输与成像研究	国家自然科学基金	2012.1-2015.12	张国权
37	介电纳米波导/金属纳米微结构复合体系光传输性能及其应用	国家自然科学基金	2012.1-2015.12	孙骞
38	无序非线性增益介质中光子局域化及上转换随机激光的研究	国家自然科学基金	2012.1-2015.12	张心正
39	可见光催化剂微观表面光生载流子特性的原位定量研究	国家自然科学基金	2012.1-2015.12	曹亚安
40	基于特异介质的矢量光场生成与调控	国家自然科学基金	2012.1-2015.12	陈璟
41	锂在铈酸锂晶体中的扩散行为及其应用研究	国家自然科学基金	2012.1-2014.12	孙 军
42	中俄 2012 年激光物理研讨会	国家自然科学基金	2012.1-2012.12	宋 峰
43	自适应光脉冲整形技术在电子加速中的应用研究	国家自然科学基金	2013.1-2016.12	臧维平
44	用于提高硅基太阳能电池效率的表面等离子体激元增强量子剪裁效应研究	国家自然科学基金	2013.1-2016.12	宋峰
45	基于二阶姜-泰勒效应的非中心对称磷酸盐功能晶体化合物的设计、合成、结构与性质	国家自然科学基金	2013.1-2016.12	孙同庆
46	原子层沉积稀土氧化物和硅酸盐纳米复合薄膜硅基 MOS 电致发光器件的研究	国家自然科学基金	2013.1-2016.12	孙甲明
47	飞秒矢量光场的超衍射极限微结构制备及特性研究	国家自然科学基金	2013.1-2016.12	涂成厚

48	微结构光纤表面等离子体谐振和局域场增强及其应用研究	国家自然科学基金青年基金	2011.1-2013.12	陈树琪
49	电子显微镜在等离激元光学中应用的理论研究	国家自然科学基金青年基金	2011.1-2013.12	蔡卫
50	聚合物分散液晶体系的多光子聚合超衍射加工研究	国家自然科学基金青年基金	2013.1-2015.12	李威
51	基于宽场显微荧光成像技术的一氧化氮亚硝基化修饰对激活的嗜中性粒细胞质钙调节机制的研究	国家自然科学基金青年基金	2013.1-2015.12	潘雷霆
52	抗紫外光损伤铈酸锂晶体及其应用研究	国家自然科学基金青年基金	2013.1-2015.12	刘宏德
53	Airy 光束的传播动力学调控及其应用	教育部新世纪优秀人才支持计划	2011.1-2013.12	楼慈波
54		教育部新世纪优秀人才支持计划	2012.1—2014.12	张天浩
55	光折变表面孤子及其应用研究	教育部高等学校博士点基金（博导类）	2011.1-2013.12	张天浩
56	基于非线性光学表面波的可调谐长程传播表面等离子体激元	教育部高等学校博士点基金（博导类）	2013.1-2015.12	张天浩
57	基于微结构光纤的表面等离子体谐振和局域场增强及其应用研究	教育部高等学校博士点新教师基金	2011.1-2013.12	陈树琪
58	基于光刻技术的细胞图案化控制及其数值仿真研究	教育部高等学校博士点新教师基金	2012.1-2014.12	潘雷霆
59	复合等离子体超材料非线性光学特性及其应用研究	教育部高等学校博士点新教师基金	2013.1-2015.12	程化
60	类石墨烯型光学微结构制备及光传播特性研究	教育部高等学校博士点新教师基金	2013.1-2015.12	宋道红

61	荧光增强空间分辨生物传感技术	天津市国际合作项目	2010.10-2013.9	周文远
62	基于聚合物-纳米颗粒复合材料的光子学微结构研究	天津市科技支撑计划 国际科技合作专项	2011.10-2013.9	张心正
63	基于聚合物-纳米颗粒复合材料的光子学微结构研究 (9-17)	中国与斯洛文尼亚政府间科技合作项目	2011.7-2013.6	张心正
64	激发态电子超快能量传输过程研究	中德合作科研项目	2011.1-2012.12	赵丽娟
65	低成本床旁快速诊断系统的研究与开发	天津市科技支撑计划 重点项目	2011.04-2013.09	田建国
66	基于近红外光谱的油料农作物品质快速检测的全固定式仪器研发和应用	天津市科技支撑计划 重点项目	2012.4-2015.3	徐晓轩
67	基于微结构光纤的空间分辨免疫传感技术研究	天津市自然科学基金 基础重点项目	2011.03-2013.03	周文远
68	焦场调控及其微纳结构制备研究	天津市自然科学基金 重点基金	2013.04-2016.03	李勇男
69	基于物联网的近海多参数水质分析仪及监测网络	天津市科技兴海项目	2012.1-2014.12	徐晓轩
70	云计算模式下基于手机信令的智能交通指挥与突发事件感知平台	天津市信息化项目	2012.1-2014.12	徐晓轩
71	近化学计量比掺铈铌酸锂晶体生长及铁电畴性能优化研究	天津市自然科学基金	2010.4-2013.3	刘宏德
72	楔形超声角锥驱动的光纤结构的滤波色散特性及其应用	天津市自然科学基金	2012.4-2015.3	高峰
73	矢量光场下的表面等离子共振及表面增强拉曼研究	天津市自然科学基金	2012.4-2015.3	齐继伟

74	石墨烯宽带光学非线性及其应用研究	天津市自然科学基金	2013.4-2016.3	刘智波
75	动态调控杂化超材料等离子激元诱导透明及其应用	天津市自然科学基金	2013.4-2016.3	陈树琪
76	XXX	国防基础科研计划	2012.1-2013.6	宋 峰
77	局域等离子激元微结构优化设计和表面增强应用研究	教育部重点实验室开放课题	2012.7-2014.6	王斌
78	蓝宝石晶体用高纯氧化铝委托开发技术	横向课题	2011.10-2012.12	孙 军
79	钢管制造信息化系统及管端参数测量系统的研究与开发	横向课题	2012.5-2014.10	田建国
80	电光晶体	中电 27 所	2012.3-2013.3	孙 军
81	基于 Zigbee 技术的温度传感物联网监控平台	天津大学	2012.10-2013.3	徐晓轩
82	ITO 用纳米 SnO ₂ 粉体制备方法	校企合作项目	2011.1-2013.12	舒永春
83	调 Q 晶体研制	205 所	2013.3-2013.4	孙军
84	高抗损伤电光晶体研制	中电 27 所	2013.4-2013.12	孙军
85	高纯铈酸锂的研制及原料合成	重庆四联	2013.6-2013.12	孙军
86	高温稳定性铈酸锂电光 Q 开关研制	中电 27 所	2013.4-2014.12	孙军

87	光功能晶体的缺陷调控与性能优化	中央高校基本科研业务费专项基金重大培育	2011.9-2013.6	孔勇发
88	新型稀土磷酸复盐光电功能材料的制备、结构与性质	中央高校基本科研业务费专项资金平台重大项目	2012.10-2013.9	孙同庆
89	类石墨烯型光子晶格的制备及其光传播特性研究	中央高校基本科研业务费专项基金	2011.10-2013.9	宋道红

仪器设备平台/Facilities

仪器设备名称	规格型号	购置时间
激光器工作站	899-29	2005.09
飞秒激光器	VF-T2S	2000.08
皮秒激光器	PY61	2003.11
纳秒激光器	Panther OPO	2003.11
光纤激光器	PLY-20-M	2003.11
可调频再生放大器	Spitfire F-1K	2000.04
时间分辨光谱及瞬态吸收光谱系统	Spectrapro.300i	2000.04
光谱分析仪	AQ6315A	2005.09
显微拉曼光谱仪	MKI2000	1998.09
分子速外延生长炉	Riber Compact 21T	2003.09
提拉法晶体生长炉	研制	2002.04
晶体切割研磨抛光系统	Logitech 系列	2001.06
扫描探针显微镜	Nanoscope IIIa	2006.08

注：除开放基金外，所有仪器设备均为有偿使用

研究报告/Scientific Report

非线性物理与光子技术/Nonlinear Physics and Photonics Techniques

负责人：田建国

本方向涉及石墨烯光学性质、等离子激元、超材料、光学传感、光在介质中的传播、光子带隙材料、亚波长微结构等方面。本年度发表论文 29 篇；申请或授权专利 17 项。在研课题经费 1541.5 万元。2013 年度“非线性物理与光子技术”方向主要在以下方面取得了进展：

In this field, we mainly focused on optical properties of graphene, plasmonics, metamaterials, optical sensor, one dimensional photon crystal, and sub-wavelength microstructure. 29 papers have been published in international academic journals, and 17 patents applicanted. The total researching founds are 15.415 millions. This year, we obtained some important results as following:

(1)我们提出了一种石墨烯选择性定点转移方法。使用光刻胶曝光和 PMMA 转移方法相结合，并利用显微镜和微操作平台进行转移的微观操作控制，可以将需要的石墨烯部分从整体结构上选择性的转移出来，转移到目标基底的指定位置。采用本方法可以高效地将选定的石墨烯或石墨烯微结构转移到目标基底的指定位置，特别适合于机械剥离法石墨烯的选择和转移。由于石墨烯与其它结构或材料的结合可以极大的提高石墨烯的性能和应用范围，因此将选择的石墨烯精确的定点转移到目标基底或目标结构上对石墨烯材料的研究和应用有着重要的科学意义和实用价值。

We demonstrate a selective microcleaving graphene (MG) transfer technique for the transfer of graphene patterns and graphene devices onto chosen targets

using a bilayer-polymer structure and femtosecond laser microfabrication. In the bilayer-polymer structure, the first layer is used to separate the target graphene from the other flakes, and the second layer transfers the patterned graphene to the chosen targets. This selective transfer technique, which exactly transfers the patterned graphene onto a chosen target, leaving the other flakes on the original substrate, provides an efficient route for the fabrication of MG for microdevices and flexible electronics and the optimization of graphene's performance. This method will facilitate the preparation of van der Waals heterostructures and enable the optimization of the performance of graphene hybrid devices.

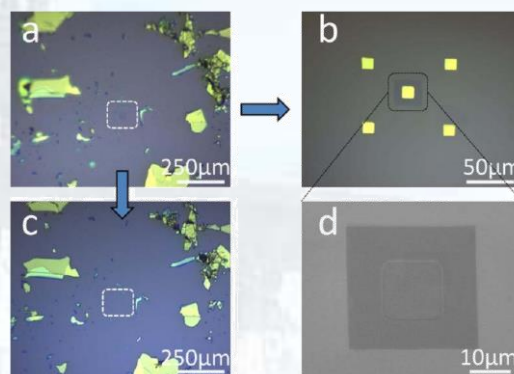


图 1 石墨烯选择性定点转移结果。(a) 利用飞秒激光图形化处理后的单层机械剥离石墨烯；(b) 将石墨烯选择性转移到 SiO₂ 微腔上；(c) 转移后残留的其他石墨碎片；(d) 转移后石墨烯覆盖微腔的 SEM 图。

Fig. 1 Results of the selective transfer and precise location.(a-c), Optical images of (a) a monolayer MG patterned by femtosecond laser on a SiO₂/Si wafer, (b) the patterned graphene located on a chosen microcavity obtained by selective transfer, and (c) the graphene/graphite flakes remaining on the original substrate. (d), The morphological images of the patterned graphene above the microcavity analyzed by SEM.

(2)利用石墨烯偏振吸收效应，我们实现

了基于石墨烯的多层膜光存储。我们在研究石墨烯光学性质时发现, 如果将石墨烯置于两层介质之间, 对于 s 和 p 入射偏振光将产生不同的反射和吸收行为。光学数据存储带来了信息存储容量革命性的进步。随着数字信息的显著增加, 存储介质的存储容量需要进一步的改善。石墨烯是最薄的二维材料, 利用石墨烯作为存储介质将具有最薄的厚度, 从而提升存储的面密度和记录层数。我们通过石墨烯对两种不同偏振光的反射差别来读取记录在石墨烯上的存储信息。改变入射光的角度, 利用不同聚合物折射率的差别, 读取不同层位置的石墨烯所记录的数据。

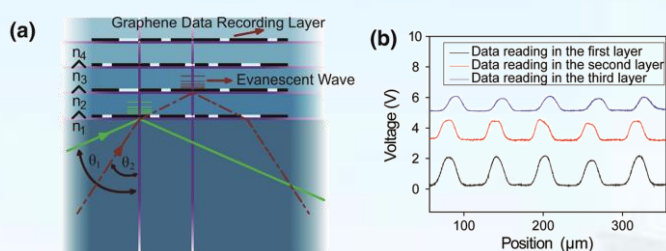


图 2. (a) 基于石墨烯的多层膜光存储结构数据读取示意图; (b) 三层石墨烯光存储结构的数据读取结果。

Fig. 2. (a) Data-reading schematic illustration of the graphene-based multi-layer-film ODS medium. (b) The reading results for each layer of the three-layer-film ODS medium.

Based on the polarization-sensitive absorption of graphene under condition s of total internal reflection, we demonstrate the fabrication and reading of transparent and flexible multi-layer-film optical data storage media based on graphene recording layers. We report a realization of the process of data writing-transferring-reading by repeatedly transferring recorded graphene and its strong polarization effect. The reading results show a high signal-to-noise ratio and stability and low crosstalk interference between the layers. In addition, the graphene-based multi-layer-film optical data storage medium has a high transparency and flexibility.

(3) 我们应用石墨烯费米能级的可控特性, 提出了应用反对称单层石墨烯纳米十字天线实现光学偏振动态调控的方案。实现了线偏振光的巨光学旋转和从线偏振光到圆偏振光和椭圆偏振光的转换, 通过改变石墨烯的费米能级, 可以动态调控透射光的工作波长和偏振态。我们的工作为可控偏振转换器的研究提供了依据。

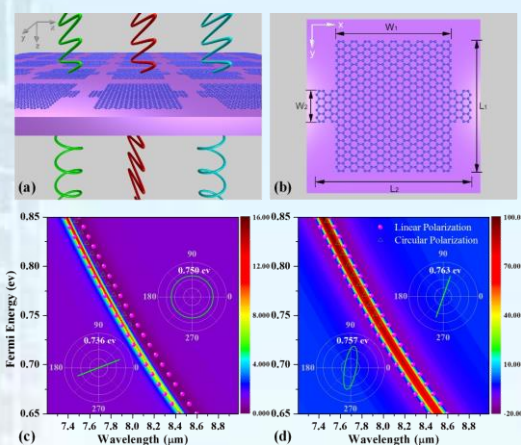


图 3. (a) 线偏光经过反对称石墨烯纳米十字天线的转换示意图; (b) 反对称石墨烯纳米十字天线结构示意图; 不同费米能级和入射光波长下的 (c) 振幅比和 (d) 位相差。插图不同费米能级下实现的线偏振光的巨光学旋转和从线偏振光到圆偏振光和椭圆偏振光的转换。

Fig. 3 (a) Schematic model of asymmetric graphene nanocrosses on a substrate. (b) Unit cell structure of our design: $L1=70$ nm, $W1=63$ nm, $L2=80$ nm, $W2=16$ nm, and the periodicity is 90 nm. (c) The calculated amplitude ratio and (d) phase difference as a function of the Fermi energy and wavelength. Inset images show the transmitted polarization state for different Fermi energies at the wavelength of 7.92 μm .

We present a mid-infrared highly tunable optical polarization converter composed of asymmetric graphene nanocrosses. It can convert linearly polarized light to circularly and elliptically polarized light, or exhibit a giant optical activity at different wavelengths. The transmitted wavelength and polarization states can also be dynamically tuned by varying the Fermi energy of graphene, without re-optimizing and re-fabricating the nanostructures. This offers a further step in

developing a controllable polarization converter.

(4)开展了偏振无关广角等离子激元诱导透明平面超材料的研究,证明局域非对称是产生等离子激元诱导透明的关键条件,但是可以通过整体对称实现等离子激元诱导透明,为等离子激元诱导透明的产生和调控提供了新的途径。研究了由氧化钒天线和狭缝天线阵列形成的杂化超材料,利用氧化钒在近红外波段具有良好的金属-半导体相变特性,通过温控实现了等离子激元诱导反射的动态调控。由于氧化钒不是简单的作为基底或者夹层,而是嵌入的狭缝天线中,这样将大大增强动态调控的灵敏性和调控强度。同时,提出一种四能级等离子激元系统解释并且分析这种等离子激元诱导透明的形成机制,四能级模型同数值模拟和实验结果符合的很好。

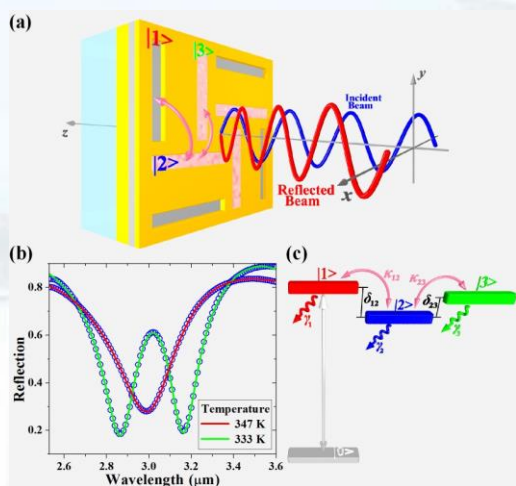


图 4. (a) 动态可调等离子激元诱导反射复合超材料结构示意图; (b) 不同温度下等离子激元诱导反射谱; (c) 四能级等离子激元系统。

Fig. 4. (a) Perspective view of a unit cell of the tunable PIT planar MM. The pink arrows indicate the near-field coupling between meta-atoms. (b) Simulated transmission spectra achieved by FEM (blue-circled curves) and four-level plasmonic model (color-solid lines) for different temperature. (c) Coupled four-level plasmonic system for the tunable PIT planar MM.

We design and analyze numerically a

dynamically tunable plasmonically induced transparency (PIT) planar hybrid metamaterial (MM) in near-infrared regime, which combines the near-field coupling effect into active MM. The embedded position of tunable material in active MM is optimized. Thermal-tunable VO₂ stripes are filled in the cut-out slots as components of plasmonic system, which dramatically improve the dynamic modulation depth of the PIT. We also use a four-level plasmonic system to quantitatively analyze the dynamically tunable PIT device. This work may offer a further step in the design of tunable PIT effect.

(5)开展了通过复合超材料操控局域近场光学偏振态的研究,提出了一种由反对称纳米孔和领结纳米天线构成的线性纳米偏振转换器,给出了一种自由控制局域近场光学偏振态新方法。提出的线性纳米偏振转换器不仅可以产生大的局域场增强和局域场的均匀空间分布,而且可以在任意线偏光、圆偏光或椭偏光激发下产生固定偏振态的线偏光。通过调整反对称纳米孔的结构参数,线性纳米偏振转换器的响应波长可以很容易的在宽频范围内调控。我们的研究成果为局域近场光学偏振态的操控提出了一种新的方案。

We present a linear nano-polarizer composed of asymmetric nanoaperture and bowtie nanoantenna, which provides a new way to freely control the polarization azimuth of the translated optical field in the near-field. It can not only generate large localized field enhancement and outstanding spatial confinement, but also maintain the polarization azimuth of linearly polarized optical field excited by arbitrary linearly, circularly or elliptically polarized lights. The response wavelength of the linear

nano-polarizer can be easily tuned in a wide range by adjusting the geometrical parameters of asymmetric nanoaperture. This offers a further step in developing integrated optical devices for polarization manipulation.

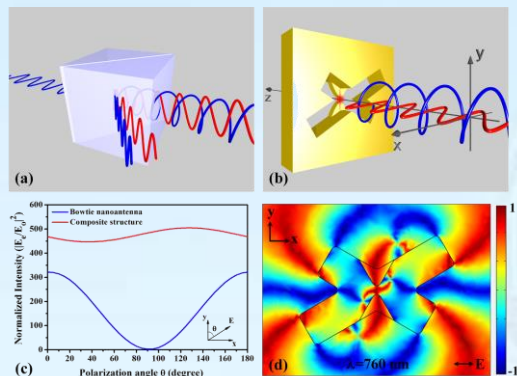


图 5. (a) 传统的格兰泰勒棱镜；(b) 设计的线性纳米偏振转换器；(c) 领结天线和复合线性纳米偏振转换器的强度谱；(d) 偏振度 C 因子的分布，入射光偏振沿着 x 方向， $C=1$ 或者 $C=-1$ 分别对应沿着 y 轴或 x 轴完美线偏振。

Fig. 5 (a) A Glan-Taylor polarizer reflects s -polarized light at an internal air-gap, transmitting only the p -polarized component. (b) The designed linear nano-polarizer, generating linearly polarized optical field with a fixing polarization azimuth excited by arbitrary linearly, circularly polarized lights. (c) Normalized intensity of bowtie nanoantenna and linear nano-polarizer under different incident excitation light polarizations at the resonant wavelengths. (d) Distribution of the degree of polarization C with the polarization azimuth of incident light along x direction, for which $C=1$ or $C=-1$ present a perfect linear polarization along the y or x axis, respectively.

(6)在胶体球刻印法中，用二氯甲烷溶液刻蚀去除聚苯乙烯胶体微球，制备出了具有不同开口大小及方向的破缺金属纳米球壳阵列结构。在实验过程中我们发现利用二氯甲烷溶液去除胶体球时，在不同反应时间下，可以获得不同开口大小、方向的金属纳米球壳结构。该结构的透射、吸收光谱表明，金属纳米球壳结构的对入射光的偏振和入射角度都具有明显依赖关系。

We fabricated inclined Au nanocup arrays by using the nanosphere lithography method

combined with dichloromethane etching and investigated their optical properties. The size and the orientation of the nanocup can be controlled by the reaction time. The transmittance and absorption spectra of these Au nanocup arrays under different polarizations and incident angles were detected. And their properties are strongly related to the polarization and the incident direction of the light.

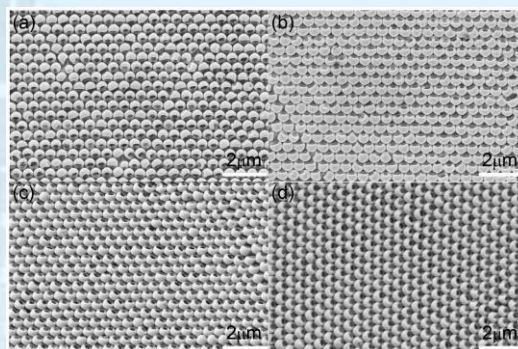


图 6. 不同反应时间下生成开口大小不同的金属球壳结构。
Fig. 6 SEM images of samples for different reaction time. (a) 20 s, (b) 40 s, (c) 60 s, (d) 90 s.

(7)在金属-电介质-金属表面等离子激元波导研究中，借助变换光学理论，通过调整相位和功率密度分布，我们在金属-电介质-金属波导中设计了可以将反对称束缚模转换为对称束缚模的模式转换器。我们提出了两种实用的模式转换器结构，用数值方法模拟验证了转换器的功能。在不考虑传输损耗的情况下，实现了高达 95% 的模式转换效率。在考虑金属损耗的情况下，实现了超过 80% 的模式转换效率。

In order to facilitate multifunctional manipulations of light in plasmonic metal-dielectric-metal waveguides, we design mode converters in the waveguides that can convert the asymmetric mode to the symmetric mode. Efficient conversion between the two modes can be achieved by reshaping both phase and power density distributions of the guided mode, which are

designed with the assistance of transformation optics. We propose two practical configurations of mode converter in plasmonic waveguides. The functionalities of the converters are demonstrated by numerical simulations. Without consideration of transmission loss, conversion efficiency of as high as 95% can be realized. When ohm loss is considered, the conversion efficiency is more than 80%.

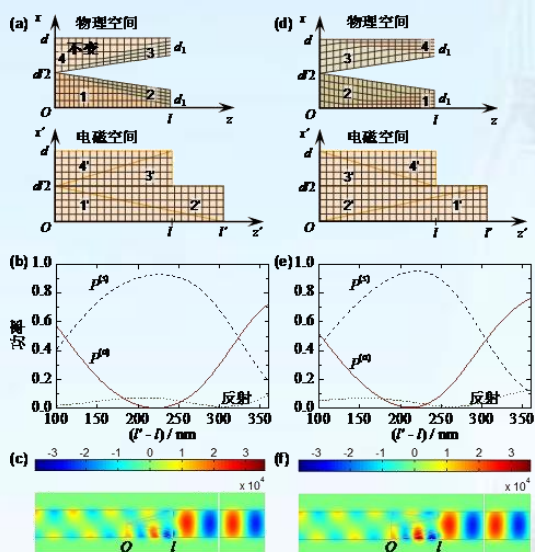


图 7. 通过同时调控相位和功率密度分布实现模式转换器的设计和功能。(a)和(d)分别为用于变换光学的两种设计方案。(b)和(e)给出了两种设计方案的出射和反射功率随着(l'-l)的变化曲线。(c)和(f)是两种设计方案中最大转换效率处 E_z 分布图。

Fig. 7 Mode conversion by reshaping both phase and power density. (a) and (d) show two divisions of the physical and virtual spaces. (b) and (e) show the power flows of transmission as well as the reflected power, as functions of $(l' - l)$. (c) and (f) show the snapshots of E_z fields at the maximum conversion efficiencies of (a) and (d) respectively.

(8)在一维双周期光子晶体中实现子能带激射。相对于光子晶体带边激射，子能带激射的激发效率显著地提高了 8 倍，同时阈值降低到原来的 1/6。与含 Rh6G 的明胶薄膜比较，双周期光子晶体可实现荧光增强高达 660 倍。这种高效率地阈值子能带激射是由于双周期光子晶体子能带的平坦色散和

长距离电场局域增强导致的。另外，我们还在一维双周期光子晶体中观察到彩色多环锥形激射，从而推测出光子晶体中存在能带耦合。我们提出了能带耦合模型来数值拟合锥形激射的特性，得到的激射锥角和激射波长与实验十分吻合。

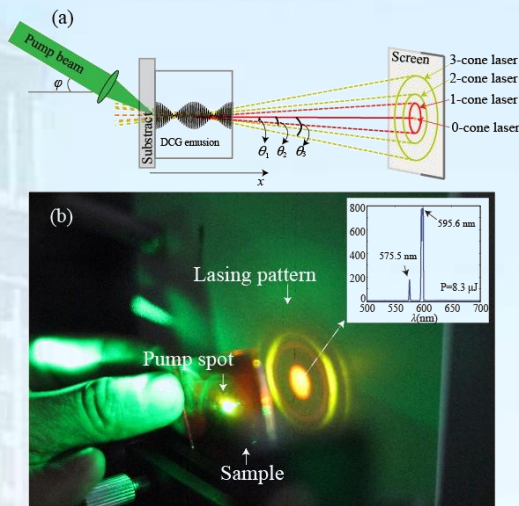


图 8. (a)锥形激射激发实验简图。中间方框是 DCG 的折射率分布。样品的锥形激射被在其后的光屏所接受，角度分别是 $\theta_1, \theta_2, \theta_3$ ，我们分别称之为 1-, 2-, 3- 锥形激光 (cone laser)。(b) 佳能 EOS 600D 拍摄的光屏上的锥形激光光斑照片，所使用曝光参数是：曝光时间 0.25s，光阑是 $f/1.8$ 。右上角的插图是 0- cone laser 在 $8.3 \mu\text{J}$ 时的荧光光谱，可以看到子能带激射和短波带边激射峰。

Fig. 8 (a) Schematic experimental setup of lasing excitation. The profile of the refractive index in DCG emulsion is shown. The sample emits cone-shaped lasing with angles of θ_1, θ_2 , and θ_3 , which are marked as 1-, 2-, and 3-cone laser, respectively. (b) A photo of the backward cone laser pattern displayed on the screen. The photo was taken using a Cannon EOS 600D with exposure time 0.25s and aperture value $f/1.8$. The inset is the fluorescence spectrum for 0-cone laser pumped at $8.3 \mu\text{J}$

We demonstrate miniband lasing in a 1D dual-periodic photonic crystal (PC). The lasing efficiency is dramatically enhanced by about eight times and meanwhile the threshold is decreased to about 1/6 of that of the band-edge lasing in a single-periodic PC. Moreover, fluorescence emission enhanced by a factor of up to 660 was observed as compared with that in dye-doped film. This

high optical conversion efficiency can be attributed to the extremely flat dispersion and large mode volume of the miniband induced by dual-periodicity. We also observed multiple and colorful cone-shaped lasing from dual-periodic photonic crystal, indicating that coupling occurs between the photonic bands in a photonic crystal laser system. We propose a band-coupling model to estimate lasing wavelengths and emission-cone angles, which match well those from experimental observations from cone-shaped lasing.

光子学材料及先进制备技术/ Photonics Materials and Advanced Fabrication Techniques

负责人: 孔勇发

本方向涉及多功能光学晶体、低维功能材料、软物质、硅基发光、微晶玻璃陶瓷、光子学微结构等方面。本年度发表论文19篇, 申请发明专利1项, 获得授权专利4项, 在研课题经费1883万元。获得天津市科学技术进步奖一等奖一项。取得的代表性成果如下:

In this field, we mainly focused on the multi-functional optical crystals, low-dimensional functional materials, soft matter, silicon based light emitting materials, nano-crystalline glass ceramics, and photonic microstructure. 19 papers were published in international academic journals, 1 invention patents applied, and 4 patent issued. The total researching funds are 18.83 millions. We obtained Tianjin Science and Technology Progress Award. This year, we obtained some important results, they are mainly shown as following:

我们设计并生长了镁钼双掺及钼钼双掺铌酸锂晶体, 并系统研究了这两个系列双掺晶体的光折变性能。实验结果如图1所示, 这两种双掺铌酸锂晶体都可以中成功实现从紫外到可见波段的全息存储, 但是当 ZrO_2 的掺杂浓度都超过阈值浓度时, 并没有起到提高掺钼铌酸锂晶体光折变响应速度的作用, 反而使得晶体在紫外和可见波段的响应时间比单掺钼铌酸锂晶体的更长, 饱和衍射效率更低。然而, 当 MgO 的掺杂浓度超过它在掺钼铌酸锂晶体中的阈值浓度时, 能够使晶体在紫外至可见波段的光折变响应速度得到极大的提高, 在351、488、532和671nm处的响应时间分别是0.22、0.33、0.37和1.2秒。这意味着 Mg^{2+} 离子更适合被选择共掺入掺钼铌酸锂晶体来提高晶体的光折变响应速度。镁钼双掺铌酸锂晶体是一种实现快速响应的全息数据存储器候选材料。

A series of LN:Mo,Zr and LN:Mo,Mg crystals with different Zr and Mg doping were grown and characterized. As shown in

Fig. 1, holographic storage from UV to the visible is realized in all of the doubly doped crystals. It is interesting that ZrO_2 cannot improve the response speed of LN:Mo even when its concentration is above the threshold. However, when the concentration of MgO exceeds the threshold, a very short photorefractive response time of 0.22 s, 0.33 s, 0.37 s and 1.2 s for 351, 488, 532 and 671 nm was obtained, respectively. Our experimental results indicate that Mg^{2+} ions are a preferable choice to improve the photorefractive response of LN:Mo crystal. LN:Mo,Mg can be an excellent candidate for all-color holographic data storage with fast response.

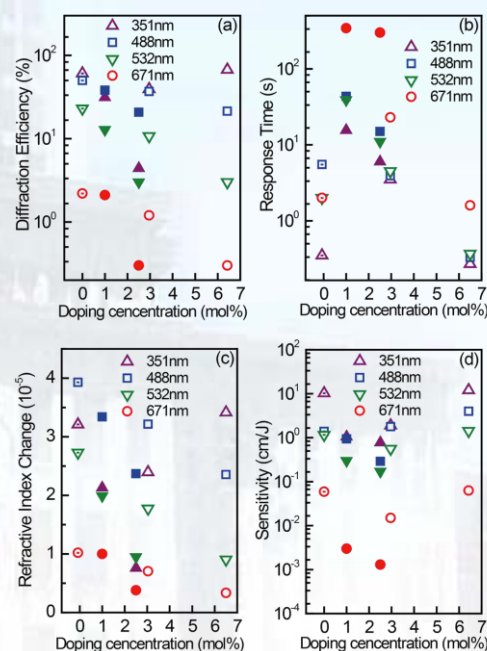


图1. 钼钼双掺铌酸锂和镁钼双掺铌酸锂晶体在紫外到可见光区的光折变性能随掺钼(实心符号)和掺镁(空心符号)量的变化:(a)衍射效率,(b)响应时间,(c)折射率变化,(d)灵敏度。对应351, 488, 532和671 nm激光的单束光强分别为238, 400, 400和1500 mW/cm^2 。

Fig. 1 The photorefractive (a) diffraction efficiency, (b) response time, (c) refractive index change and (d) sensitivity of LN:Mo crystals codoped with different concentration of Zr (solid symbols) and Mg (open symbols) from UV to the visible. The light intensity per beam is 238, 400, 400, and 1500 mW/cm^2 for 351, 488, 532, and 671 nm laser, respectively.

我们在原磷酸盐光电功能材料研究方向

外, 初步开展了基于二阶姜-泰勒效应的功能化合物的制备、结构和性质研究。代表性成果为CsLa(PO₃)₄ (单斜P₂₁空间群结构) 单晶的生长和构效关系的调查。生成态晶体主要由{001}、{011}、{-101}和{-110}等晶面构成。我们从化学键强度和结构基元的空间堆积分析了晶体沿(001)和(100)面易发生解理的原因; 通过基于键价理论的偶极矩的计算分析了氧多面体的畸变。CsLa(PO₃)₄具有高的热稳定性, 926°C才会发生热分解。该晶体在室温附近的热释电系数为9.72μC/m²·K; CsLa(PO₃)₄的粉末SHG性能约为KDP的1/2, 可能由于相位匹配条件不满足的原因未能在晶体上观察到SHG信号。理论计算表明CsLa(PO₃)₄为间接带隙材料, 价带主要由O-2p和Cs-5p构成, 导带主要P-3p和La-5d轨道所占构成。光学性质的计算结果表明该材料具有有小的双折射和大的色散, 从而导致其难以实现相位匹配。该材料在0.17~4.0μm范围内具有良好的透光性, 其紫外吸收边短至167nm。

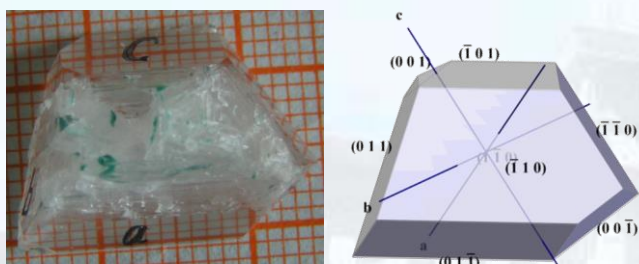


图2.自发成核生长的CsLa(PO₃)₄晶体(左)与其晶面指认后的外形模拟(右)。

Fig. 2. (Left) CsLa(PO₃)₄ crystal grown by spontaneous nucleation. (Right) Stimulated facets marked by Miller indices (*hkl*).

Besides the former research interest on functional materials of phosphates, we gradually engaged in synthesis, structure and properties of functional compounds based on the second order John-Teller effect. This year, we made a typical progress on the growth of CsLa(PO₃)₄ single crystal with P₂₁ space group and its structure-properties relationship. The morphology of the as-grown crystal was made up of the crystalline forms {001}, {011},

{-101}, {110}, etc. The cleavage habit along (001) and (100) faces was analyzed from the point of view of chemical bond and stereo structure. The local dipole moments for the PO₄, CsO₁₀ and LaO₈ polyhedra were calculated by using a bond-valence approach for understanding their distortions. CsLa(PO₃)₄ presents a good thermal stability till 926°C. Its pyroelectric coefficient near room temperature is about 9.7μC/m²·K. The SHG intensity of CsLa(PO₃)₄ powder is only one half of that of KDP. However, no SHG signal was observed on the as-grown crystal, which may be attributed to phase mismatch. The results of theoretical calculation showed that CsLa(PO₃)₄ is a kind of indirect band gap material. Its conducting band was mainly occupied by the 2p orbits of O atoms and the 5p orbits of Cs atoms, and the valence band by the 3p orbit of P atoms and the 5d orbits of La atoms. The simulation of optical property reflected that the crystal has a low birefringence and a big dispersion. CsLa(PO₃)₄ crystal shows a good transmittance in the range of 0.17~4.0μm and a short UV cutoff edge of 167nm.

我们完成了 MgO/SrO-ZnO-B₂O₃ 和 BaO/ZnO-Bi₂O₃-B₂O₃ 四个体系固相线下相关关系的研究。分别研究了 Ba₂ZnB₂O₆:Eu³⁺和 ZnBi₂B₂O₇:Eu³⁺的光致发光性质, 它们均可同时被近紫外光和蓝光激发, 发射色纯度较高的红色荧光, 并对掺杂后微结构的变化进行了深入研究。合成了两个新结构化合物, 并制备了纯相, 由其元素组成分析, 这两个化合物适宜作为新荧光材料的基质, 其结构正在解析过程中。在研究 NaSrBO₃:Eu³⁺的发光现象过程中, 确认了基质材料的相变过程, 并用粉末从头算法解析了该基质材料的新结构相, 认为该荧光材料的光致发光是在新相结构基础上产生的。

The subsolidus phase relations of four systems MgO/SrO-ZnO-B₂O₃ and BaO/ZnO-Bi₂O₃-B₂O₃ were studied by solid

state reactions. The photoluminescence of $\text{Ba}_2\text{ZnB}_2\text{O}_6:\text{Eu}^{3+}$ and $\text{ZnBi}_2\text{B}_2\text{O}_7:\text{Eu}^{3+}$ were studied, which exhibit red color with high color purity and brightness under the excitation of both near UV light and blue light, and the structure changes of doping samples were studied. Two new compounds were synthesized, and the pure phases were prepared for structure determination. They will be good hosts for new phosphors, and the structure determination is under going. A phase transition of the host was confirmed during the investigation of the photoluminescence of $\text{NaSrBO}_3:\text{Eu}^{3+}$, and the new structure was solved by *ab initio* method. It was believed that the luminescence properties were exhibited on the new phase structure.

通过 Eu^{3+} 离子作为荧光探针研究了镧系元素掺杂的 $\beta\text{-PbF}_2$ 纳米颗粒。三价稀土离子以取代 Pb^{2+} 格位的方式掺入纳米晶中, 并且发现稀土掺杂浓度可以诱导稀土离子位置对称性从 O_h 到 D_{4h} 的畸变。通过荧光和 X 射线衍射分析, 低浓度稀土离子掺杂的纳米颗粒具有 Pb_3EuF_9 立方相结构, 其点群和空间群分别是 O_h ($m-3m$) 和 $Pm-3m$ (No. 221)。然而随着掺杂浓度的增加, Pb_3EuF_9 立方相结构逐渐转变为具有点群和空间群分别为 D_{4h} ($4/mmm$) 和 $P4/mmm$ (No. 123) 的 PbEuF_5 四方相结构。特别是在中等浓度掺杂的时候我们第一次提出并证实了两种混合结构的共存。另外, 根据第一性原理中结合能的计算, 四方相结构的结合能比立方相结构的结合能低 2.327eV, 这意味着在高浓度掺杂的时候四方相结构比立方相结构更加的稳定, 更易形成。这个工作让我们更加全面深入的理解了镧系元素在氟化物纳米晶中的位置对称性以及它们在氟化物纳米晶中所处的晶格场环境。这对进一步稀土离子光学特性的研究, 比如结构对稀土离子发光的调控等, 有着重要的指导意义。

在以上工作的基础上制备了一系列不同稀土离子掺杂的玻璃陶瓷, 通过热处理获

得了一系列不同稀土离子掺杂的纳米颗粒, 通过 XRD 对其结果进行了分析, 结果表明对于不同稀土离子的掺杂, 以上的结论同样适用。针对不同的稀土离子, 其半径与结构存在一定的约束关系。

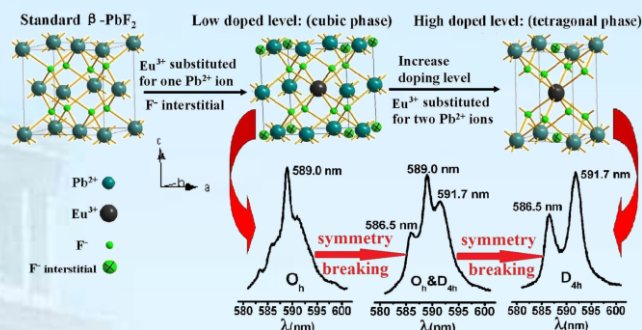


图3. 不同Eu离子掺杂导致结构从 Pb_3EuF_9 到 PbEuF_5 的对称破缺示意图。

Fig.3. Photoluminescence spectroscopy employing Eu^{3+} as the structural probe unambiguously revealed a doping concentration induced phase transition from lowly doped cubic Pb_3EuF_9 to highly doped tetragonal PbEuF_5 .

By using Eu^{3+} as a fluorescence probe in Lanthanide-doped $\beta\text{-PbF}_2$ nano-particles, Ln^{3+} ions are substituted for Pb^{2+} sites and the doping concentration induces a site symmetry distortion from O_h to D_{4h} . By photoluminescence and XRD study, we conclude that the structure of lowly doped nano-particles is cubic Pb_3EuF_9 (O_h ($m-3m$), $Pm-3m$ (No. 221)). With the increase of doping concentration, the cubic Pb_3EuF_9 transforms to tetragonal PbEuF_5 (D_{4h} ($4/mmm$), $P4/mmm$ (No. 123)). Particularly, the coexistence of both structures in moderately doped nano-particles is proposed and confirmed for the first time. The binding energy of the C and T structures differs with about 2.327 eV, which means that the T structure is more stable and easier to form in highly doped materials. Our work represents a significant advance towards a more comprehensive understanding of the site symmetry of Ln^{3+} ions in fluoride nano-particles, which would benefit the further research on the optical properties, such as fluorescence regulation and control of Ln^{3+}

ions, and have great importance in the applications of this material in optical fields.

A series of rare earth (RE) doped oxyfluoride glasses with the composition of $(45-x) \text{SiO}_2\text{-}5\text{Al}_2\text{O}_3\text{-}40\text{PbF}_2\text{-}10\text{CdF}_2\text{-}x\text{RE}_2\text{O}_3$ ($x = 1, 5, 10, 15$) (mol%) were prepared by a traditional melt-quenching method. Glass ceramics (GCs) were obtained after thermal treatment and characterized by X-ray diffraction (XRD) to investigate the nanocrystal structure and distortion. Based on the RE-doping mechanism of $\text{Pb}^{2+}\text{-RE}^{3+}$ substitution with interstitial F⁻ charge compensation, different phases can form via adjusting the dopant concentration. The cubic Pb_3REF_9 phase with Pm3m space group plays a dominant part in low dopant concentration. The unit cell parameters decrease from 5.92 Å to 5.80 Å from Pr to Yb. Tetragonal PbREF_5 phases with P4/mmm(No. 123) space group appear with increasing dopant concentration, and RE^{3+} has a typical $D_{4h}(4/mmm)$ point symmetry. The “peak splitting” in the XRD spectra was found in GC doped with RE^{3+} , and the splitting distance gets smaller and smaller as the RE^{3+} ionic radius increases from Yb^{3+} to Dy^{3+} . This phenomenon was well explained by the structural distortion due to the difference in ionic radius between the host ion and the guest ion. Our work provides a comprehensive understanding towards nanocrystal structure at the atomic level and the RE^{3+} environment in oxyfluoride glass ceramics, which would benefit further optical investigations and practical applications.

利用原子层沉积技术优化制备了 SiO_2 、 Al_2O_3 、 TiO_2 、 Tb_2O_3 和 Er_2O_3 薄膜等基础硅基薄膜材料, 对各类薄膜的光学和电学性能进行了系统的研究; 然后从原子层尺度精确配比制备了光电性能可调的 $\text{ZnO}/\text{Al}_2\text{O}_3$ 复合透明导电薄膜、 $\text{TiO}_2/\text{Al}_2\text{O}_3$ 介质缓冲和电注入复合薄膜, 稀土氧化物掺杂的 SiO_2 等纳米层状复合发光薄膜。最终研制出高效率

的硅基 MOS 结构电致发光器件。

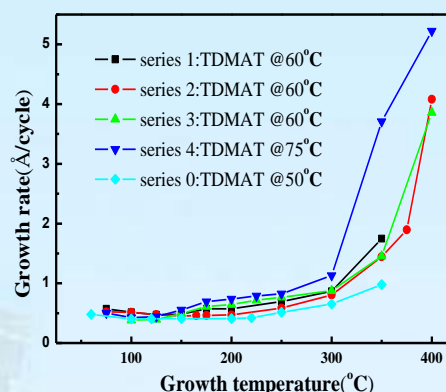


图4. 不同TDMAT源温度下 TiO_2 薄膜的ALD单层生长速率随衬底温度的变化。

Fig.4. The growth rate of the TiO_2 films grown by ALD under different TDMAT source temperatures.

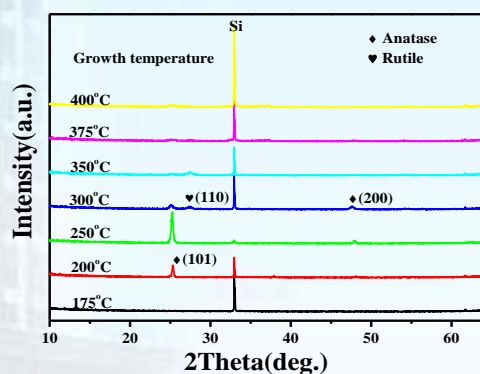


图5. 不同温度下ALD生长的 TiO_2 薄膜的XRD谱。

Fig.5. XRD patterns of the TiO_2 films grown by ALD at different growth temperatures.

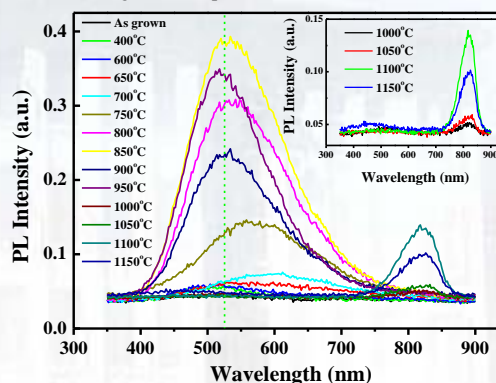


图6. ALD生长的锐钛矿相 TiO_2 薄膜经过不同温度退火后的发光光谱。

Fig.6. PL spectra of the TiO_2 films grown by ALD at different annealing temperatures.

SiO_2 、 Al_2O_3 、 TiO_2 、 Tb_2O_3 and Er_2O_3 thin films were prepared by atomic layer deposition technology. The optical and electrical properties of the films were studied,

transparent conductive ZnO/Al₂O₃, dielectric buffer and electron injection TiO₂/Al₂O₃, and rare earth doped SiO₂ luminescent multiple layers were prepared by fine tuning of the atomic layers using ALD technology. Efficient rare earth doped SiO₂ MOS electroluminescence devices were prepared by full ALD technology.

氧化钛薄膜具有非常高的介电常数 (80) 非常稳定的化学性质, 具有良好的光催化性能、亿阻效应, 可用于光催化、阻变存储器件等。TiO₂ MIS结构具有良好的大电流注入发光性能, 可以用于硅基电致发光器件。我们利用TDMAT与臭氧反应原子层沉积方法在硅衬底上分别制备了非晶态, 锐钛矿和金红石相的薄膜, 系统研究了TiO₂薄膜原子层沉积的衬底温度, 热处理温度对于薄膜的晶体结构, 发光性能的影响。研究表明利用ALD方法可以不同的衬底温度区间不同结构的TiO₂薄膜, 生长速率为0.4-0.6Å/周期左右。在(100-200℃)为非晶态, 在(200-300℃)为锐钛矿相, 在350℃以上生长的TiO₂薄膜为金红石相。在266nm紫外光激发下, 处于锐钛矿相的TiO₂薄膜能够发出红色或者绿色光。金红石相的TiO₂薄膜能够发出波长在830nm的红外发光。1000℃以上高温退火可以促使锐钛矿向金红石相转变。结构和性能可控的优质TiO₂薄膜的研究为进一步研制低电压大电流注入的硅基电致发光器件奠定了基础。

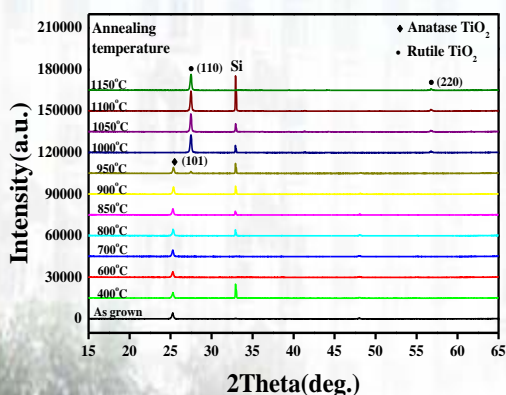


图7. 250℃ ALD生长的锐钛矿相TiO₂薄膜经过不同温度退火后的XRD谱。1000℃ 转化为金红石相。

Fig.7. XRD patterns of the TiO₂ films grown by ALD at different annealing temperatures.

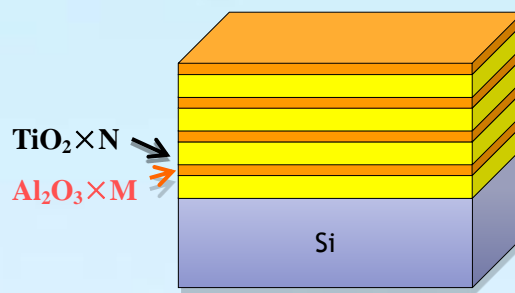


图8. TiO₂/Al₂O₃复合介质层的原子层生长示意图。

Fig.8. The schematic of the TiO₂/Al₂O₃ multiple films grown by ALD.

我们用ALD技术生长两种介电性能互补的TiO₂/Al₂O₃纳米层状介质保护层, 其中TiO₂薄膜具有大的介电常数和较大的注入电流, 与绝缘性能好击穿场强高的Al₂O₃性能互补, 通过利用ALD生长技术精确调控TiO₂/Al₂O₃原子层比例, 在Ti_{0.75}Al_{0.25}O_x比例下调配出既能注入击穿电流密度0.5A/cm², 耐击穿场强大于4.3MV/cm, 介电常数大于15的TiO₂/Al₂O₃复合介质保护层, 解决了硅基MOS结构电注入稳定性问题。

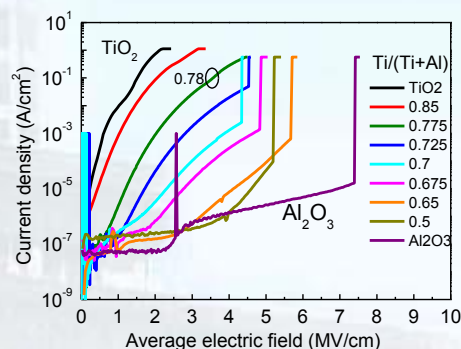


图9. 不同TiO₂原子层比例的TiO₂/Al₂O₃复合介质层的电流电压特性。

Fig.9. I-V characteristics of the TiO₂/Al₂O₃ multiple films with different atomic layer ratios.

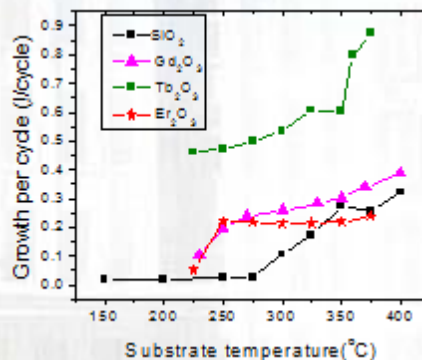


图10. SiO₂, Gd₂O₃, Tb₂O₃和Er₂O₃薄膜的ALD生长速率随衬底温度的变化。

Fig.10. Growth rates of SiO₂, Gd₂O₃, Tb₂O₃ and Er₂O₃ films as a function of substrate temperatures.

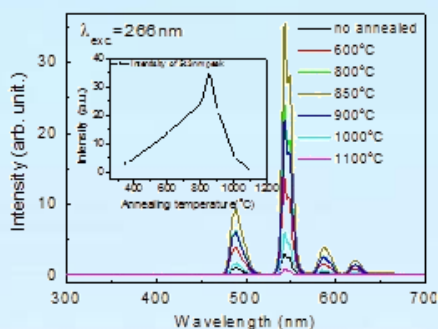


图11. 不同退火温度下稀土Tb离子掺杂的SiO₂薄膜在的光致发光光谱。

Fig.11. PL spectra of the SiO₂:Tb films annealed at different temperatures.

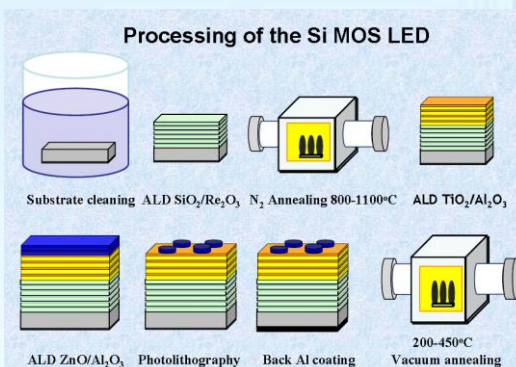


图12. 硅基MOS电致发光器件的工艺流程图。

Fig.12. The processing line of the Si MOS LEDs.

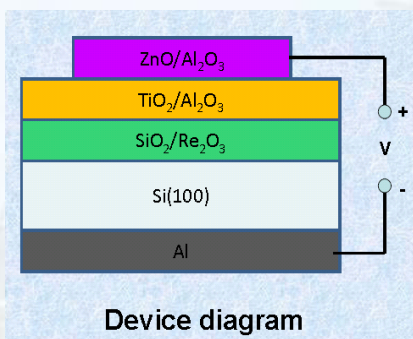


图13. 器件的结构示意图。

Fig.13. Schematic of the structure of the Si MOS LED.

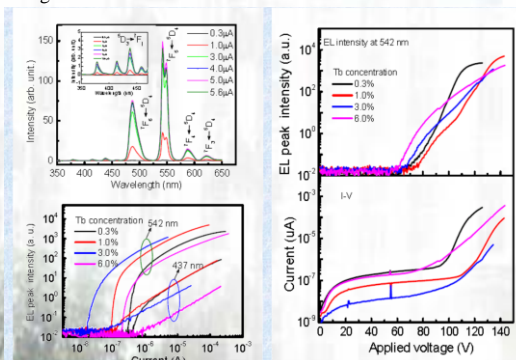


图14. 硅MOS电致发光器件的电致发光性能。

Fig.14. EL properties of the Tb doped SiO₂ green MOSLEDs.

我们采用原子层沉积系统在单晶硅片

上生长了Tb₂O₃和Er₂O₃稀土薄膜，系统研究了ALD生长温度对生长速率的影响。进一步利用Tb₂O₃单原子层掺杂方法制备了稀土掺杂的SiO₂发光薄膜，结合高温退火获得了高效率的SiO₂: Tb和硅酸铽发光薄膜。

首次全部利用原子层沉积技术在硅衬底上构建了由透明导电薄膜、high-k复合介质薄膜、以及稀土掺杂的氧化硅薄膜构成的硅基MOS结构复合薄膜电致发光器件，获得了高效率的紫外、蓝色和绿色硅基电致发光，并系统研究了器件的电致发光性能。ALD方法制备的SiO₂: Tb绿色MOS电致发光器件的EL和电学性能，器件发光阈值电流为纳安量级。器件的量子效率大于10%，达到已报道的热氧化和离子注入方法获得的同类硅基MOS电致发光器件的水平。

黑硅的锥状结构具有良好的减反效果，利用这些特点，可以将其应用于制作表面拉曼增强(SERS)衬底。我们利用聚二甲基硅氧烷(PDMS)压印黑硅表面的锥状微纳结构，制备出了一种大面积低成本高增强因子的SERS衬底。该SERS衬底的增强因子为10⁶~10⁷，衬底的SERS均匀性良好，可重复性高。由于采用的是成熟的纳米压印材料PDMS，其制作成本低，具备实际应用潜力。

飞秒微构造硅材料在光电子领域有着很好的应用前景，针对光生载流子的输运及弛豫过程物理机制，我们通过探测空气中微构造硅材料的时间分辨光致发光谱，建立了载流子迁移、复合模型，分析了其光致发光机理并研究了温度及缺陷对载流子复合过程的影响。我们对比了退火样品和未退火样品的差异，在300K温度下，对于未退火样品，有A_{snr0}~6.9×10⁻¹⁰，而对于退火样品，A_{snr0}~2.4×10⁻¹⁰。可见，退火后，非辐射复合被明显减弱，这是由于退火修复了大量缺陷（非辐射复合中心）。缺陷浓度的降低大大减小了载流子迁移过程中被其捕获的几率，增大了载流子寿命。

我们完成了电解法制备纳米Al₂O₃的研究，小批量制备了粒径在30~70nm Al₂O₃。完成了纳米AZO粉团化造粒技术的研究，批量制备了粒径在5~20um的球形团化颗粒。

完成了注浆成型技术的综合工艺研究, 获得了相对密度为72.1%的高密度素坯。完成了温场分布、烧结曲线等烧结工艺研究, 获得了200×400×10mm相对密度为98.5%的高密度靶材, 电导率 $\leq 2.0 \times 10^{-3} \Omega \cdot \text{cm}$, 性能指标达到了863项目要求。

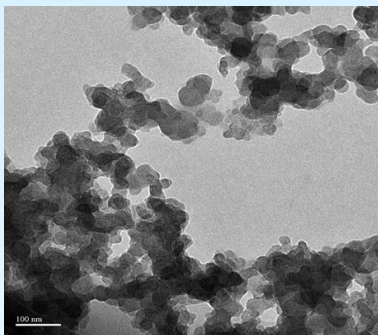


图15. 纳米 Al_2O_3 的TEM照片。

Fig.15. The TEM image of nano- Al_2O_3

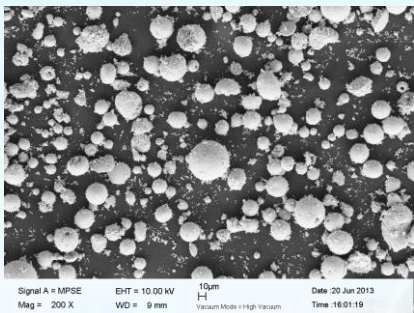


图16. 造粒后SEM形貌。

Fig. 16. The SEM morphology after granulation



图17. 烧结后靶材材料照片。

Fig.17. The photo of target material after sintering

我们完成了电解法制备纳米 Al_2O_3 的研究, 小批量制备了粒径在30~70nm Al_2O_3 。完成了纳米AZO粉团化造粒技术的研究, 批量制备了粒径在5~20um的球形团化颗粒。完成了注浆成型技术的综合工艺研究, 获得了相对密度为72.1%的高密度素坯。完成了温场分布、烧结曲线等烧结工艺研究, 获得了200×400×10mm相对密度为98.5%的高密度靶材, 电导率 $\leq 2.0 \times 10^{-3} \Omega \cdot \text{cm}$, 性能指标达到了863项目要求。

我们对无盐溶液中强带电聚电解质单

链的热力学性质——特别是链塌缩转变和标度行为进行了系统研究。使用显含溶剂分子和抗衡离子的模型, 澄清了在有限链长以及热力学极限下, 其单链的链塌缩转变为不连续相变。获得了热力学极限下的链塌缩转变温度以及体系的链尺寸与聚合度之间的关系。发现在某一区间内链尺寸与聚合度的标度指数可以大于1。

The thermodynamic behavior, especially the coil-globule transition and scaling behavior, of a strongly-charged polyelectrolyte chain in a solution system with explicit neutralizing counterions and solvent molecules are studied. The coil-globule transition is identified as a first-order transition at both at finite and infinite chain lengths. Phase transition temperatures at various ion concentrations are obtained. It is found that the exponent ν of the radius of gyration, $\langle R_g^2 \rangle \sim N^{2\nu}$, can be slightly larger than 1 under some conditions.

在我们的综述中, 我们讨论了嵌段共聚物受限条件和所形成的纳米结构之间的关系, 聚焦于二维和三维受限的两嵌段共聚物体系的结构形成原理。特别是讨论了匹配条件、表面与嵌段共聚物间的相互作用和受限几何对自组装结构的影响。

In our review paper, we discuss the relationship between confining conditions of block copolymers and the resulting structures, focusing on principles governing structural formation of diblock copolymers under two-dimensional and three-dimensional confinement. In particular, the effects of commensurability condition, surface-polymer interactions, and confining geometries on the self-assembled morphologies are discussed.

我们采用溶胶凝胶法制备了一系列具有可见光响应的N和Ni-Cl共修饰 TiO_2 催化剂 ($\text{TiO}_2\text{-N-x}\%\text{Ni}$)。光催化降解对氯苯酚实验结果表明 $\text{TiO}_2\text{-N-x}\%\text{Ni}$ 比纯 TiO_2 和N掺杂 TiO_2 呈现了更好的可见光催化活性。通过XRD、XPS、漫反射吸收谱和荧光谱对催化

剂的结构和性质进行了表征。结果表明，催化剂表面形成了独特的 NO_x 和 O-Ni-Cl 物种。 NO_x 和 O-Ni-Cl 物种掺杂能级分别位于 TiO_2 的价带上方和导带下方，导致了可见光吸收的增强，促进了光生载流子的分离。我们的结果为通过多种元素掺杂制备可见光响应的 TiO_2 催化剂提供了良好的示范。

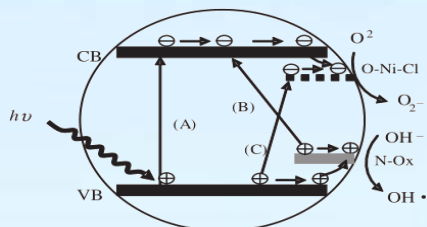


图18. $\text{TiO}_2\text{-N-x}\%\text{Ni}$ 的能带结构及光催化机理图。

Fig.18. Schematic diagram for the band structure of $\text{TiO}_2\text{-N-x}\%\text{Ni}$ and the photocatalytic mechanism.

A series of nitrogen and nickel-chlorine co-modified TiO_2 photocatalysts ($\text{TiO}_2\text{-N-x}\%\text{Ni}$) with visible-light response have been synthesized by a sol-gel method. The results of photocatalytic degradation of 4-chlorophenol (4-CP) suggest that $\text{TiO}_2\text{-N-x}\%\text{Ni}$ photocatalyst shows a higher activity than both pure TiO_2 and nitrogen doped TiO_2 ($\text{TiO}_2\text{-N}$) under visible-light irradiation. The structure and properties of the photocatalysts have been investigated by XRD, XPS, UV-vis diffuse reflectance spectra (DRS), and photoluminescence (PL) spectra. It was found that unique chemical species, such as N-Ox and O-Ni-Cl , existed on the surface of $\text{TiO}_2\text{-N-x}\%\text{Ni}$. The energy levels of N-Ox and O-Ni-Cl surface states locate above the valence band and below the conduction band of TiO_2 , respectively. This could lead to strong visible-light absorption and an enhanced charge carrier separation compared with both pure and $\text{TiO}_2\text{-N}$. Our results offer a paradigm for preparation of photocatalyst with a high visible-light activity by simultaneously doping TiO_2 with two or more different elements.

采用溶胶-凝胶法制备出偏硼酸锶

(SrB_2O_4)光催化剂。紫外光催化还原 CO_2 合成 CH_4 （在液相水中）的实验证明： SrB_2O_4 催化剂的光催化活性略高于 TiO_2 (P25)。利用X射线电子衍射谱(XRD)、傅里叶变换红外(FTIR)光谱、X射线光电子能谱(XPS)、透射电子显微镜(TEM)、荧光(PL)光谱和紫外-可见(UV-Vis)漫反射吸收光谱等技术，研究了 SrB_2O_4 催化剂的晶体结构、形貌和能带结构。结果表明： SrB_2O_4 的价带为2.07V (vs normal hydrogen electrode (NHE))，低于($\text{H}_2\text{O}/\text{H}^+$)的氧化还原电位 E_{redox} (0.82V (vs NHE))；而导带为-1.47V (vs NHE)，高于(CO_2/CH_4)的氧化还原电位 E_{redox} (-0.24V (vs NHE))。因此， SrB_2O_4 催化剂可以有效地光催化还原 CO_2 生成 CH_4 。与 TiO_2 (P25)相比， SrB_2O_4 催化剂具有相对较高导带，光生电子的还原能力强于 TiO_2 (P25)，更有利于 CH_4 的生成，从而决定了 SrB_2O_4 催化剂光催化还原 CO_2 合成 CH_4 具有较高的光催化活性。

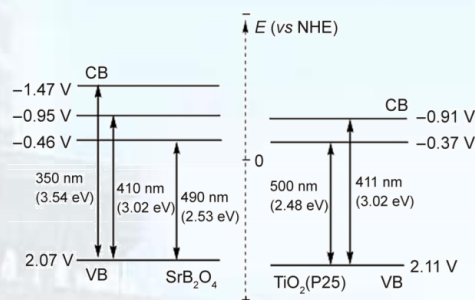


图19. TiO_2 (P25)和 SrB_2O_4 样品的能带结构。

Fig.19. Schematic diagram for the alignment of energy levels of TiO_2 (P25) and SrB_2O_4 samples.

The reduction of carbon dioxide to methane in the presence of water was used to evaluate the photocatalytic activity of a prepared strontium metaborate (SrB_2O_4) catalyst. The strontium metaborate was prepared by a simple sol-gel method, and was shown to exhibit better photocatalytic performance than TiO_2 (P25) under UV-light irradiation. The structure, morphology, and energy levels of the photocatalysts were studied by X-ray diffraction (XRD), Fourier transform infrared (FTIR) spectroscopy, X-ray photoelectron spectroscopy (XPS), transmission electron microscopy (TEM),

photoluminescence (PL) spectroscopy, and UV-Vis diffuse reflectance absorption spectroscopy. It was revealed that the SrB_2O_4 valence band (VB) was located at 2.07V (vs normal hydrogen electrode, NHE), which is more positive than E_0 redox ($\text{H}_2\text{O}/\text{H}^+$) (0.82V (vs NHE)); the conduction band was estimated to be -1.47V (vs NHE), which is more negative than E_0 redox (CO_2/CH_4) (-0.24V (vs NHE)). Therefore, it is clear that strontium metaborate is capable of transforming CO_2 into CH_4 . Moreover, the potential at the bottom of the conduction band for SrB_2O_4 is more negative than that for TiO_2 (P25), leading to a higher deoxidization capacity, which also favors CH_4 formation. Thus, SrB_2O_4 exhibits a higher photocatalytic activity than TiO_2 (P25).

采用溶胶凝胶法制备了In和B共掺杂 TiO_2 催化剂。通过XRD、BET、XPS、漫反射吸收谱和荧光谱对催化剂的结构和性质进行了表征。结果表明：B以间隙式掺杂进入 TiO_2 晶格，而In在表面形成独特的O-In-Cl $_x$ 物种。由于B的间隙式掺杂以及O-In-Cl和 B_2O_3 的表面物种造成了禁带宽度的减小，导致可见光吸收的增强和光生载流子的有效分离。因此In和B双掺杂 TiO_2 催化剂呈现了更好的催化活性。

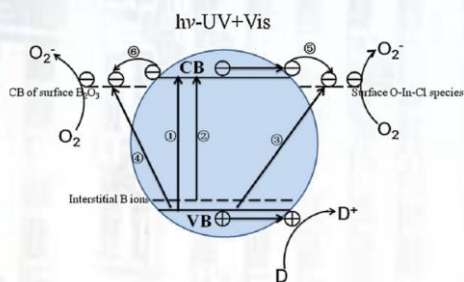


图20. TiO_2 -B-In的能带结构及光催化机理图。

Fig20. Schematic diagram for the band structure of TiO_2 -B-In and the photocatalytic mechanism.

Indium and boron co-doped TiO_2 photocatalysts were prepared by a sol-gel method. The structure and properties of photocatalysts were characterized by XRD, BET, XPS, UV-vis DRS and PL techniques.

It is found that boron is mainly doped into the lattice of TiO_2 in interstitial mode, while indium is present as unique chemical species of O-In-Cl $_x$ ($x = 1$ or 2) on the surface. Compared with pure TiO_2 , the narrowness of band gap of TiO_2 doped with indium and boron is due to the mixed valence band formed by B 2p of interstitial doped B ions hybridized with lattice O 2p. And the surface state energy levels of O-In-Cl $_x$ ($x = 1$ or 2) and B_2O_3 species were located at about 0.4 and 0.3 eV below the conduction band respectively, which could lead to significant absorption in the visible-light region and facilitated the effectually separation of photogenerated carriers. Therefore, indium and boron co-doped TiO_2 showed the much higher photocatalytic activities than pure TiO_2 , boron doped TiO_2 (TiO_2 -B) and indium doped TiO_2 (TiO_2 -In) under visible and UV light irradiation.

采用溶胶-凝胶法制备出 SrB_2O_4 和 SrCO_3 复合催化剂($\text{SrB}_2\text{O}_4/\text{SrCO}_3$)。紫外光催化还原 CO_2 生成 CH_4 的实验证明： $\text{SrB}_2\text{O}_4/\text{SrCO}_3$ 复合催化剂的光催化活性已超过 SrB_2O_4 和 TiO_2 (P25)催化剂。利用X射线电子衍射(XRD)谱、透射电子显微镜(TEM)和等温氮气吸附-脱附分析确定了催化剂的晶相结构、粒子尺寸和比表面积。利用紫外-可见(UV-Vis)漫反射吸收光谱、X射线光电子能谱(XPS)的价带谱和荧光光谱(PL)确定了催化剂的能带结构。结果表明： $\text{SrB}_2\text{O}_4/\text{SrCO}_3$ 复合催化剂异质结构有利于光生载流子的分离，从而抑制了光生电子和光生空穴的复合，提高了光生电子和光生空穴在固液界面参加光催化反应的利用率。因此， $\text{SrB}_2\text{O}_4/\text{SrCO}_3$ 复合催化剂的紫外光催化活性得到了有效的提高。

An $\text{SrB}_2\text{O}_4/\text{SrCO}_3$ composite catalyst is synthesized by the simple sol-gel method. Reduction of carbon dioxide into methane in the presence of water is used to evaluate the photocatalytic activity of the composite

catalyst. $\text{SrB}_2\text{O}_4/\text{SrCO}_3$ exhibits better photocatalytic performance than TiO_2 (P25) and SrB_2O_4 under irradiation with UV light. The crystalline structure, crystallite size, and the BET surface areas of the resultant photocatalysts are studied via the techniques of X-ray diffraction (XRD), transmission electron microscopy (TEM), and nitrogen adsorption-desorption isotherms. The energy levels of the $\text{SrB}_2\text{O}_4/\text{SrCO}_3$ photocatalyst are determined from characterization with UV-Vis diffuse reflectance absorption spectra, X-ray photoelectron spectroscopy (XPS), and photoluminescence (PL) measurements. The heterojunction formed at the $\text{SrB}_2\text{O}_4/\text{SrCO}_3$ interface efficiently promotes photogenerated carrier separation and increases the use of photogenerated carriers in photocatalytic reactions at the solid/liquid interface, resulting in high photocatalytic activity under UV light.

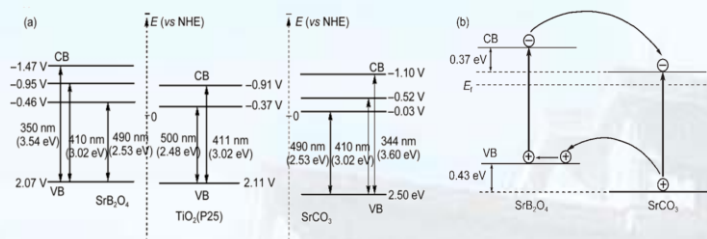


图21. TiO_2 (P25)、 SrCO_3 、 SrB_2O_4 (a)和 $\text{SrB}_2\text{O}_4/\text{SrCO}_3$ (b)样品的能级结构示意图。

Fig21. Schematic diagram for the alignment of energy levels of TiO_2 (P25), SrCO_3 , SrB_2O_4 (a) and $\text{SrB}_2\text{O}_4/\text{SrCO}_3$ (b) samples.

采用溶胶-凝胶法制备出纯 TiO_2 和不同浓度 Sn^{4+} 离子掺杂的 TiO_2 光催化剂($\text{TiO}_2\text{-Snx}\%$, $x\%$ 代表 Sn^{4+} 离子掺杂的 TiO_2 样品中 Sn^{4+} 离子摩尔分数)。利用X射线衍射(XRD)、X射线光电子能谱(XPS)和表面光电电压谱(SPS)确定了 $\text{TiO}_2\text{-Snx}\%$ 催化剂的晶相结构和能带结构,结果表明:当 Sn^{4+} 离子浓度较低时, Sn^{4+} 离子进入 TiO_2 晶格,取代并占据 Ti^{4+} 离子的位置,形成取代式掺杂结构($\text{Ti}_{1-x}\text{Sn}_x\text{O}_2$),其掺杂能级在导带下0.38eV处;当 Sn^{4+} 离子浓度较高时,掺入的 Sn^{4+} 离子在 TiO_2 表面生成金红石 SnO_2 ,形成 TiO_2 和 SnO_2 复合结构($\text{TiO}_2/\text{SnO}_2$), SnO_2 的导带位于 TiO_2

导带下0.33eV处。利用瞬态光电电压谱和荧光光谱研究了 $\text{TiO}_2\text{-Snx}\%$ 催化剂光生载流子的分离和复合的动力学过程,结果表明: Sn^{4+} 离子掺杂能级和表面 SnO_2 能带存在促进光生载流子的分离,有效地抑制了光生电子与空穴的复合;然而, Sn^{4+} 离子掺杂能级能更有效地增加光生电子的分离寿命,提高了光生载流子的分离效率,从而揭示了 $\text{TiO}_2\text{-Snx}\%$ 催化剂的光催化机理。

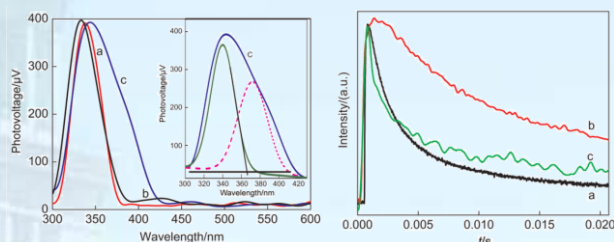


图22. TiO_2 (a)、 $\text{TiO}_2\text{-Sn5}\%$ (b)和 $\text{TiO}_2\text{-Sn50}\%$ (c)的表面光电电压谱和瞬态光电电压谱。

Fig22. SPS spectra and transient photovoltage spectra for TiO_2 (a), $\text{TiO}_2\text{-Sn5}\%$ (b), and $\text{TiO}_2\text{-Sn50}\%$ (c).

Pure TiO_2 and Sn^{4+} doped TiO_2 ($\text{TiO}_2\text{-Snx}\%$) photocatalysts were prepared by a sol-gel method, where $x\%$ represents the nominal molar fraction of Sn^{4+} ions in the TiO_2 structure. The crystal structure and energy band structure of the resultant catalysts were characterized by X-ray diffraction (XRD), X-ray photoelectron spectroscopy (XPS), and surface photovoltage spectroscopy (SPS). The results show that for a low content of Sn^{4+} ions, the Sn^{4+} ions are doped into the TiO_2 lattice and replace lattice Ti^{4+} ions in a substitute mode ($\text{Ti}_{1-x}\text{Sn}_x\text{O}_2$). The energy levels of these Sn^{4+} ions are located 0.38eV below the conduction band. Moreover, the rutile SnO_2 crystal structure evolves with increasing content of Sn^{4+} ions, i.e., a $\text{TiO}_2/\text{SnO}_2$ structure is formed. The conduction band of SnO_2 is located 0.33eV lower than that of TiO_2 . The separation and recombination mechanism of the photo-generated carriers was characterized by photoluminescence and transient photovoltage techniques. The results showed that the

formation of the energy levels of Sn^{4+} ions and the conduction band of rutile SnO_2 can enhance the separation of the photogenerated carriers, and suppress the recombination of photo-generated carriers. However, the energy levels of Sn^{4+} can lead to a much longer life time and higher separation efficiency of the photo-generated carriers. For different content of Sn^{4+} in Sn^{4+} ion doped TiO_2 ($\text{TiO}_2\text{-Sn}x\%$), the above mentioned aspects improve the photocatalytic activity.

采用溶胶-凝胶法制备出 Si^{4+} 离子掺杂的 TiO_2 可见光催化剂 ($\text{TiO}_2\text{-xSi}$), 该催化剂的可见光催化活性高于纯 TiO_2 。利用XRD、XPS、FT-IR和UV-Vis DRS等表征技术, 研究了 $\text{TiO}_2\text{-xSi}$ 催化剂的晶体结构、能带结构和表面性质。研究发现: 掺入 Si^{4+} 离子在 TiO_2 粒子表面主要形成 Ti-O-Si 物种, 并在价带上 0.2-0.6 eV区域形成 Si^{4+} 离子掺杂的表面态能级, 该表面态能级的存在是 $\text{TiO}_2\text{-xSi}$ 催化剂产生可见光响应, 实现可见光催化的根本原因; 并进一步讨论了 $\text{TiO}_2\text{-xSi}$ 催化剂可见光催化降解对氯苯酚的机理。

doped silicon ions formed Si-O-Ti bonds on the surface of TiO_2 particles. And thus, surface state energy attributed to the silicon dopant was located at 0.2-0.6eV below the conduction band of TiO_2 , which enhanced the response to the visible light and photocatalytic ability. It was also discussed the $\text{TiO}_2\text{-xSi}$ samples' mechanism of photocatalytic degradation of 4-chlorophenol.

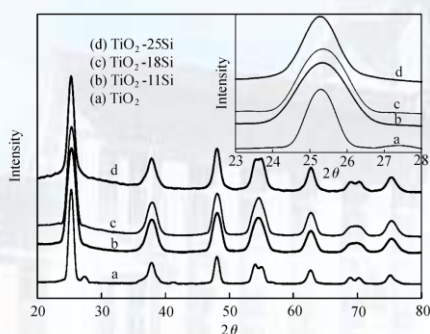


图23. TiO_2 和 $\text{TiO}_2\text{-xSi}$ 样品的XRD谱图, 插图为各样品在 $2\theta=25.3^\circ$ 附近的衍射峰。

Fig23. XRD patterns of TiO_2 and $\text{TiO}_2\text{-xSi}$ samples, the inset shows the enlarged version of the peak near 25.3° .

TiO_2 photocatalysts ($\text{TiO}_2\text{-xSi}$) doped by different contents of silicon were prepared by a sol-gel method. The catalysts exhibited a better photocatalytic ability than the pure TiO_2 . The samples were characterized by XRD, XPS, FT-IR and UV-Vis diffuse reflectance absorption spectra. It was revealed that the

弱光非线性及量子相干光学/ Weak Light Nonlinear Optics and Quantum Coherent Optics

负责人：许京军

本方向主要开展纳微结构制备及其光学性质、非线性光调控与应用、量子非线性光学、飞秒超快探测技术以及光折变材料与新效应等方面的研究。2013 年度本方向共发表论文 46 篇，主要取得如下进展：

The main research topics in this group are fabrication and optic properties of nano/micro-structure, nonlinear optical manipulation and its applications, quantum nonlinear optics, ultrafast detection and analysis by using fs technology and photorefractive materials and nonlinear optics. We published 46 papers in various academic journals. The main research progresses in 2013 are as follows.

表面等离子激元在光通信、光传感等领域都有重要的潜在应用。而主动调控将对表面等离子激元的应用起到关键作用。传统的表面等离子激元主要基于贵金属，但是贵金属由于性质过于稳定，因此表面等离子激元的控制主要源自于外部环境的改变。石墨烯作为新型的等离子激元材料，其性质可以通过电或者化学方法实现掺杂，从而能实现等离子激元的主动调控。在本工作中，我们提出了在异质石墨烯条对中，利用电掺杂来改变其中一个石墨烯带的费米能级，从而改变其载流子浓度，实现石墨烯带对中耦合表面等离子激元的模式的改变。在非对称的情况下，除了存在对称耦合模式，反对称模式同样出现，利用该现象可以实现光学近场在石墨烯带中的空间调控。同时石墨烯纳米带对的间隙对于光调控具有重要作用。较小的间隙能实现强的调控。

The spatial switching of mid-infrared light near-fields is proposed in coupled graphene heterogeneous ribbon pairs. By using the coupled plasmon modes in graphene ribbon pairs, the electric near-field enhancement can be spatially controlled in graphene ribbons as the tuning of the external

bias voltage difference. More specifically, due to symmetry breaking, the anti-symmetrically coupled dipolar plasmons exist except for the symmetrically coupled modes in homogeneous graphene pairs. Moreover, the gap distance is one of the key parameters for switching of electric near-fields, strong coupling means the efficient control of near-fields.

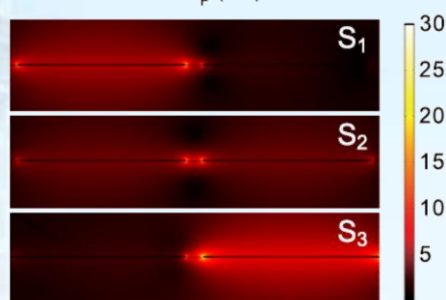


图1. 石墨烯条对在不同费米能级差的光学近场分布图。

Fig1. The electrical near-field distribution for graphene ribbon pairs with different Fermi energy differences..

在工作中我们研究了亚波长石墨烯楔形与沟槽波段中的表面等离子激元模式，该模式位于太赫兹-红外频率波段。该结构中的等离子激元模式按照对称性可以分为完美电导体与完美磁导体对称模式，分别具有不同的传播特性。这些模式的能流分别聚集在石墨烯波导的不同位置，并且这些模式从物理上可以通过折叠的石墨烯带模式来解释。同时，我们还研究了楔形与沟槽波导结构中边缘长度以及石墨烯本身的掺杂对这些模式的影响。总之，该研究对集成光路的进一步研究具有一定意义。

Surface plasmon modes at terahertz-infrared waveband in subwavelength graphene wedge and groove waveguides are investigated, which can be categorized into perfect electric conductor and perfect magnetic conductor symmetric modes with different propagation characteristics. The electromagnetic near-fields are localized strongly in different regions for these two

kinds of modes. Moreover, these modes can be interpreted by the folded graphene ribbon modes. The brim width of the waveguides and the Fermi energy of the graphene strongly influence the dispersion and propagation distances of the plasmon modes, which can be used for tuning the plasmon modes in graphene wedge and groove waveguides efficiently.

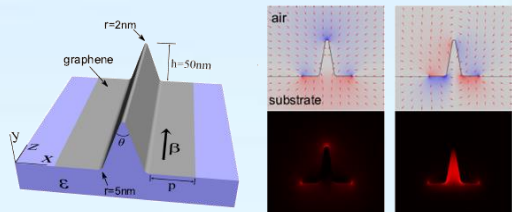


图2. 石墨烯楔形波导与低阶完美电导体与磁导体对称模式。

Fig2. The first-order PEC and PMC symmetric plasmon modes in graphene wedge waveguides.

集成光路中的全光信号处理中要求实现光控光。传统的全光器件中存在两个主要的缺点：较大的尺寸与高的操作光强。表面等离子激元作为金属-介质表面传播电子与电磁场的耦合，不但能将光局域在纳米尺度，而且能实现电磁场的强局域。因此将表面等离子激元应用到全光期间中，能很好的弥补传统全光器件的缺点。在本工作中，我们提出了在金属-介质-金属波导构造布拉格谐振腔，将非线性介质置于该腔中，从而实现光学双稳。利用时域有限差分方法结合艾利方程，我们发现高 Q 值的腔能实现更高的透射，并且具有较窄的迟滞回路；同时该布拉格腔的响应时间能达到皮秒量级。我们提出的光学双稳装置在实验室较容易构造，对未来的光学通讯和光学计算有一定的意义。

An optically bistable device based on a Bragg grating resonator with a nonlinear medium in metal-insulator-metal waveguides is proposed. Its properties are numerically investigated by a finite-difference time-domain method and further qualitatively analyzed by adopting Airy equation. Cavities with different Q factors are compared with respect to bi-stability. Cavities with a small Q

factor lead to a high transmission and a narrow hysteresis loop. The response time of such cavities is found to be in the sub-picosecond region. Our nano-scale switching structure is comparatively easy to fabricate and integrate in plasmonic circuits and promises to be useful for future all-optical computing and communication technology.

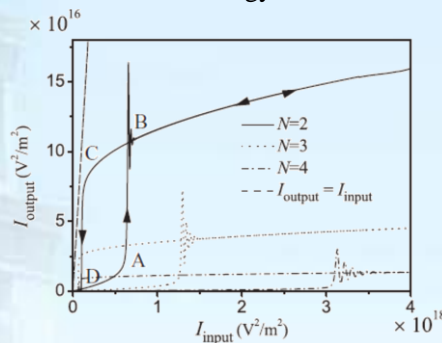


图3. 光学双稳腔的入射-出射关系图。对应于对于不同周期数 N=2, 3, 4 的迟滞回线。

Fig3. Input-output light intensity in optical bistable cavities with N=2, 3, 4, respectively.

我们在一种包含了金属-电解质-金属波导与矩形腔的表面等离子激元结构中研究了 Fano 共振。Fano 共振来源于矩形腔中局域的四极子模式与宽谱间的干涉。通过调节矩形腔的长度以及宽度可以调节 Fano 共振的谱线形貌。这种纳米结构可以作为一种优良的纳米传感器，其灵敏度可以达到 530 nm/RIU，FOM 值可以达到 650。

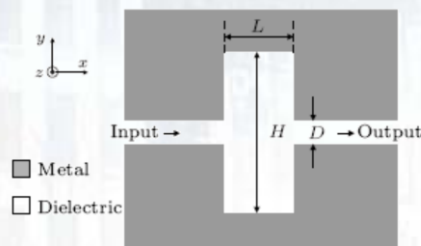


图4. 对称的表面等离子激元的结构示意图。

Fig4. Schematic diagram of the symmetric plasmonic structure.

A novel symmetric plasmonic structure consisting of a metal-insulator-metal waveguide and a rectangular cavity is proposed to investigate Fano resonance performance by adjusting the size of the structure. The Fano resonance originates from

the interference between a local quadrupolar and a broad spectral line in the rectangular cavity. The tuning of the Fano profile is realized by changing the size of the rectangular cavity. The nanostructure is expected to work as an excellent plasmonic sensor with a high sensitivity of about 530 nm/RIU and a figure of merit (FOM) of about 650.

我们研究了金属纳米粒子边角效应对消光谱线的影响。目前，由几何微妙的变化引起的，尤其是棱角的圆弧金属纳米粒子的光学响应，已引起了研究人员的极大兴趣。在外边缘倒圆的金粒子和金粒子二聚体间的距离可以用离散偶极子近似方法来研究其对光学性能的影响。研究证明金的纳米粒子的光学性质是内边缘倒圆比外边缘倒圆更敏感，比如如偶极的蓝移，纳米粒子二聚体的四极共振。与金属纳米粒子二聚体的内边缘倒圆的比较，我们发现，外边缘的钝化引起的四极模式的较大的位移和偶极子模式的近似偏移。

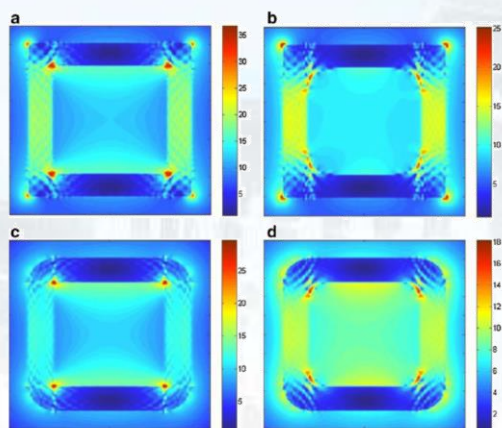


图5. 纳米粒子的电场分布图。a $R_o=R_i=0$ nm ($\lambda=658$ nm); b $R_o=0$ nm and $R_i=6$ nm ($\lambda=640$ nm); c $R_o=6$ nm and $R_i=0$ nm ($\lambda=629$ nm); and d $R_o=R_i=6$ nm ($\lambda=614$ nm)。

Fig5. The electric field distribution of nanobox with a $R_o=R_i=0$ nm ($\lambda=658$ nm), b $R_o=0$ nm and $R_i=6$ nm ($\lambda=640$ nm), c $R_o=6$ nm and $R_i=0$ nm ($\lambda=629$ nm), and d $R_o=R_i=6$ nm ($\lambda=614$ nm)

The optical responses of metal nanoparticles induced by subtle variations in geometry, especially by the rounding of the edges and corners, have generated great

interest at present due to the requirement of fabricating refined structures of metal nanoparticles and theoretical simulations of the real particles. We study the effect of both inner and outer edge rounding on the optical properties of gold nanobox and gold nanobox dimer with small inter particle distances by using the discrete dipole approximation method. The shift of extinction peaks, the electric field distribution, and the variation of refractive index sensitivities by changing the curvature of the inner and outer edges of gold nanobox are investigated. We demonstrate that the optical properties of nanobox are more sensitive to the outer edge rounding than the inner edge rounding. By edge rounding of two very close gold nanoboxes, the blue shift of the dipolar and the quadrupolar plasmonic resonances of nanobox dimer are shown. Comparing with the inner edge rounding of nanobox dimer, we find that rounding of the outer edges causes the larger shift of the quadrupolar mode and approximate shift of the dipole mode.

等离子体超材料的一个重要应用为实现外界折射率的传感，目前已经取得很多成果。超材料折射率传感器主要有两种工作模式：1 波长传感模式，即通过检测超材料共振波长随外界折射率的移动，得到外界折射率的变化信息。这样的传感器内应集成宽带光源与光谱仪以实现光谱的测量与峰位判断，这增加了系统复杂性与信号采集处理时间；2 光强传感模式，即检测超材料某一特定波长下透（反）射光强随外界折射率的变化，实现对于折射率的检测。相比于波长传感模式，该模式只需要使用单色光源与功率探头，系统简单且信号采集处理速度快，但测量范围受到光谱曲线中临近峰-谷波长距离的限制。已报道的超材料传感器往往只可工作于上述一种工作模式中。并且为了提高传感器的灵敏度，大多数超材料采用非对称的结构设计，以实现较锐的共振峰。但非对称的结构结构设计使得其光学性质依赖于

偏振方向,如此需要使用偏振片对于入射光起偏,并且偏振方向需要同超材料满足特定的取向要求,带来了不必要的麻烦。本文设计了一种基于各向同性螺旋结构设计的折射率变化传感器。由于采用了各向同性结构设计[图 6 (a)],其光谱性质不依赖于入射光的偏振,且该结构透射光谱同时具有尖锐共振峰[图 6 (b) 中 A]和很宽的光谱线性斜坡[图 6 (b) 中红色虚线],可分别实现波长传感模式与光强传感模式。利用尖锐的共振透射峰 A 随着外界折射率变化的移动,实现了灵敏度达 410nm/RIU[图 6 (d)]的波长模式传感。另外,通过监测 833nm 处透射光强的变化,灵敏度为 147%/RIU[图 6 (e)]的折射率传感得以实现,且其测量范围可达 $\Delta n=1.5$,该测量范围可以满足对于大多数液体折射率的测量。

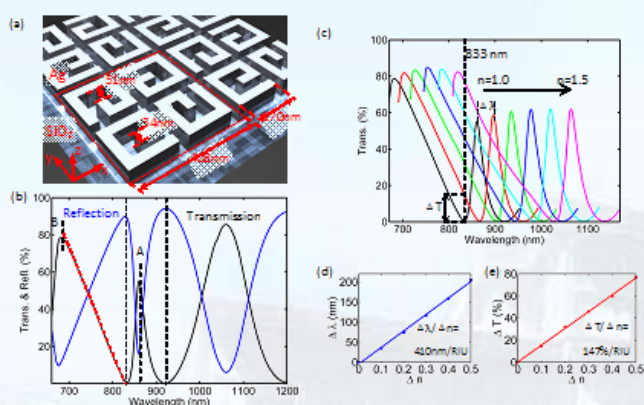


图6. (a) 各向同性螺旋结构超材料。(b) 超材料的透射与反射光谱。(c) 超材料透射光谱随着外界折射率的变化。(d, e) 超材料的波长与光强模式传感性能。

Fig6. (a) Isotropic spiral plasmonic metamaterial. (b) The transmission and reflection spectra of the metamaterial. (c) The spectral shift of the metamaterial induced by surrounding refractive index increase from 1.0 to 1.5. (d) The spectral interrogation and intensity interrogation sensing modes of the

In recent years, the interdisciplinary field between metamaterials and refractive index sensing technology has become a fertile and active area. Two of the most commonly used plasmonic sensing techniques include spectral (wavelength) interrogation and intensity interrogation technique. In the former case, the refractive index change of the surrounding

medium is derived through measuring the spectral shift. In such a configuration, broadband light sources and spectra analyzers are needed. In the latter situation, people derive the environmental refractive index by measuring the intensity variations from transmitted/reflected monochromatic beams. This has the benefit of a more compact detection scheme, which removes the need for a spectrometer. Generally speaking, the dynamic ranges for the wavelength interrogation sensors are mostly limited by the spectral ranges of the spectrometers adopted in the detection scheme. However, for intensity interrogation sensors, the dynamic range is dependent on the interval between the operating wavelength and its neighboring spectral peak/valley position. The most of the present plasmonic sensors work in the spectral interrogation configuration. And in order to improve sensing performance, most of the sensors are based on non-centrosymmetric structure designs to obtain sharper resonances, in which the induced birefringence puts strict requirement on the alignment of the polarization direction of incident light with the sensor orientation. Here we demonstrate numerically a isotropic spiral G-shaped plasmonic metamaterial (shown in Fig. 6(a)), in which both an arrow transmission resonating mode with a high-quality factor (Q factor) (indicated by A in Fig. 6(b)) and a broad resonance with a long linear slope (dash line in Fig. 6(b)) can be achieved simultaneously. Both spectral shift sensing and single wavelength operating abilities are demonstrated by this planar metamaterial (see Fig. 6(c)). By utilizing the high-Q resonance, our plasmonic device gives a spectral shift sensitivity as large as 410 nm/RIU (Fig. 6(d)). By detecting transmittance change ΔT at 833nm, sensing with the sensitivity of 153%/RIU (Fig. 6(d)) is achieved, and the

dynamic range remains about 0.5 RIU, which is sufficient to identify most of the chemical liquids.

我们进行了大面积自组装金属微结构制作、光学性质及表面增强拉曼散射 (SERS) 性能的研究。虽然支持表面增强拉曼散射 (SERS) 的贵金属纳米间隙结构可以用来检测单分子,但是由于缺乏可控重现的纳米制造技术限制了该技术的实际应用。可以通过 Au 膜沉积的蝉翼,设计出纳米柱结构的有序阵列的翅膀,形成大面积的高性能 SERS 基底。通过 Au 膜沉积到蝉翼的厚度以及相邻的纳米柱间隙大小的控制,可以在 SERS 衬底与小于 10 纳米间隙中获得的最高的拉曼增强因子 (EF) 大于 2×10^8 。利用这种办法制作模板的蝉翼使我们大面积高性能的 SERS 衬底在化学/生物传感应用中有极大的优势。

Noble metal nanogap structure supports strong surface-enhanced Raman scattering (SERS) which can be used to detect single molecules. However, the lack of reproducible fabrication techniques with nanometer-level control over the gap size has limited practical applications. In this letter, by depositing the Au film onto the cicada wing, we engineer the ordered array of nanopillar structures on the wing to form large-area high-performance SERS substrates. Through the control of the thickness of the Au film deposited onto the cicada wing, the gap sizes between neighboring nanopillars are fine defined. SERS substrates with sub-10-nm gap sizes are obtained, which have the highest average Raman enhancement factor (EF) larger than 2×10^8 , about 40 times as large as that of commercial Klarite® substrates. The cicada wings used as templates are natural and environment-friendly. The depositing method is low cost and high throughput so that our large-area high-performance SERS substrates have great advantage for chemical/biological sensing applications.

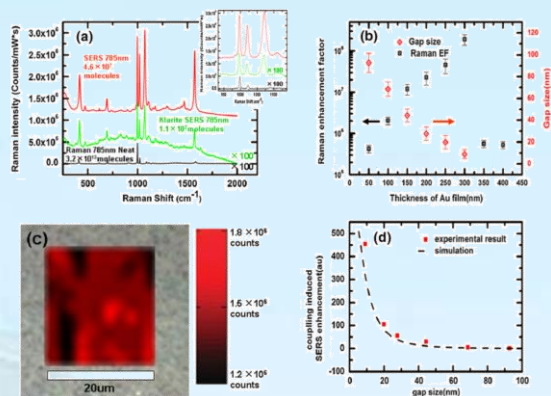


图7. 比较基板和苯硫基, 平均EF和间隙大小, 空间图形, 以及实验和COMSOL模拟。(a) 基板CW300 (红色) 的表面增强拉曼光谱与 Klarite® (绿色) 以及在785 nm波长激发下的苯硫基拉曼光谱 (黑色) 的比较。苯硫醇中每个测量探测分子的数目被表示在图中。插图表示靠近1,000 /厘米的三种主要方式的放大光谱 (b) 与沉积在蝉翼的金膜厚度与表面增强拉曼光谱强度的关系图, EFs为黑色方框和邻近的间隙的纳米柱红色菱形。(c) 在一个面积比20微米×20微米大的SERS衬底中CW300的998/cm空间映射。背景是通过显微镜用×50物镜拍摄基板CW300的光学反射图像。(d) 拉曼增强 (黑色虚线) 和实验的平均EFs (红色方块) 作为相邻的纳米柱之间的间隙大小的函数平均值的COMSOL模拟图。

Fig7. Comparison of substrates and neat benzene thiol, average EFs and gap sizes, spatial mapping, and COMSOL simulations. (a) Comparison of the SERS of substrates CW300 (red), Klarite® (green), and neat Raman spectra (black) of benzene thiol collected at 785-nm incident. The number of molecules of benzene thiol that each measurement is probing is denoted in the figure. Inset: zoomed-in region of the spectra showing the three primary modes located near 1,000/cm, with the 998/cm used for calculation of the SERS enhancement factor. Note that the SERS of the Klarite® substrate and the neat spectra have been multiplied by a factor of 100 for easier direct comparison. (b) Average EFs (black open squares) and gap sizes between neighboring nanopillars (red open rhombuses) as function of gold film thickness deposited on the cicada wing. (c) Spatial mapping of the SERS intensity at 998/cm of SERS substrate CW300 over an area larger than $20 \mu\text{m} \times 20 \mu\text{m}$. The background is the optical reflection image of substrate CW300 photographed through a microscope with a $\times 50$ objective. (d) COMSOL simulations of SERS enhancement (black dash) and the mean of experimental average EFs (red squares) as function of gap size between neighboring nanopillars. All data points are normalized to the corresponding value of SERS enhancement of CW50

当飞秒激光作用到硅材料上时,在一定条件下,可以形成一种新型的材料,我们通常称之为飞秒微构造硅或者黑硅。其表面形

成如图 8 左图所示的微纳结构。飞秒微构造硅有很多特殊的性质, 例如其光吸收率从紫外到红外都很高 (大于 90%), 如图 8 右图所示。

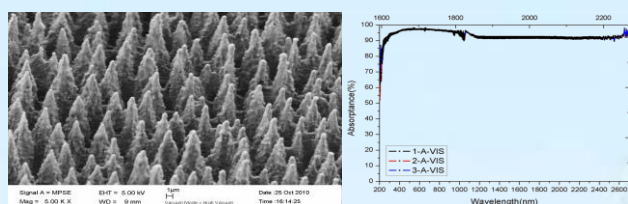


图8. 左图: 飞秒微构造硅表面形貌; 右图: 典型的吸收曲线。

Fig8. Left: Surface morphology of femtosecond laser microstructured silicon; Right: the typical absorptance curve

When femtosecond laser pulses irradiate silicon samples, a new kind of material called femtosecond laser microstructured silicon (FLMS) or black silicon can be produced under some conditions. Some micro/nano structures are produced in the silicon surface as shown in Fig. 8L. FLMS has some interesting extraordinary properties, for example, the absorptance is very high, more than 90%, from UV to IR, as shown in Fig. 8R.

飞秒微构造硅是一个复杂的超快过程。一方面大量的电子、硅离子、硅原子以及硅纳米颗粒及团簇飞离硅表面形成等离子体羽流, 另一方面在硅表面同时也发生了一系列的超快物理过程; 二者共同作用, 导致微纳结构的形成及表面性质的变化。我们分别对离开硅表面的等离子体和硅表面的进行研究。

通过稳态光谱我们可以知道等离子体的成分, 以及不同条件 (气氛、压强、能流密度等) 间的关系和影响。如图 9 中左图所示, 等离子体羽流所含的主要粒子是硅原子和硅离子, 并且还含有背景气体所含元素的原子或离子。这说明, 飞秒激光作用期间, 不仅硅被电离, 而且, 在硅等离子体羽流喷发扩散的过程中, 碰撞也导致了背景气体的分解、电离。这使硅与背景气体之间的潜在化学反应得以发生。在 SF_6 中, 高温等离子体环境下, SF_6 的分解将易于导致如下化学反应: $\text{F} + \text{Si} \rightarrow \text{SiF}_4 \uparrow$ 。而硫原子则有很大几率

进入处在晶格破裂、重建的硅表面, 实现过饱和掺杂。图 9 右图表明, 等离子体羽流的光辐射强度受到背景气体限域效应的影响, 更强的限域效应抑制羽流扩散, 增强了光辐射。全光谱积分强度和 413.1 nm Si II 谱线强度均对激光能流密度和背景气氛种类表现出相似依赖性。四种背景气体的限域效应强度有如下关系: $\text{SF}_6 > \text{Air} > \text{N}_2 > \text{V}$ 。

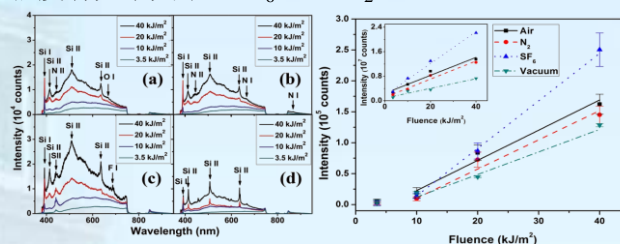


图9. 左图: 不同入射能量下的等离子体稳态谱(a)100-kPa air, (b) 70-kPa N_2 , (c) 70-kPa SF_6 , and in (d) vacuum (<1 Pa); 右图: 发射强度和入射能流密度的关系。其中大图是413.1 nm Si II的结果, 插图是光谱全积分的结果。

Fig9. Left: Emission spectra of a plasma with different fluences (a)100-kPa air, (b) 70-kPa N_2 , (c) 70-kPa SF_6 , and in (d) vacuum (<1 Pa). Right: The fluence dependence of emission intensity of the 413.1 nm Si II line for different ambient gases. The inset shows the fluence dependence of the integral intensity of the whole spectrum. The straight lines represent linear fits

The process of FLMS is ultrafast and complicated. On the one hand, a large amount of electrons, silicon ions, atoms, nanoparticles, and clusters are ejected from the silicon surface to form plasma plume; on the other hand, there are a series of ultrafast processes in the silicon surface. The two factors lead to the microstructures formation and the changes of surface properties. We studied the process of FLMS separately for the plasma plume and that on the silicon surface.

By the steady state spectroscopy, we can determine the plasma composition and investigate the relationship among the laser fluence, ambient gases, gas pressure and so on. As shown in Fig. 9L, the plasma plume mainly contains silicon atoms and monovalent ions. Furthermore, signals of N and O are observed for air, N for nitrogen and S and F for SF_6 atmosphere. This suggests that

ambient gas molecules are dissociated during laser ablation, which leads to the potential chemical reaction between silicon and ambient gas. In SF_6 , the SF_6 molecules are dissociated in the hot plasma, easily causing the chemical reaction: $\text{F} + \text{Si} \rightarrow \text{SiF}_4 \uparrow$. Moreover, due to the destroying and rebuilding of the silicon lattice, it is more possible for the sulfur atoms to enter the silicon surface and realize the highly doping. During the expansion of the plasma plume, the ambient gas can suppress it. This kind of confinement effect enhances the optical emission of the plume. As seen in Fig. 9R, the integral intensity of the whole spectrum and the intensity of the 413.1 nm line both represent the similar dependence with the laser fluences and with the ambient gases. The results suggest that the confinement of the different ambient gases exhibit a relationship: $\text{SF}_6 > \text{Air} > \text{N}_2 > \text{V}$.

通过时间分辨光谱, 我们可以研究等离子羽流的演化过程。图 10 左为 SF_6 气氛下等离子体时间分辨光谱。我们发现, 羽流光辐射的衰减存在两个过程。其中较快的过程对应韧致辐射, 较慢的过程对应受激原子或离子的跃迁辐射。由双指数拟合分别得到两个衰减过程的寿命, 它们均受到能流密度和背景气氛的影响, 如图 10 右图所示。背景气氛限域效应的强度不同, 造成不同气氛下羽流光辐射寿命的不同。不同气氛中, 快、慢两个衰减过程的寿命均有如下关系: $\text{SF}_6 > \text{Air} > \text{N}_2 > \text{V}$ 。限域效应不仅会影响等离子体的扩散, 从而影响其光辐射的强度和寿命; 还会导致喷出物的再沉积。在不同气氛下, 再沉积的强度和沉积物的大小均有不同, 这使得后续激光脉冲所遭遇的表面情况有所差异, 从而影响作用过程, 因此在这种反馈机制作用下, 多个脉冲后, 逐渐形成不同的微纳结构。需要指出的是, SF_6 气氛具有最强的限域效应, 本应有更强的再沉积过程。然而由于化学反应生成的易挥发的 SiF_4 大大减弱了再沉积效应, 所以反而形成更光滑、更尖锐的锥结构。

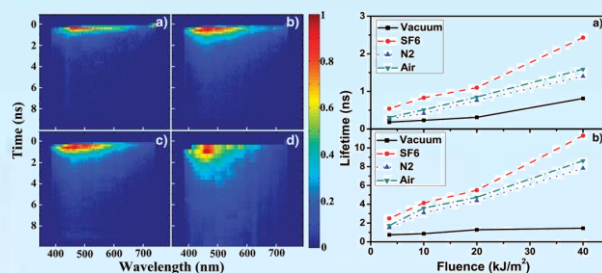


图10. 左图 SF_6 气氛下不同激光通量的等离子体时间分辨光谱: (a) 3.5 kJ/m^2 , (b) 10 kJ/m^2 , (c) 20 kJ/m^2 , and (d) 40 kJ/m^2 .; 右图: 505.6 nm Si II 线在不同气氛下不同入射通量下的寿命。

Fig10. Left: Time-resolved spectra of the plasma measured in SF_6 under different laser fluences: (a) 3.5 kJ/m^2 , (b) 10 kJ/m^2 , (c) 20 kJ/m^2 , and (d) 40 kJ/m^2 . Right: The dependence of the lifetime of the 505.6 nm Si II line on laser fluence for different ambient gases. (a) lifetime τ_1 of the fast process; (b) lifetime τ_2 of the slow process

By time-resolved spectroscopy, we can study the ultrafast dynamic processes of the plasma. Figure 10L shows the time-resolved spectra of the plasma plume in SF_6 . We observe that the decay of the spectral intensity consists of two processes: a fast decay and a slow decay, which correspond to the bremsstrahlung radiation and the recombination radiation respectively. The decay profile can be well fitted with a bi-exponential function so that we obtain two decay time constants. They are both affected by the laser fluence and the ambient gases, as shown in Fig. 10R. The different confinements cause the different lifetimes of the optical emission of the plume in various ambient gases. The lifetimes of the two decay processes for different ambient gases exhibit a relationship: $\text{SF}_6 > \text{Air} > \text{N}_2 > \text{V}$. Besides, the confinement can cause the redeposition of the ejected materials. In various ambient gases, the different confinements lead to the different redeposition intensity and the different sizes of the redeposited materials. As a result, the surface morphologies are different for every successive pulse, leading to the different ablating processes in various ambient gases. Finally, the distinct microstructures are formed

by this kind of feedback mechanism. Although the confinement of the SF_6 is the strongest, the formation of the volatile SiF_4 significantly weakens the redeposition effect, leading to the sharper and smoother micro-cones.

对羽流性质和演化过程的研究,使我们弄清了背景气氛对作用过程的影响,以及形成不同微结构的原因。同时,我们继续探究了飞秒激光脉冲辐照硅期间及之后,硅表面所发生的物理过程。当 100 飞秒的激光脉冲照射到硅上的时候,电子和晶格对光的响应速度是不一样的,在亚皮秒时间尺度,二者处在强烈的非平衡态,这时候需要用双温模型来模拟这个过程。大量的电子会在几百飞秒激发到导带,如图 11 左所示。这时候硅表现出来的应该是金属的性质而不是半导体。因此我们把 Drude 模型引入到双温模型中,形成新的物理模型——TTM-Drude 模型,用以解释初期周期性条纹的产生机制。实验观测到条纹周期为 $746 \pm 34 \text{ nm}$,而采用该理论模型模拟的结果为 755 nm ,二者非常吻合。

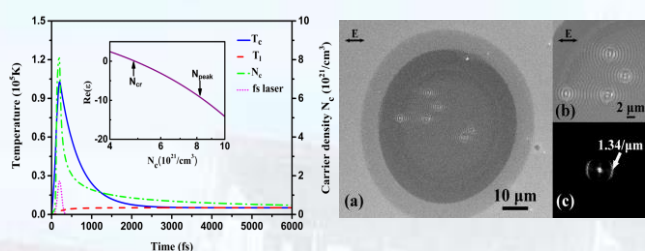


图11. 左图: 载流子浓度(绿线)、载流子温度(蓝线)、晶格温度(红线)的演化过程。紫线是激光脉冲。插图演示了介电常数从半导体到金属性的转变。右图: 单脉冲激光照射硅表面形成fs-LIPSS的结果。与理论计算相符。

Fig11. Left: Evolution of carrier density N_c (green dash dot curve), carrier temperature T_c (blue solid curve) and lattice temperature T_l (red dash curve) calculated for laser fluence $F = 1.6 \text{ J/cm}^2$. The purple dot curve shows the laser pulse whose duration is 120 fs. The insert shows a relationship between N_c and the real part of dielectric constant, where N_{cr} is critical carrier density and N_{peak} is the peak value of the N_c . Right: The SEM image of the nanoparticle-covered silicon surface irradiated (in vacuum) by a single femtosecond laser pulse where laser fluence $F = 1.6 \text{ J/cm}^2$. (b) Details of fs-LIPSS formed on the sample surface. (c) 2D-FFT spectrum of Fig. 11(b). The arrows represent laser polarization direction

The studies of the properties and evolution of the plasma plume make us to

clarify the ambient effect and the mechanism of the formation of the different microstructures. Meanwhile, we studied the physical processes occurring in the silicon surface during the interaction between femtosecond laser and silicon. When silicon is irradiated by a fs-laser pulse, the response time of carriers and lattice are different. After fs-laser pulse irradiation, electrons and lattices are in an extremely nonequilibrium state on the timescale of subpicosecond. Hence, it can be treated as a two-temperature model. As shown in Fig. 11L, the surface carrier density is very high, which changes surface optical properties from semiconductor to metallic-like. Therefore, the Drude model should be introduced to modify TTM, aiming to explain the mechanisms of the laser-induced periodic surface structures (LIPSS). A finite difference method (FDM) is employed to numerically solve the TTM-Drude equations. The theoretical computation derives the period of the LIPSS is 755 nm that is close to the experimental result of $746 \pm 34 \text{ nm}$. The excellent consistency proves our model is available.

基于上面的研究,我们认为单个飞秒激光脉冲构建 LIPSS 是由于入射激光与粗糙表面激发的 SPPs (飞秒激光导致的表面金属性) 干涉导致的载流子空间周期分布,使得硅表面的光吸收率呈现出周期性分布,在电子浓度高的区域更容易发生电子的逃逸、硅原子及硅离子的逃逸,引起更强烈地刻蚀,最终形成垂直于入射激光偏振方向的周期性条纹。然而,如果能量过高,剧烈的超快相变或超快热熔过程会引起表面的消融作用,抑制 LIPSS 的产生。我们从实验上观测到了这个竞争过程,如图 12 所示。在截面能量高斯分布的光斑中心,没有发现周期性条纹的产生,而是出现类似气泡破裂导致的火山口状的结构。我们认为这是由于光斑中心过高的能流密度引起剧烈的相变,晶格温度的快速上升(图 12 左)导致表面快速熔

化,在熔化过程中产生的气泡发生破裂,形成冲击波,最终形成环状的火山口结构并抑制了周期性条纹的产生。多个脉冲作用后,也有类似的情况,如图 13 所示。高能量脉冲作用下,光斑中心没有形成条纹,而边缘形成条纹。如果降低激光脉冲能量,则在光斑中心也能形成条纹。这些结果说明超快熔化的强度决定着条纹的形成或消失,在该竞争机制中起到决定性作用。

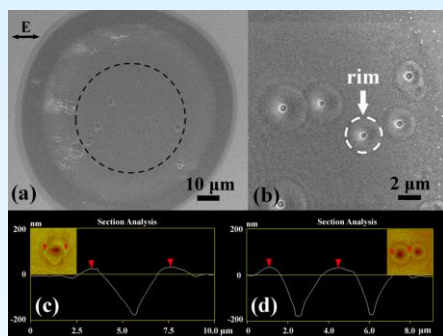


图12. (a) 入射激光能流 $F = 6.7 \text{ J/cm}^2$ 时,硅表面形貌SEM图。在灰圈中没有LIPSS出现,只有类似于火山口的形状。(b) $F = 6.0 \text{ J/cm}^2$ 的双火山口。(c)和(d)是上图的AFM图。

Fig12. (a) The SEM image of the nanoparticle-covered silicon surface irradiated (in vacuum) by a single femtosecond laser pulse where laser fluence $F = 6.7 \text{ J/cm}^2$. Inside the dashed circle, only some bubble-like pits are formed; out of the dashed circle, fs-LIPSS appear. (b) Bubble-like pits with similar size are observed in the central region of a damage spot irradiated by a single pulse with $F = 6.0 \text{ J/cm}^2$. (c) and (d) are the AFM images of the craters corresponding to Fig. 12(a) and (b) respectively. The arrows represent laser polarization direction.

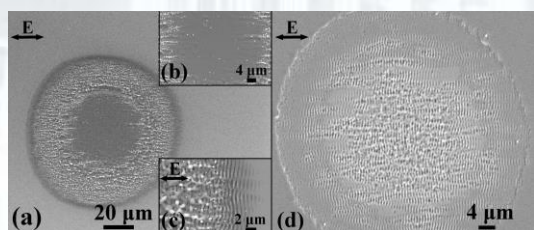


图13. 五个脉冲照射下的SEM图。(a) 脉冲作用的全景图, $F = 6.7 \text{ J/cm}^2$ 。(b),(c)是(a)图的中心和边缘。(d) $F = 1.6 \text{ J/cm}^2$ 的作用情况。

Fig13. The SEM image of the nanoparticle-covered silicon surface irradiated by five pulses (in vacuum). (a) a damage spot with $F = 6.7 \text{ J/cm}^2$. (b)-(c) the central region and periphery of Fig. 13(a). (d) a damage spot with $F = 1.6 \text{ J/cm}^2$.

Based on our research, we propose that the production of LIPSS is due to the spatial modulation of carriers produced by the

interaction of incident laser and the SPPs. It leads to a spatial periodic distribution of the absorptance. Hence, in the area with higher electron density, the escape of the electrons, silicon atoms, and silicon ions is more possible to take place, causing a stronger ablation. However, if the incident intensity is too high, LIPSS will be suppressed by the ultrafast melting. Our experiments approved this competition compress, as shown in Fig. 12. In the center of the gaussian laser spot, instead of the periodic ripple, there are some volcano-like structures. We believe that it is caused by the shockwave generated when the bubbles burst during the ultrafast melting. As shown in Fig. 11L, the temperature of the lattice can exceed the melting point within several picoseconds, which supports our viewpoint. After irradiation with multi-pulses, the situation is similar, as shown in Fig. 13. Under the high laser fluence, there is still no ripple in the center of the laser spot where can receive more energy, while the ripples appear in the periphery region. When the laser fluence decreases, the LIPSS are formed in the center of the spot. The results indicate that the ultrafast melting, which depends on the laser fluence, plays a critical role in this competing mechanism.

在初期条纹基础上,再结合背景气体对羽流的限域效应引起的再沉积过程,表面形貌的逐渐变化实时地调制着每个脉冲的刻蚀过程,这种反馈机制最终导致了多个脉冲后不同气氛下不同微结构的形成。对于飞秒激光与硅相互作用的物理机制的更深刻了解,有助于我们可控地制备不同微结构的硅材料,改善材料的性质,拓展其应用。在这一基础上,我们分别研究了FLMS在光致发光及拉曼增强方面的应用。

Based on the original ripples and the redeposition of the ejected materials, the surface morphology is various for every successive pulse, leading to the different

ablation processes in different ambient gases. After ablated by multi-pulses, different microstructures are formed by this feedback mechanism. A better understand of the interaction mechanisms can help us to controllably process the material and obtain the desired microstructures. This greatly expands the application area of FLMS. So we try to do some researches on the photoluminescence and the SERS based on FLMS.

在空气环境下制备的 FLMS 具有室温下光致发光 (PL) 的性质, 具有很好的应用前景。我们系统地研究了其发光机制, 并提出载流子迁移模型来解释其非单指数衰减的特性。如图 14 左图所示, FLMS 的光致发光峰位于 530nm, 且不随温度变化, 然而发光强度随温度升高而降低。FLMS 的绿光发光带起源于硅表面形成的表面氧化的硅纳米晶, 氧化层和硅晶核界面上的氧空位缺陷是其发光中心。为了进一步弄清其发光机理及光生载流子在材料内的迁移过程, 我们探究了该光致发光的时间分辨光谱, 如图 14 右图所示。可见, 不同温度下 PL 的衰减不同, 而不同波长的光衰减曲线也不相同, 并且其衰减曲线均不遵循单指数衰减规律。

The FLMS made in air has exhibited a good PL property at room temperature. To further improve its performance, we systematically study the emission mechanism and introduce a new model to describe the carrier transport and explain the decay property of PL. As shown in Fig. 14L, the peak wavelength of PL, which is at 530 nm, does not vary with temperature. However, the PL intensity decreases with temperature. This emission band originates from the silicon nanocrystals (NCs) which are formed during laser ablation and are covered with oxide layers. By time-resolved spectroscopy, we can study the PL mechanism, the carrier transport in the material, and the defect properties. As shown in Fig. 14R, the decay profiles of PL

are various at different temperature and at different wavelength.

FLMS 的 PL 谱的衰减曲线很好地符合拉伸指数 (stretched exponential function) 衰

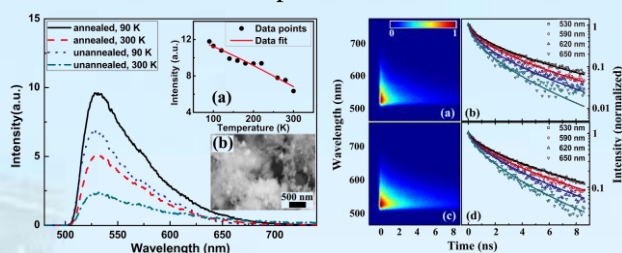


图14. 左图: 退火及未退火FLMS不同温度下的光致发光谱。(a) 退火样品的发光峰强度与温度的关系,(b) 退火样品表面微纳结构的SEM图像。右图: 退火样品不同温度的时间分辨光致发光谱。(a) 300K,(c) 90K;(b)、(d)分别为从(a)、(c)中提取出的不同谱线的衰减曲线。

Fig14. Left: The integral PL spectra of annealed and unannealed FLMS at different temperatures. (a) The temperature dependence of the PL intensity of the annealed sample at peak wavelength. (b) The SEM image of the annealed sample. Right: Time-resolved PL spectra of the annealed sample measured at (a) 300 K and (c) 90 K. The decay profiles at different wavelengths are obtained at (b) 300 K and (d) 90 K. The solid lines are the fits with the stretched exponential function.

减规律: $I = I_0 * \exp[-(t/\tau)^\beta]$, 如图 14 右图 (b)

(d) 所示。我们进一步研究了拟合参数与温度的关系, 如图 15 左图所示。可见, 时间常数 τ 随温度升高而减小。尽管拉伸指数可以很好的拟合实验结果, 但其没有深刻的物理含义, 不能反映真实的物理过程。因此我们提出了载流子迁移模型来阐述载流子的微观运动机制, 并由此解释了 PL 谱的衰减性质。简言之, 光辐照后, FLMS 表面的纳米晶核内产生大量光生载流子, 它们迅速扩散迁移到晶核与氧化层界面, 被氧空位缺陷捕获, 被捕获的载流子会经历一个复杂的弛豫过程: 辐射复合, 再激发, 再捕获, 迁移扩散, 非辐射复合。这些过程相互竞争共同决定了 FLMS 的非单指数衰减的发光性质。根据这一理论, 我们建立了数学模型, 对实验参数进行拟合, 结果符合的非常好, 如图 15 右图所示。对退火和未退火样品的对比, 表明退火降低了非辐射复合中心的密度, 大大减小了非辐射复合速率。载流子迁移模型能够反映 FLMS 这种复杂微纳材料

体系内载流子的输运状态，以及缺陷对载流子输运的影响，对于我们改进 FLMS 具有指导意义。

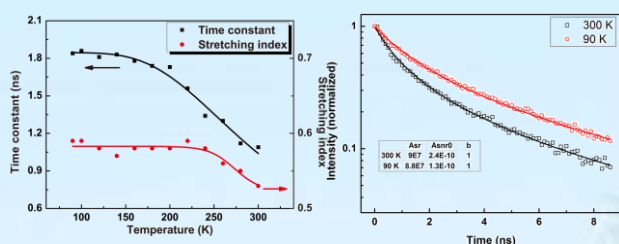


图15. 左图：拉伸指数拟合参数 τ 和 β 与时间的关系。右图：采用载流子迁移模型对300K和90K温度下发射峰强度衰减曲线的拟合结果。

Fig15. Left: Dependences of the time constant τ and the stretching index β on temperature for the wavelength of 530 nm. Right: The decay profiles of the PL (annealed sample) at 530 nm under 300 K and 90 K respectively. The points represent the experimental data and the solid lines denote the fits with our model.

The decay profiles of PL can be well fitted with a stretched exponential function instead of a mono-exponential function. The stretched exponential is described as: $I=I_0*\exp[-(t/\tau)^\beta]$. The dependence of the decay time constant τ and of the stretching index β on the temperature is investigated, as shown in Fig. 15L. It is obvious that τ decreases with the temperature. The stretched exponent is good. However, it does not describe the physical mechanism. So, we introduce a carrier transport model to explain this kind of PL decay. In brief, the carriers, which are excited by incident light in the silicon cores, can quickly transport to the Si/SiO interface and be localized by the oxygen-related defects. These localized carriers will experience a complex process: radiative recombination or to be re-excited. The re-excited carriers may be re-localized or diffuse away, and then non-radiative recombination. This complex process determines the PL properties. According to this theory, we establish a mathematic model to fit the experimental results, as shown in Fig. 15R. The experimental results are perfectly consistent with this model. Comparing the annealed

sample and the unannealed sample, we find that the non-radiative recombination rate decrease greatly due to the decrease of the trap site density. This model helps us to understand the carrier transport and the defect effect in FLMS, and helps us to improve the performance of FLMS.

另外，我们将 FLMS 用于表面拉曼增强基底材料的制作，取得了很好的效果。并且，该方法具有简单、便捷，可大面积制备，FLMS 基底可重复使用等优点。样品制备方法如图 16 左图所示。以 FLMS 为模板，用 PDMS 压印的微纳结构基底材料，展现出很高拉曼增益，如图 16 右图所示。其拉曼增强因子达到 1.98×10^7 。这种高增益一方面源于微米量级微结构的陷光效应，这大大增强了激发光的吸收效率；另一方面，微米量级微结构的表面也很粗糙，有更精细的纳米尺度结构，所以蒸镀金膜后，很自然地形成金纳米结构，且纳米结构的间隙很小，增加了共振增强的“热点”的密度。

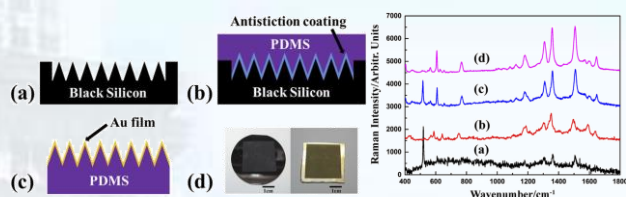


图16. 左图：微结构PDMS拉曼增强基底制备方法示意图及实物。右图：不同基底的拉曼信号，(a) 平整硅片，10-1M R6G，激光功率50mW；(b) 镀金膜的平整PDMS，10-3M R6G，激光功率1mW；(c) 镀金膜的FLMS，10-6M R6G，激光功率0.1mW；(d) 镀金膜的微构造PDMS，10-6M R6G，激光功率0.1mW。积分时间均为10秒。

Fig16. Left: Fabrication of a microstructured polydimethylsiloxane (PDMS) substrate. Right: Raman spectra of rhodamine 6G on different substrates: (a) flat silicon wafer (black) 10- 1M rhodamine 6G (R6G), 50mW laser power; (b) gold film-coated flat polydimethylsiloxane (PDMS) substrate (red), 10- 3M R6G, 1mW laser power; (c) gold film-coated microstructured silicon substrate (blue), 10- 6M R6G, 0.1mW laser power; and (d) gold film-coated microstructured PDMS substrate (purple), 10- 6M R6G, 0.1mW laser power. The integration time is 10 s for all cases.

By using a FLMS as the template, we make a microstructured PDMS substrate for the SERS application. The methods, which are

described in Fig. 16L, have some advantages: simple, low-cost, large area, reusable of the FLMS template. The microstructured PDMS substrate shows a high Raman enhancement, as shown in Fig. 16R. The Raman enhancement factor reaches up to 1.98×10^7 . This can be attributed to two factors. One is the high optical absorptance caused by the microstructures. Another is the nano-structures on the micro-cones which lead to the formation of the gold nanostructures during coating. The gold nano-structures increase the density of the hot spots.

微构造 PDMS 基底不仅有强的拉曼增益, 而且其均匀性非常好, 我们任选了一块 $30 \times 20 \mu\text{m}^2$ 的区域, 探测了其拉曼信号的空间分布, 如图 17 左图所示。其拉曼增强因子的标准偏差仅为 0.13, 具有很好均匀性。另外, FLMS 作为母版, 可以多次使用, 多次压印的微构造 PDMS 的性能十分稳定, 具有可重复性, 第三次压印的样品比第一次压印样品的拉曼信号降低了不超过 15%, 测试结果如图 17 右图所示。这种简单、快捷、低成本且可重复的制备大面积 SERS 基底的方法有望在产业得到应用。

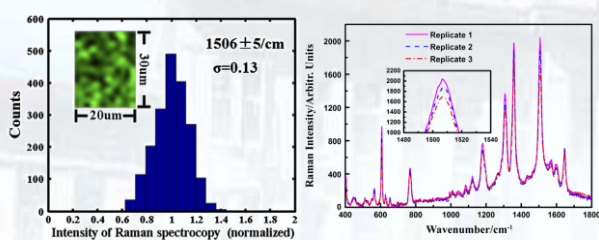


图17. 左图: 微构造PDMS基底上随机选择的一块 $30 \times 20 \mu\text{m}^2$ 区域的 Raman map。右图: 同一块FLMS母版进行3次PDMS压印制备拉曼基底的 可重复性测试。

Fig17. Left: Raman map of microstructured polydimethylsiloxane substrate with an area of $20 \mu\text{m} \times 30 \mu\text{m}$. Right: Raman spectra of rhodamine 6G measured on three different polydimethylsiloxane-based surface-enhanced Raman scattering substrates prepared from the same silicon master copy. Replicates 1–3 were fabricated one by one.

The microstructured PDMS substrate performs a high Raman enhancement. Moreover, it has an excellent uniformity. We randomly map a $30 \times 20 \mu\text{m}$ large area, as

shown in Fig. 17L. The standard deviations of the enhancement factor of microstructured PDMS substrates are $\sigma \sim 0.13$. Besides, we check the reproducibility of the substrates. The results is shown in Fig. 17R. We observe that the Raman intensities of the three replicates vary less than 15%. The microstructured PDMS substrate is promising to be used as SERS substrate in the industry, due to its many advantages.

用飞秒微构造硅材料, 我们制备了光电二极管。这种光电二极管有着极其特殊的性质, 其光电响应是普通硅光电二极管的几百倍。

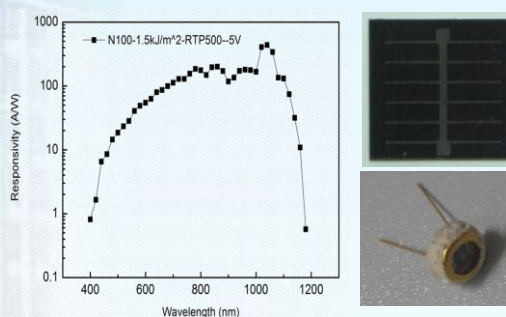


图18. 左图是-5v偏压下的光电响应曲线 (半导体所测量)。

Fig18. The responsivity of FLMS detector, measured by Institute of Semiconductors, Chinese Academy of Sciences.

We made a photoelectronic diode detector using FLMS, which has very special characters. Its responsivity is more than 300 A/W, which is some hundred times than the commercial silicon detector.

基于多光子聚合的激光直写技术作为任意三维微纳加工的关键技术之一, 得到了广泛的发展和应用。此技术基于多光子吸收原理, 多采用脉冲激光器引发单体或者低聚物的聚合反应得到高聚物的产品。此技术的加工分辨率已经达到了 10nm 量级, 与大分子的尺寸很接近。应用于此技术的功能型材料也在不断的探索中。然而, 由材料聚合度不同而导致的光学介面会因倏逝波效应影响光场的分布, 进而影响加工基元的形貌。本文研究了因为倏逝波效应对加工基元的形貌的影响。具体考查了在多脉冲作用下, 材料的折射率改变对加工基元形貌的作用。

发现在微纳尺度上,加工材料聚合后因折射率改变所形成的光学介面将极大影响加工基元的长径比,改变基元的形貌。此结果在一定程度上解释了奇异的加工基元长径比,也为加工材料的选择和开发提供了一定的参考。

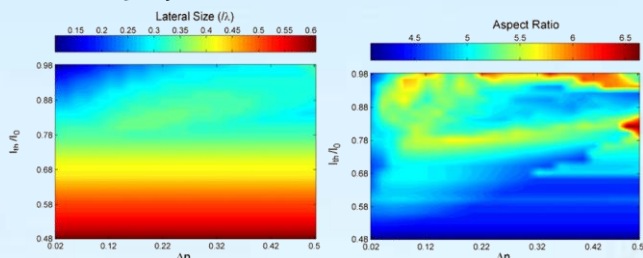


图19. 加工材料不同折射率差及不同域值下,加工基元的尺寸和长径比。
Fig19. The final lateral size (a) and the aspect ratio (b) versus the refractive index change and the polymerization threshold. The lateral size is normalized by the light wavelength in a vacuum.

The relationship between the profile of the structures obtained by multiphoton polymerization and the optical parameters of nanofabrication systems has been studied theoretically for a multipulse scheme. We find that the profile of sub-wavelength structures is greatly affected by the evanescent waves affect. Not only is the photocured polymer voxel affected by the beam profile, but the beam propagation behavior is influenced by the photocured polymer voxel. This gives us a new view of matter–light interactions in multipulse polymerization process, which is useful to the accurate control of the nanofabrication profile and the selection of new nanofabrication materials.

SiC 由于其独特的性质(莫氏硬度为9与 Al_2O_3 相似;努氏硬度为 2480 kg/mm^2 , 略高于 Al_2O_3 的 2100 kg/mm^2), 作为第三代半导体材料正广泛应用于 MEMS 器件的。然而其加工技术是限制其应用,尤其是高集成器件应用的一个瓶颈。我们用基于激光直写的飞秒直写技术,实现了超衍射极限的微纳结构的加工。此方法为 SiC 在 MEMS 器件方面的应用提供了良好的前景,并为基于 SiC 的石墨烯构形生长技术提供了前期的准备。

Sub-diffraction-limit fabrication of 6H-SiC is investigated with femtosecond laser direct-write setup. Micro/nano-fabrication on 6H-SiC is studied with a home-made micro/nano-fabrication platform, which is

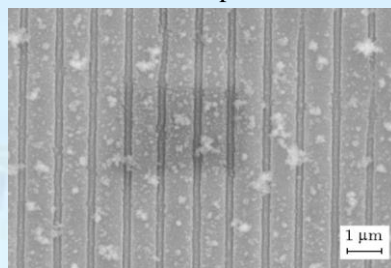


图20. 周期1 微米线宽240 纳米的SiC线阵列结构。

Fig20. SEM of a 240 nm line on SiC with 1 μm period. integrated with a fluorescence microscope and a Ti:sapphire laser with a central wavelength of 800 nm and pulse duration of 130 fs. Micro/nano-structures are characterized with scanning electron microscope. It is found that the spatial resolution is improved with the decrease of laser power and the increase of scanning velocity. The smallest resolution achieved is 125 nm and line array with a line width of 240 nm and a period of 1 μm is fabricated. This work paves the new way for integrated micro electro-mechanical systems devices.

表面等离子激元可实现光在纳米尺度上传播和操作的控制,被认为是下一代芯片尺寸元件的传输媒介。表面等离子激元作为金属-介质表面传播电子与电磁场的耦合,它的激发、传播、信号处理已经得到广泛的研究。在光信息存储、传播和处理中,很多应用需要光具有很高的相干性,因此在光-表面等离子激元-光转换中,光的相干性的保持成为值得研究的问题。在本文中我们搭建了一个由棱镜、银膜、空气和铌酸锂组成的四层介质光学系统。先是以两束光入射激发表面等离子激元,在铌酸锂中表面等离子激元被解耦合成光并记录下一个全息光栅。这表明两束光在通过在光-表面等离子激元-光转换中保持相干。通过研究该全息光栅的性质,我们发现全息光栅的厚度在百微米的尺度上。全息光栅的厚度表明光栅确实是

解耦合的光记录而不是直接由表面等离子激元写入。

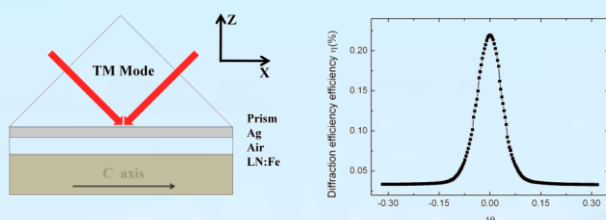


图21. (a) 四层光学系统的示意图; (b) 全息光栅的衍射效率随读出光角度的变化 (横坐标原点为布拉格角)。

Fig21. (a) Experimental setup with a four-layer system,

Layer 0: a K9 glass prism; Layer 1: an Ag film; Layer 2: an air layer; Layer 3: an LN:Fe crystal.

(b) Rocking curve of the photorefractive holographic grating. The origin of the $\Delta\theta$ is at the Bragg angle.

We constructed a four-layer system composed of a prism, a silver film, an air layer and a lithium niobate crystal. Initially we used two coherent light beams to excite surface plasmons. The surface plasmons were then decoupled into light in the photorefractive crystal where a holographic grating was recorded. The two beams remained coherent through light to surface plasmons to light transformation. Studying the characteristics of the holographic grating we found out that the thickness of the grating was to the order of hundreds of microns. The thick holographic grating suggests that the holographic recording in the photorefractive materials was induced by the leaky waves rather than by surface plasmon polaritons directly.

我们首次在实验上产生了 three-Airy beams。这种新型光束可以通过三个艾里函数相乘得到。我们的实验结果表明: 相对传统的二维艾里光来说, three-Airy beams 不需要衰减截断就可以实现。另外, 我们还研究了它在光折变晶体中的非线性传输情况。我们发现, 在线性传输时, 这种光束会衍射成超高斯光束。但是在自散焦非线性下, 却转变成三个强光斑传输。当然, 在自聚焦非线性下, 它可以稳定的自陷传播。这些实验结果可以应用于光束整形及相关光学设计。

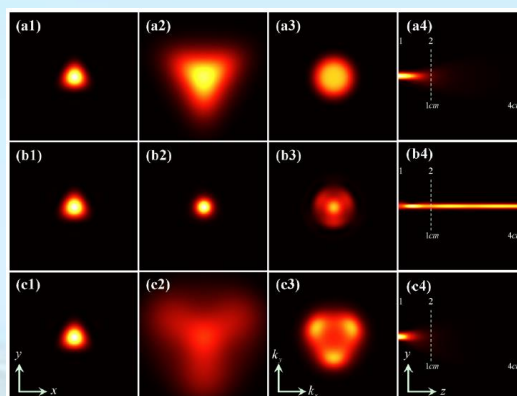


图22. Three-Airy beam在SBN晶体中非线性传输1cm的数值模拟结果: (a) 线性, (b) 自聚焦非线性, (c) 自散焦非线性。(a1-c1) 和 (a2-c2) 分别对应输入和输出的光场分布。(a3-c3) 对应于 (a2-c2) 的空间频谱分布。(a4-c4) 是4cm非线性传输的侧视图。

Fig22. (Numerical simulation) The (a1)-(c1) input, (a2)-(c2) output intensity patterns of the three-Airy beam transmitting through 1 cm SBN when (a) no nonlinearity, (b) self-focusing nonlinearity, or (c) self-defocusing nonlinearity is present. (a3)-(c3) k-space spectrum corresponding to the second column. (a4)-(c4) Side view of 4 cm propagation through the SBN crystal.

We report the first experimental demonstration of the so-called three-Airy beam. Such beams represent a two-dimensional field that is a product (rather than superposition) of three Airy beams. Our experiments show that, in contrast to conventional Airy beams, this new family of Airy beams can be realized even without the use of truncation by finite apertures. We study linear and nonlinear propagation of the three-Airy beam in a photorefractive medium. It is found that a three-Airy beam linearly diffracts into a super-Gaussian-like beam, while under nonlinear propagation it either breaks up with a self-defocusing nonlinearity or evolves into a self-trapped channel with a self-focusing nonlinearity. Our results may find applications in beam shaping and related optical design.

之前的大部分对自加速光轨迹调控的研究都是在实空间 (坐标空间), 我们提出了一种新的方法在频谱空间实现对自加速光轨迹的调控。我们引入空间频谱相位梯度的

概念来产生和调控单轨迹和多轨迹的自加速光束，并且理论和实验上成功的实现了对自加速光轨迹的调控。自加速光的轨迹实际上可以看成是由很多不同的关键空间频率通过频谱空间到实空间的映射变换形成的。在非傍轴条件下，我们的结果清楚的显示了艾里光束的解体，同时展示了圆形、椭圆及双曲加速光也可以通过调节频谱相位得到。进一步我们发现通过频谱调控预定轨迹的加速光同样可以适用于矢量光波。我们所提出的通过傅立叶频谱空间新方法为调控自加速光的轨迹提供了更多的可能性，而有些轨迹的调控是无法在实空间实现的。

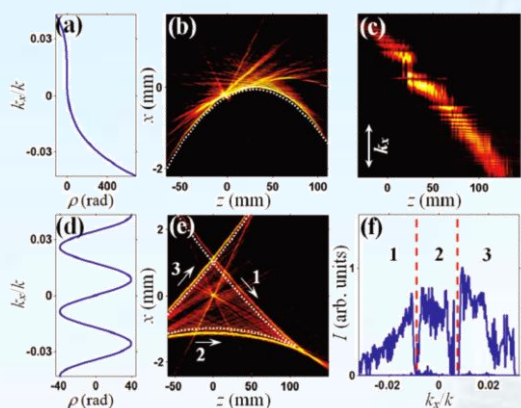


图23. 利用立方相位（第一行）(a) 与正弦相位（第二行）(d) 来产生自加速光的实验结果图。频谱的相位分布：(b),(e)分别为(a)与(d)形成单轨迹与三轨迹的加速光，(c)为(b)中只剩下主极大的频谱；(f)为(e)中对应不同轨迹的频谱区域。

Fig23. Experimental results of self-accelerating beams obtained with a cubic (top panels) and a sinusoidal (bottom panels) phase. Spectral phase distribution: (b), (e) single and triple trajectories of the accelerating beams resulting from (a) and (d), respectively; (c) theresidual spectrum of the filtered main hump in (b); (f) different spectral ranges responsible for different trajectories in (e).

We introduce the concept of spatial spectral phase gradient, and demonstrate, both theoretically and experimentally, how this concept could be employed for generating single- and multipath self-accelerating beams. In particular, we show that the trajectories of the accelerating beams are determined a priori by different key spatial frequencies through direct spectrum-to-distance mapping. In the nonparaxial regime, our results clearly

illustrate the breakup of Airy beams from a different perspective, and demonstrate how circular, elliptic, or hyperbolic accelerating beams can be created by judiciously engineering the spectral phase. Furthermore, we found that the accelerating beams still follow the predicted trajectory also for vectorial wave fronts. Our approach not only generalizes the idea of Fourier-space beam engineering along arbitrary convex trajectories, but also offers possibilities for beam or pulse manipulation not achievable through standard direct real-space approaches or by way of time-domain phase modulation.

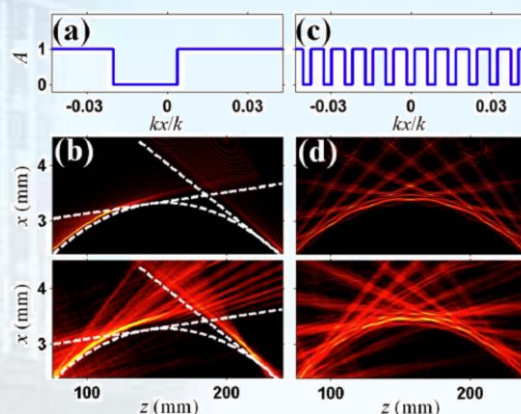


图24. 通过单个频谱阱 (a)与周期性频谱阱(b)产生沿抛物线轨迹传播的周期性加速光。(a),(c)是对应产生(b)与(d)加速光的k空间频谱的强度调制，第一行第二行分别为对应的数值模拟结果与实验结果。

Fig24. Generation of periodic accelerating beams along a parabolic curve by employing (a), (b) one spectral well and (c), (d) an array of spectral wells. (a), (c) k-space amplitude modulation relative to the results in (b) and (d), where the upper and bottom panels correspond to numerical and experimental results, respectively.

我们进一步提出并实现了一种通过在傅立叶空间同时改变相位与振幅的方法来产生周期性自加速光，对小幅度变化，加速光束仍然遵循平凸轨迹，它可以仅通过作用于频谱的相位来实现，但是对于大调制比如具有亥维赛函数生成的具有零振幅分布的频谱会修正平凸的轨迹，因为它会形成一些直线的轨迹。此外，沿着凸轨迹传播的周期性加速光可以通过周期性的频谱阱来实现，这

种方法对傍轴与非傍轴都适用。

We propose and demonstrate the generation of periodic self-accelerating beams through both phase and amplitude modulation in the Fourier space. For small amplitude variations, an accelerating beam still follows a smooth convex trajectory, which can be traced by acting on the spectral phase only. However, large modulations such as those generated from the Heaviside function with a zero amplitude distribution partially modify the convex trajectory due to the appearance of straight-line paths. Furthermore, periodic self-accelerating beams along convex trajectories are realized by employing an array of “spectral wells” in both the paraxial and nonparaxial regimes.

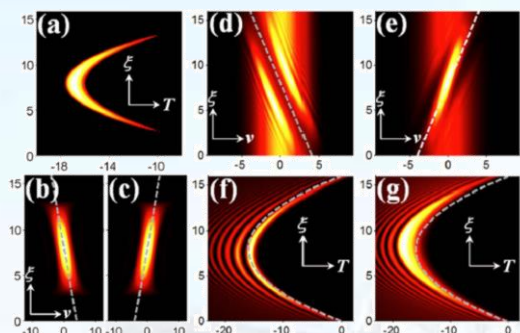


图25. 线性与非线性传播的艾里型脉冲。(a)主峰值的线性演化, (b)和(c)为脉冲在反常色散(b)和正常色散(c)的频谱成分, (d)和(e)为反常色散(d)和正常色散(e)的频谱分布, (f)与(g)对应(d)和(e)的非线性时域演化情形。所有图中虚线表示的是线性传播的轨迹。

Fig25. Linear and nonlinear propagation of Airy pulses. (a) Evolution of the main hump in the linear case, (b) and (c) spectral components of the pulse depicted in panel for anomalous (b) and normal (c) dispersion, (d) and (e) spectral distribution for anomalous (d) and normal (e) dispersion, (f) and (g) nonlinear temporal evolution corresponding to (d) and (e), respectively. Here, the dashed lines show the linear trajectories.

我们理论与实验研究了艾里型脉冲在光纤中基于自相位调制的非线性传输现象。在非线性的演化过程中,艾里型脉冲频谱的能量在正常色散区间会集中于一个峰值,在反常色散区间会集中在两个峰值。在传播过程中该峰值的位置会移动,这样就形成了纵坐

标与频谱空间的一个映射关系。这个频率的移动可以通过简单的附加一个频谱的立方相位结构来精确的控制而不需要改变光纤的长度。

We theoretically and experimentally study the phenomena related to self-phase modulation of Airy pulses in fibers. During nonlinear evolution, most spectral components of the Airy pulses concentrate into one or two peaks for normal and anomalous dispersion, respectively. The resulting peaks self-shift along the propagation, effectively mapping the longitudinal coordinate into the frequency domain. The frequency shift can be precisely controlled by simply acting on the spectral cubic phase structure without the need to alter the fiber length.

我们理论研究了二维四方光子晶格中高能类四极光束的非线性传播特性。发现在适当的自聚焦非线性下,单格点入射的类四极光束可以形成稳定的传播常数位于第二布拉格反射带中的带隙孤子,同时发现如果改变入射四极光束与晶格对称轴的角度,非线性四极模式会形成周期性振荡的局域模式,更为重要的是在振荡过程中在某些特定的传播距离上会形成具有轨道角动量的二阶涡旋模式。我们对形成的涡旋模式进行了讨论,发现它可以看成是由第三布洛赫带中不同对称点布洛赫模式叠加而成。

Higher-band self-trapping and oscillation (rotation) of nonlinear quadruple beams in two-dimensional (2D) square photonic lattices are numerically demonstrated. Under appropriate conditions of nonlinearity, aquadruple-like beam can self-trap into localized modes that reside in the second Bragg reflection gap through single-site excitation. By changing the initial orientation of the incident quadruple beam related to the lattices, periodic oscillations of the localized quadruple mode may be obtained. The localized quadruple state becomes a rotating doubly charged optical vortex (DCV) during

rotation and should undergo charge-flipping when the rotating direction is reversed.

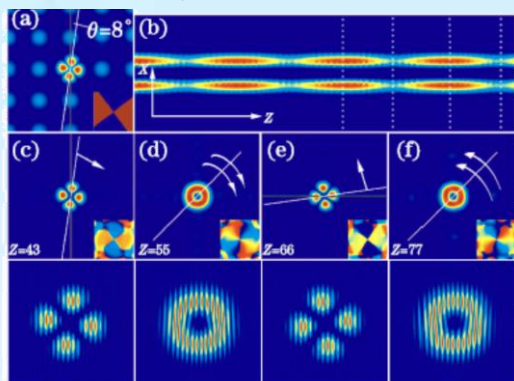


图26. 四方光子晶格中非线性高带四极模式演化成二阶涡旋模式的数值模拟结果。

Fig26. Numerical results of the generation of doubly charged vortices during the propagation of a nonlinear quadruple-like beam in high band of 2D square photonic lattices.

石墨烯是一种由单层碳原子组成的二维材料，具有多种优异的性能和新奇的特性，因此成为了凝聚态物理及材料学领域研究的前沿和热点。石墨烯中电子的传输行为与无质量狄拉克费米子的行为类似，产生了一系列新颖的物理现象。石墨烯中电子边缘态对于理解这些现象及相关的电子传输性质具有至关重要的作用。但是石墨烯的边缘由于杂质，缺陷，及化学键不稳定性等因素影响，使得直接在石墨烯中观察电子的边缘态非常困难，特别是对于类胡须型的边缘 (bearded edge)，因为它在石墨烯中不能稳定存在。我们制备了一种与石墨烯对称性完全相同的光学微结构---光子石墨烯 (photonic graphene)。这种微结构具有与石墨烯相似的能带结构和狄拉克点，这使得我们利用光学手段来研究石墨烯中的物理机制成为可能。更为重要的是光子石墨烯能够提供稳定的，完美的边缘来研究其边缘态及其特性。从而在实验上成功的直接观察到了存在于锯齿形和类胡须型边界上的边缘态，并且测量了它们的色散特性。更为重要的是，还发现了一种从未预言过的存在于类胡须型边界上的新型边缘态，这种新型的边缘态存在于带边的范·霍夫奇异点附近，它可以分类归属于类塔姆态。与传统的塔姆态的物理机制不同，该边缘界面上是完美无缺陷的。我们发

现的这种新型的边缘态也可能存在于其它具有类似带隙结构的晶格系统中。该工作不仅提供了一种直接研究石墨烯相关物理现象的光学平台，更为重要的是对于理解石墨烯中电子边缘态及相关的电子输运性质具有至关重要的作用。

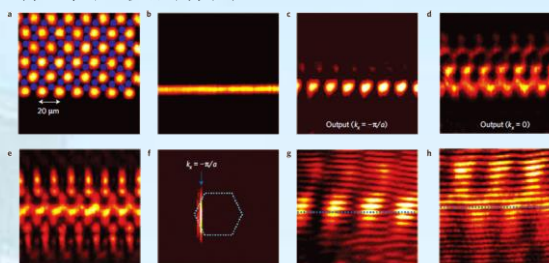


图27. 光诱导光子石墨烯中观察到锯齿型边缘态的实验结果图。(a)晶格诱导光与对应的在自散焦非线性下形成的光子石墨烯晶格的格点(蓝色点),(b)激发边缘态的条形探测光,(c)当探测光以倾斜角度 $k_x = -\pi/a$ 入射到锯齿型边界面时的出射光强分布,(d)当入射光无倾斜($k_x=0$)入射时表面的出射光强分布,(e)在晶格内部的线性出射,(f)对应(b)的入射光的空间频谱,(g),(h)分别对应(c),(d)与倾斜平面波沿着边界方向的干涉图。

Fig27. Experimental demonstration of an edge state at the zigzag edge of an optically induced honeycomb lattice. (a), Lattice-inducing beam (bright spots) and corresponding lattice sites (blue spots) induced under self-defocusing photorefractive nonlinearity. (b), Transverse pattern of an input probe beam launched along the bottom edge in (a). (c) Localized output when the input beam is tilted at $k_x = -\pi/a$. (d), Diffracted output when the input beam is not tilted ($k_x = 0$). (e), Diffracted output when the input beam is launched straight into the bulk. f, Fourier spectrum of the input beam corresponding to c, g, h, Interferograms of output (c, d) with a tilted broad beam showing the staggered phase (g) and the uniform phase (h) of the output field along the edge.

Graphene, a two-dimensional honeycomb lattice of carbon atoms, has been attracting much interest in recent years. Electrons therein behave as massless relativistic particles, giving rise to strikingly unconventional phenomena. Graphene edge states are essential for understanding the electronic properties of this material. However, the coarse or impure nature of the graphene edges hampers the ability to directly probe the edge states. Perhaps the best example is given by the edge states on the bearded edge that

have never been observed—because such an edge is unstable in graphene. Here, we use the optical equivalent of graphene—a photonic honeycomb lattice—to study the edge states and their properties. We directly image the edge states on both the zigzag and bearded edges of this photonic graphene, measure their dispersion properties, and most importantly, find a new type of edge state: one residing on the bearded edge that has never been predicted or observed. This edge state lies near the Van Hove singularity in the edge band structure and can be classified as a Tamm-like state lacking any surface defect. The mechanism underlying its formation may counter intuitively appear in other crystalline systems.

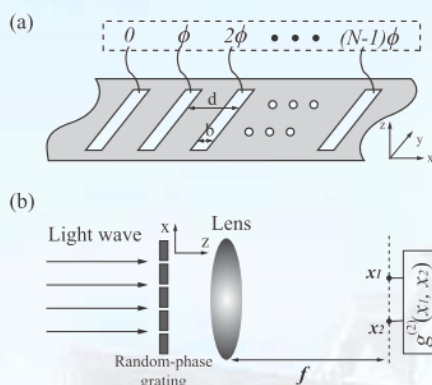


图28. (a) 设计的N周期随机相位光栅及其相位结构。其中 ϕ 为随机相位。(b) 基于随机相位光栅的远场双光子干涉效应的原理图，其中 f 为透镜焦距。

Fig28. (a) Schematic diagram for the designed random-phase grating with N slits. The inset shows the random phases encoded on the light waves transmitting through the respective slits of the grating, in which the elementary phase ϕ changes with time randomly. (b) Schematic diagram for detecting the two-photon interference of the light wave transmitting through the N-slit random-phase grating in the Fraunhofer zone, where f is the focal length of the lens.

通过相位控制，我们设计了一种随机相位光栅，从而引入了双光子多路径干涉，并进一步在理论和实验上观察到了可见度超过50%的经典光的双光子干涉效应。这一结果表明相位控制对光学高阶干涉具有很重要的调控作用。

Two-photon interference with

independent classical sources, in which superposition of two indistinguishable two-photon paths plays a key role, is of limited visibility with a maximum value of 50%. By using a random-phase grating to modulate the wavefront of a coherent light, we introduce superposition of multiple indistinguishable two-photon paths, which enhances the two-photon interference effect with a signature of visibility exceeding 50%. The result shows the importance of phase control in the control of high-order coherence of classical light.

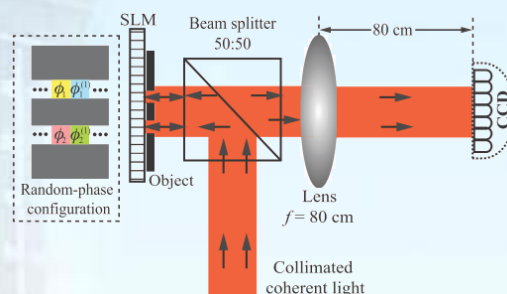


图29. 实验方案的示意图，左侧的虚线框内是双缝模板上加载的随机相位示意图。

Fig29. Diagram of the experimental setup. The inset on the left side shows the spatial configuration of the random-phase pairs on the slits of the mask.

我们设计了一种具有双光子路径纠缠性质的经典光源，该光源的每一个发光点源具有两个模式，其中每个模式的相位随时间变化具有随机性，但满足两个模式的相位之和为一个常数，即两个模式的相位是反关联的。由这种光源可以引进具有路径纠缠性质的双光子路径，从而实现经典光的二阶亚波长干涉。实验上，我们采用纯相位型空间光调制器调制通过双缝的激光的位相结构，使得从双缝出射的光具有上述性质，从而实现了双缝的二阶亚波长干涉。

We propose a two-photon subwavelength interference scheme for classical light in which multiple quantum-like entangled two-photon paths play an essential role. These entangled two-photon paths are introduced through a specially designed source composed of many point sources j with j 's complex

amplitude being a superposition of modes with certain relationship in their phases. Interference between the entangled two-photon paths could lead to second-order subwavelength interference of an object put in front of the source plane. In a proof-of-principle experiment, by using a spatial light modulator to modulate the wave front of a coherent light, we have generated such a source and observed subwavelength interference of a double-slit mask via two-photon measurement.

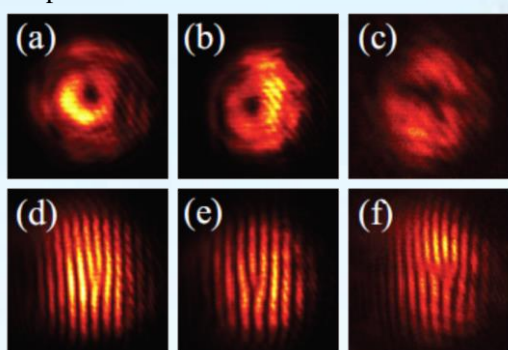


图30. $\text{Pr}^{3+}:\text{Y}_2\text{SiO}_5$ 晶体中基于 EIT 效应光脉冲存储的光学拓扑电荷的相加实验结果。其中第一行为光强分布情况，第二行为与平面波干涉形成的叉型干涉图。(a)和(b)分别为两输入光束的光强分布，(d)和(e)分别为对应的叉型干涉图。(c)和(f)为光学拓扑电荷相加后的对应结果。

Fig30. Summation of optical topological charges through optical pulse storage-retrieval process on the basis of EIT effect in $\text{Pr}^{3+}:\text{Y}_2\text{SiO}_5$ crystal. Here the first and the second rows are the transverse intensity profiles and the fork-type interference fringes of interacting beams. (a) and (b) are the transverse intensity profiles of two input beams, while (d) and (e) are the corresponding fork-type interference fringes. (c) and (f) are the transverse intensity profile and the fork-type interference fringes of the output targeted beam.

在 $\text{Pr}^{3+}:\text{Y}_2\text{SiO}_5$ 晶体中，我们验证了基于 EIT 的光脉冲存储-读取过程中相互作用光束所携带的光学拓扑荷守恒。根据该守恒定律，我们可以将相互作用光束所携带的光学拓扑荷转移到目标信号光上，并在光脉冲的存储和读取过程中实现了光学拓扑电荷的加减等代数运算。上述结果在经典和量子信息处理方面有潜在的应用价值。

We verified that optical topological

charges are conserved in a two-step light-pulse storage and retrieval process based on the electromagnetically-induced-transparency (EIT) effect in a $\text{Pr}^{3+}:\text{Y}_2\text{SiO}_5$ crystal. Based on this conservation law, one could transfer topological charges from the interacting beams, which may not be overlapped in space and time domains, to the targeted output signal beam, and algebraic operations such as summation and subtraction of topological charges carried by the interacting beams were demonstrated via the EIT-assisted two-step light-pulse storage-retrieval process. The results may be useful for classical and quantum information processing based on optical topological charge buffer memory in EIT media.

基于两个声光调制器之间包层模的倏逝波耦合，我们设计了可调谐且插入损耗在可调波段内均一的话路转换器。转换器的调谐范围从 1490 纳米到 1610 纳米，覆盖了全部的 C 波段 L 波段以及部分的 S 波段，插入损耗在调谐过程中始终保持在 -5dB 左右。这种结构可以广范应用于可调宽带耦合器及粗波分复用系统。

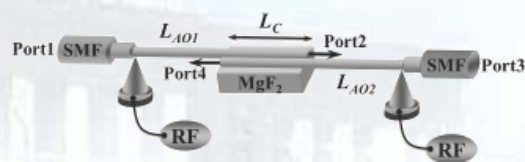


图 31. 均一插入损耗的双声光可调谐耦合器结构示意图。

Fig31. The configuration of the acousto-optic add/drop tunable coupler with uniform insertion loss.

Based on the evanescent-field coupling between the cladding modes of two adjacent and parallel all-fiber acousto-optic tunable filters, tunable broadband light coupling with relatively uniform insertion loss of trapping spectrum was achieved. In the experiments, a wide spectral tuning range from 1490 nm to 1610 nm, covering the whole C- and L-band and parts of S-bands, was demonstrated with a wavelength tunability slope of -0.72 nm/kHz .

The insertion loss of the trapping spectrum was uniform (around -5.0 dB, which can be improved with a longer evanescent-field coupling length) within the whole tuning spectral range. Such a light coupling structure would be useful in tunable broadband light coupler and broadband optical fiber add/drop multiplexer for applications in coarse wavelength division multiplexing systems.

光致荧光是研究物质能级结构的重要传统技术,但如果荧光物质对发射的光谱有一定的吸收,甚至出现二次发射,将会影响荧光的光谱线形和发光强度,从而影响研究者对于物质本征能级结构等的分析与判定。尽管这种自吸收和再发射效应很早就被人发现,但对于特定实验系统中两种效应的具体影响很少有人认真量化。本文针对实验室的激发-发射直角配置的通用荧光光谱系统,建立了激发和发射光在样品空间传输过程中能量转移微分模型,通过数值模拟分析了荧光物质的本征性质(吸收、发射光谱和量子效率等)和外在实验条件(激发位置、样品浓度和探测效率等)对最终探测到的荧光发射光谱的影响,并用不同浓度的若丹明 6G 标准样品进行了实验验证。模拟和实验结果都印证了自吸收和再发射效应将会强烈的影响到荧光发射光谱,表明对发光和吸收具有较大重叠的荧光物质,必须用低浓度试样才能获取本征光谱信息。

A theoretical approach based on differential radiative transport is proposed to quantitatively analyze the self-absorption and reemission effects on the emission spectrum for right angle excitation-detection photoluminescence measurements, and the wavelength dependence of the reemission effect is taken into account. Simulations and experiments are performed using rhodamine 6G solutions in ethanol as model samples. It is shown that the self-absorption effect is the dominant effect on the detected spectrum by inducing pseudo red-shift and reducing total

intensity; whereas the reemission effect partly compensates for signal decrease and also results in an apparent signal gain at the wavelengths without absorption. Both effects decrease with the decrease in the sample concentration and the propagation distance of the emission light inside the sample. We therefore suggest that diluted solutions are required for accurate photoluminescence spectrum measurements and photoluminescence-based measurements.

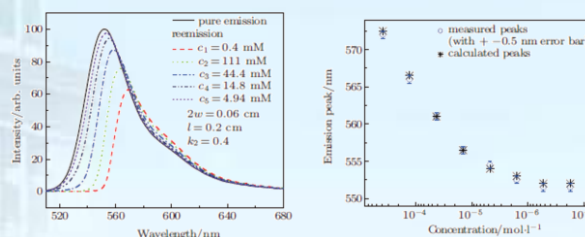


图 32. (a) 考虑到再发射效应时样品浓度对若丹明 6G 溶液荧光发射谱影响的模拟结果。(b) 实验和理论计算的不同浓度的若丹明 6G 溶液的表现光谱红移。

Fig32. (a) Simulation of the influence of sample concentration on emission spectrum considering reemission effect in Rh6G solution. (b) Artificial spectral red-shifts of Rh6G solution with different concentrations.

小胶质细胞存在于脑和脊髓中,是中枢神经系统的第一道也是最主要的一道免疫防线。当脑部受到创伤或感染时,小胶质细胞可迅速动员并聚集,在正常细胞和受损细胞间形成一个保护屏障。BV-2 小胶质细胞系是反转录病毒感染原代培养的小鼠小胶质细胞而获得的永生细胞系,基本具备了原代培养的小胶质细胞的形态学、表型以及各项功能特点。在多细胞体系下,我们实验观察到 BV-2 小胶质细胞存在频率混乱的自发钙振荡。互相关分析表明发生自发钙振荡的小胶质细胞之间具有一定关联性,即存在胞间通讯。基于最小钙模型,我们理论分析发现胞间通讯可引起自发钙振荡频率混乱。快速荧光成像结果显示 BV-2 小胶质细胞自发钙振荡的每一个钙波的起始区域以及传播方向均不同,说明小胶质细胞受到来自于不同方向的信号影响,即小胶质细胞与周围几个不同的细胞之间存在胞间通讯(图 33)。

综上，正是由于小胶质细胞与周围若干个细胞同时存在通讯效应，且小胶质细胞存在自发整体钙升高现象，导致实时测量出来的自发钙振荡的频率是混乱的。本工作可为小胶质细胞相关免疫类疾病研究提供了更新的思考视角及实验支持。

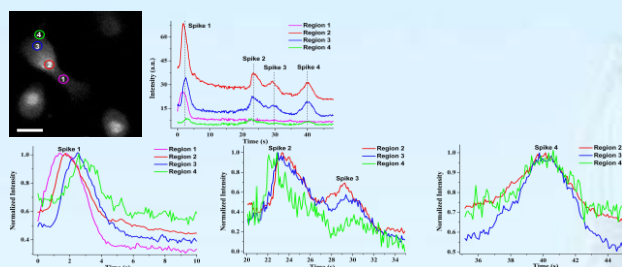


图 33. 基于快速荧光成像的单个 BV-2 小胶质细胞内钙信号时空变化监测。

Fig33. Fast imaging of Ca^{2+} oscillations in a single BV-2 microglial cell. A Ca^{2+} wave was triggered in region 1 for the first spike (C), in region 4 for the second spike (D) and region 2 for the third spike (D), respectively. A synchronous global Ca^{2+} elevation was observed for the fourth spike (E).

As the first and main form of active immune defense in the central nervous system, microglial cells usually show complicated intracellular calcium (Ca^{2+}) activity that can mediate the downstream components of signaling cascades. It was suggested that microglial cells could rapidly congregate together and establish a potential barrier between the healthy and damaged tissue after the brain injury. BV-2 microglial cells were widely used as a microglial model because they can mimic various microglial responses. In this study, we observed spontaneous oscillations of the cytosolic calcium concentration ($[\text{Ca}^{2+}]_c$) in multi-BV-2 microglial cells. These cells exhibited random spikes of Ca^{2+} oscillations. Cross-correlation analysis of the temporal dependence of the oscillations proposed the existence of cell-cell communication mediated by extracellular messengers. Numerical simulations based on a simple mathematical model suggested that

these communications could induce random spikes of spontaneous Ca^{2+} oscillations in the multi-cell system. Fast fluorescence imaging analysis of random spikes in different regions of a single cell found that spontaneous Ca^{2+} oscillations resulted from Ca^{2+} wave generated by other cells as well as from calcium elevation inside the cell (Fig. 33). Taken together, we clearly observed that spontaneous Ca^{2+} oscillations in the form of random spikes took place in the multi-BV-2 microglial cell system *in vitro*. We demonstrated that cell-cell communication existed between the cells, which then induced random spikes of spontaneous Ca^{2+} oscillations.

关节炎可诱发骨骼形成、吸收失衡等疾病如骨质疏松，严重影响患者正常的生命活动。这些疾病的产生与关节处滑膜细胞代谢异常关系密切。多种炎症因子可刺激病变关节分泌产生大量一氧化氮(Nitric oxide, NO)。研究表明 NO 在炎症导致的骨质疏松过程起着重要作用，其可抑制滑膜细胞生长并刺激细胞凋亡。本工作基于荧光成像技术监测胞内重要第二信使钙的变化，体外研究大剂量外源性 NO 供体硝普钠 (donor sodium nitroprusside, SNP) 对大鼠关节炎模型的滑膜细胞钙信号转导动力学过程的影响。我们实验发现 1 mM 浓度的 SNP 避开传统的环鸟苷酸途径，转而通过新颖的亚硝基化修饰方式诱导胞外钙涌入，进而引起滑膜细胞胞内钙浓度升高。进一步研究表明瞬时感受器电位离子通道蛋白 V 亚家族 1 (transient receptor potential vanilloid subtype 1, TRPV1) 抑制剂辣椒平 (capsazepine)、钌红 (ruthenium red)、镧 (La^{3+}) 可分别抑制 SNP 导致的钙涌入，而电压敏感性钙通道拮抗剂尼非地平 (nifedipine) 对 SNP 导致的钙涌入几乎没有抑制效果 (图 34)。此外，SNP 还可明显诱发滑膜细胞凋亡，而上述 TRPV1 通道抑制剂可一定程度上降低 SNP 导致的细胞凋亡。综上，我们实验证明大剂量外源性 NO 供体 SNP 可通过亚硝基化修饰方式激活 TRPV1 通道，并引起胞外钙内流，进

而导致胞内钙升高，最终导致滑膜细胞凋亡。本工作可为探讨滑膜细胞在炎症导致的骨质疏松等疾病中的生理病理作用提供一定的实验参考和新的思考视角。

Inflammation-mediated osteoporosis is the result of an inflammation-induced imbalance of bone formation and resorption orchestrated by osteoblasts. The high-level production of nitric oxide (NO) induced by inflammatory cytokines has been shown to play a key role in the pathogenesis of inflammation-mediated osteoporosis. The aim of this study was to investigate the role of the signaling transduction of NO donor sodium nitroprusside (SNP) in modulating the cytosolic calcium concentration ($[Ca^{2+}]_c$) of osteoblasts. In this work, we found that 1 mM SNP caused an increase of the cytosolic calcium concentration ($[Ca^{2+}]_c$) in osteoblasts, which was completely inhibited by applying Ca^{2+} -free buffer (Fig. 34). Furthermore, it showed that the SNP-induced $[Ca^{2+}]_c$ increase was obviously inhibited by useful antagonists of the transient receptor potential vanilloid subtype 1 (TRPV1) channel: capsazepine, ruthenium red, and La^{3+} in Ca^{2+} -containing buffer, respectively. However, nifedipine, an L-type voltage sensitive Ca^{2+} -channel blocker, failed to suppress this $[Ca^{2+}]_c$ change. Additionally, 1 mM SNP induced osteoblast apoptosis, which could be largely abolished by the blockers of TRPV1, capsazepine and ruthenium red. Interestingly, we found that the SNP-induced $[Ca^{2+}]_c$ increase was evidently inhibited by N-ethylmaleimide, the blocker of S-nitrosylation modification, instead of inhibitors of the NO-cGMP-PKG pathway. In conclusion, our data clearly indicated that the NO donor SNP resulted in apoptosis associated with TRPV1 channel-mediated Ca^{2+} entry via S-nitrosylation in osteoblasts.

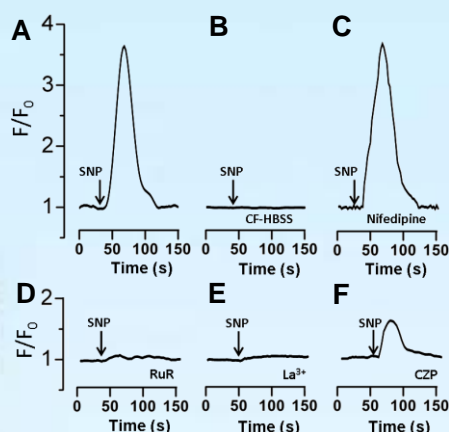


图34. 外源性一氧化氮通过激活TRPV1通道引起胞外钙涌入进而导致胞内钙升高。

Fig34. SNP triggered Ca^{2+} entry through TRPV1 channel in osteoblasts. (A) A representative trace of the $[Ca^{2+}]_c$ response to a 1mM SNP stimulus. The inhibitory effects of Ca^{2+} free-HBSS (B), 20 μ M nifedipine (C), 10 μ M RuR (D), 100 μ M La^{3+} (E), and 10 μ M CZP (F) on $[Ca^{2+}]_c$ increase induced by SNP (1mM).

光谱表征及传感技术/Spectral Characterization and Sensing Techniques

负责人：宋峰

本方向涉及制备稀土发光材料，研究稀土材料发光的机理及其应用，以及应用光谱学和光谱仪器等方面；此外还研究了超衍射光斑以提高显微镜的分辨本领。取得的代表性成果如下：

In this field, we mainly focused on the preparation of rare earth luminescent materials, the research of their mechanisms of luminescence and their applications, applied spectroscopy and spectral instrument. Besides, we also investigate the shaper super-diffraction spot which can improve dramatically resolution of microscope. Some representative results are as follows:

我们证实了在 Er^{3+} 、 Yb^{3+} 共掺的 $\text{Y}_2\text{Ti}_2\text{O}_7$ 薄膜中加入银、金纳米粒子后，薄膜的发光得到了增强。随着银三角纳米粒子的沉积，观察到了更强的 525nm、546nm 和 659nm 的上转换发光以及强烈的近红外增强发光。

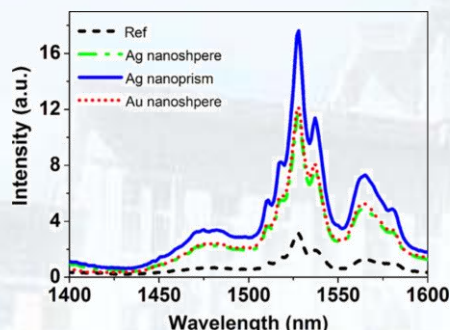


图1. 在 975nm 激光激发下，加入银纳米球（绿色虚线）、银纳米三角（蓝色实线）和金纳米球（红色点线）的 $\text{Er}^{3+}/\text{Yb}^{3+}$ 共掺 $\text{Y}_2\text{Ti}_2\text{O}_7$ 薄膜的近红外发射光谱。

Fig1. NIR photoluminescence spectra of $\text{Er}^{3+}/\text{Yb}^{3+}$ co-doped $\text{Y}_2\text{Ti}_2\text{O}_7$ films spin coated with Ag nanospheres (0.2 mm/l) (green dash dot line), Ag nanoprisms (0.2 mm/l) (blue solid line), Au nanospheres (0.2 mm/l) (red short dot line) solution, upon 975 nm LD excitation.

The enhanced luminescence of $\text{Er}^{3+}/\text{Yb}^{3+}$ co-doped $\text{Y}_2\text{Ti}_2\text{O}_7$ films were demonstrated when silver/gold (Ag/Au) nanoparticles (NPs) were doped in the films. With the precipitation of the Ag nanoprisms, more intense green (525 nm, 546 nm), red (659 nm) upconversion

(UC) emission bands and strong enhanced near infrared (NIR) emission were observed and the enhanced factors were up to 16.7, 15.6, 17.7 and 5.6 folds, respectively.

我们研究了准静态近似下，向列相液晶包覆的球形金属纳米颗粒的远场和近场特性。通过调节金属纳米核的材料、向列相液晶的各向异性以及壳层的厚度来实现共振峰的调节。发现沿着入射光的偏振方向，在外层球壳表面附近得到了场增强。

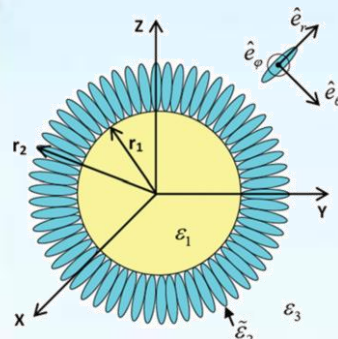


图2. 半径为 r_2 的向列相液晶金属纳米球，由半径为 r_1 的金属核和厚度为 $R=r_2-r_1$ 的向列液晶层组成；入射光为沿 Z 向传播的 X 方向偏振光。
Fig2. A NLC-coated nanosphere of total radius r_2 consists of a metal core of radius r_1 and a NLC shell of thickness $R = r_2 - r_1$ and the incident light is along the Z-direction, and is X-polarized.

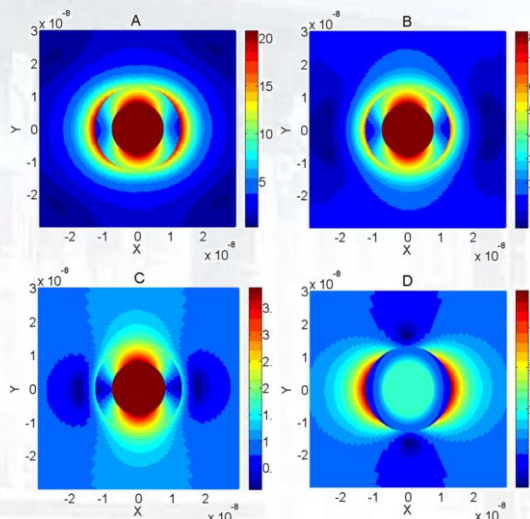


图3. 向列相液晶包覆的银纳米球 X-Y 平面上的场增强 $|E/E_0|$ 强度图。
Fig3. Contour plots of the electric field enhancement $|E/E_0|$ in the X-Y plane for the BYL4012 NLC-coated Ag nanosphere, $\Delta \epsilon = 19.8$, $R = 5$ nm. Other parameters are (A) $\lambda_{\text{resonance}} = 517$ nm, (B) $\lambda = 476$ nm, (C) $\lambda = 413$ nm, (D) $\lambda = 688$ nm.

The far-field and near-field properties of a spherical nematic liquid crystal (NLC) coated metal nanoparticle (NPs) have been investigated in an external field, basing on the quasistatic theory. The resonant wavelength is tunable by varying metallic material of core, anisotropy extent and thickness of liquid crystals (LCs). The field enhancement is along the incident polarization near the outer surface of the shell.

通过高温熔融方法制备 $\text{Sb}^{3+}/\text{Mn}^{2+}$ 共掺的磷酸盐玻璃，我们测试了它的吸收、激发和发射光谱。结果发现该玻璃在可见光区域高度通透，在紫外区域有强的吸收。在 275nm、360nm、415nm 和 520nm 激发下，它都能发射出强的红光。该玻璃材料在玻璃大棚上将有广泛的应用前景。

$\text{Sb}^{3+}/\text{Mn}^{2+}$ co-doped phosphate glasses were prepared by high temperature melting method. The absorption, excitation, and emission spectra of the glasses were investigated. The glasses are transparent in the visible light region and can emit strong red light under 275, 360, 415, or 520nm excitation. The materials will be helpful in developing glass greenhouse for the green plants.

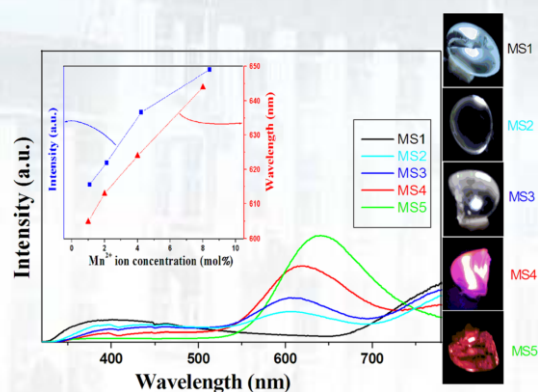


图 4. 在 275nm 激发下，五种玻璃样品的发射光谱；插图为 520nm 激发下 MS3 样品的发射强度和发射波长与 Mn^{2+} 浓度的关系。

Fig4. Emission spectra of the MS1, MS2, MS3, MS4, and MS5 glass samples under 275 nm excitation; the inset is the dependence of the emission intensity, and wavelength of the MS3 sample on the Mn^{2+} ion concentration under 520nm excitation.

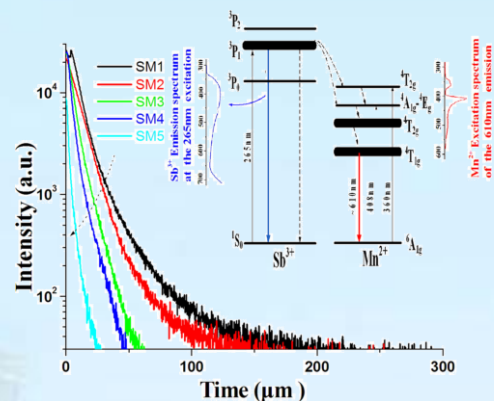


图 5. 在 275nm 激发下五种样品的 415nm 荧光衰减曲线；插图为 Sb^{3+} 和 Mn^{2+} 的能级图及其能量传递示意图。

Fig5. Decay curves of the 415nm emission of the glass samples under 275 nm excitation; the inset is the energy level diagram of the Sb^{3+} and Mn^{2+} ions, as well as the proposed energy transition.

我们研究了半径为 12nm 的银纳米球和半径为 20nm 的金纳米球对稀土配合物 $\text{Eu}(\text{TTFA})_3$ 发光的影响。在 350nm 激发下，银纳米颗粒掺杂的 Eu 配合物发光增强为 2.5 倍。通过准静态近似法，我们计算模拟了在平面波垂直照射下，银纳米球的电场分布。

The influence of 12 nm spherical silver nanoparticles (AgNPs) and 20 nm spherical gold nanoparticles (AuNPs) on the luminescence of europium complex $\text{Eu}(\text{TTFA})_3$ were studied. When 350 nm is chosen as the incident light, the maximum enhancement factor of the complexes mixed with AgNPs is about 2.5 at the wavelength of 612 nm. By means of the quasi-static approximation theory, the distribution of the electric field around a single spherical metallic nanoparticle illuminated by plane wave was calculated.

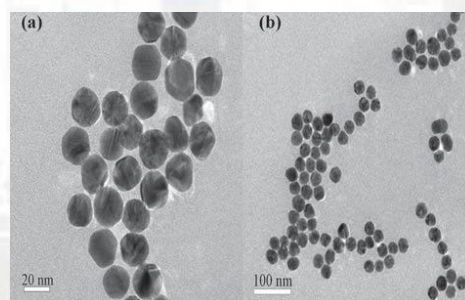


图 6. 半径为 12nm (a) 和半径为 20nm 的银纳米粒子的 TEM 图。
Fig6. The TEM images of AgNPs with a radius of about 12 nm (a) and AuNPs with a radius of about 20 nm (b).

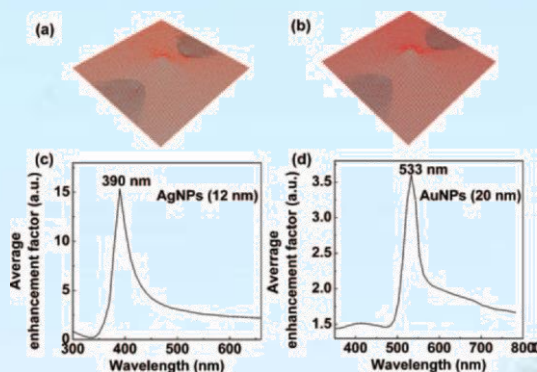


图 7. (a) 和 (b) 分别为银纳米球和金纳米球的电场分布模拟图; (c) 和 (d) 分别为银纳米球和金纳米球的平均增强因子随入射光波长的变化情况。

Fig.7. (a) and (b), simulation results of the electric field distribution for spherical silver and gold nanoparticles respectively. (c) and (d), the average enhancement factor varies with the wavelength of the incident light for spherical silver and gold nanoparticles respectively.

我们合成了 $Tm^{3+} / Tb^{3+} / Eu^{3+}$ 三掺的白光磷酸盐玻璃。在 365nm 激发下, Eu0.07 玻璃样品的 CIE 坐标 ($x=0.339, y=0.341$) 接近于标准的白光, 并且其量子效率很高, 达到了 72.27%。根据荧光寿命的分析, 我们合理解释了 Tm^{3+} 到 Eu^{3+} 的能量传递过程。为了增强白光发射, 我们还制备了 $Tm^{3+} / Tb^{3+} / Eu^{3+}$ 三掺的磷酸盐玻璃陶瓷。

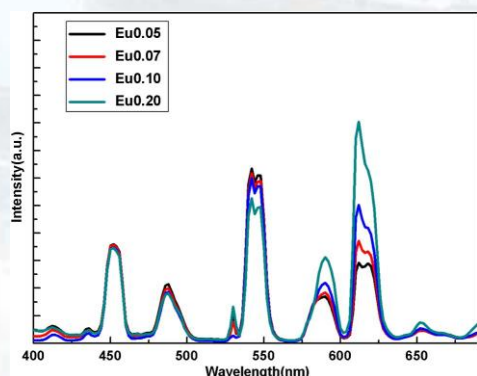


图 8. 在 365nm 激发下 Eu0.05, Eu0.07, Eu0.10 和 Eu0.20 玻璃样品的发射谱。

Fig.8. Emission spectra of the Eu0.05, Eu0.07, Eu0.10, and Eu0.20 glass samples under 365 nm excitation.

$Tm^{3+} / Tb^{3+} / Eu^{3+}$ tri-doped phosphate glasses are synthesized to explore new white-light-emitting materials. Under 365 nm excitation, the CIE coordinates ($x=0.339, y=0.341$) of the Eu0.07 glass sample are close

to the standard equal energy white-light illumination ($x=0.333, y=0.333$). The quantum efficiency is very high ($\sim 72.27\%$). The energy transition from Tb^{3+} to Eu^{3+} is reasonably interpreted based on the analysis of the luminescence lifetimes. To enhance the white-light emission, $Tm^{3+} / Tb^{3+} / Eu^{3+}$ tri-doped phosphate glass ceramics are prepared.

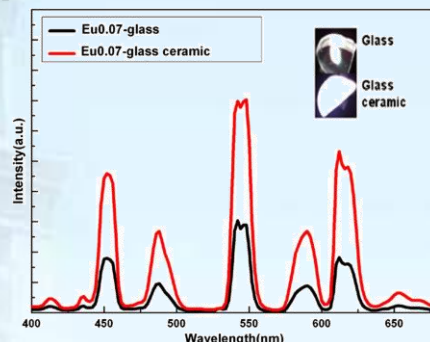


图 9. 在 365nm 激发下, $Tm^{3+} / Tb^{3+} / Eu^{3+}$ 三掺的磷酸盐玻璃和玻璃陶瓷的发射光谱, 插图分别为玻璃和玻璃陶瓷的照片。

Fig.9. Emission spectra of the $Tm^{3+} / Tb^{3+} / Eu^{3+}$ tri-doped phosphate glass and glass ceramic under 365 nm excitation. The inset shows the photos of the glass and glass ceramic.

我们探究了在高数值孔径 $NA=1$ 的情况下, 基模以及高阶模式的拉盖尔-高斯径向偏振光 4π 聚焦形成的焦场, 计算了各种情形下焦斑的峰值半高宽。与相同条件下的单透镜高数值孔径的情形相对比, 生成了在横向和纵向尺寸都被大幅度缩小的锐利焦斑。这样尺寸上的压缩不仅来源于特定方向上的高阶径向偏振光的纵向焦场分量的干涉相消, 而且还得益于两个相向传播的入射光的径向焦场分量的完美干涉相消。

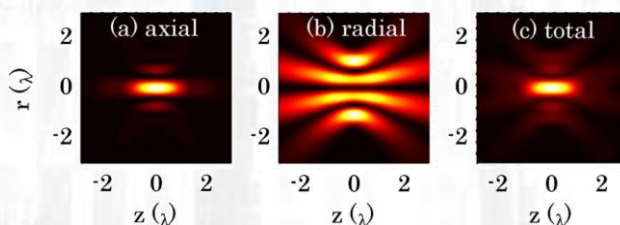


图 10. 在单透镜数值孔径 $NA=1$ 的紧聚焦情况下, 高价径向偏振光 ($R-TEM_{11}^*$) 的 (a) 轴向分量 (b) 径向分量和 (c) 总场的在 $r-z$ 面上的强度分布图。

Fig.10. Calculated intensity distributions of the (a) axial component, (b) the radial component, and (c) and the total in $r-z$ plane under single-lens tight focusing with $NA=1$ for the higher-order LG RP ($R-TEM_{11}^*$) beam.

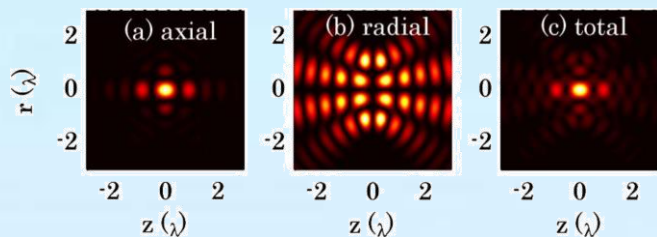


图 11. 在数值孔径 $NA=1$ 的 4π 紧聚焦情况下, 高径向偏振光 ($R-TEM_{11}^*$) 的 (a) 轴向分量 (b) 径向分量和 (c) 总场的在 $r-z$ 面上的强度分布图。

Fig11. Calculated intensity distributions of (a) the axial component, (b) the radial component, and (c) the total in the $r-z$ plane under the 4π tight focusing with $NA=1$ for the higher order LG RP ($R-TEM_{11}^*$) beam.

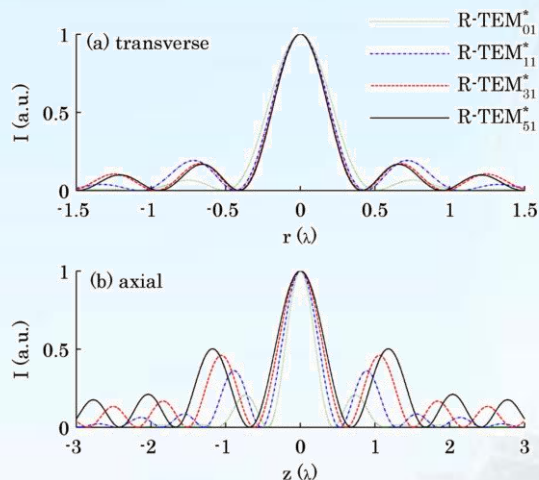


图 12. 在数值孔径 $NA=1$ 的 4π 紧聚焦情况下, $R-TEM_{01}^*$ (点线)、 $R-TEM_{11}^*$ (虚线点线)、 $R-TEM_{31}^*$ (虚线) 和 $R-TEM_{51}^*$ (实线) 光场在 (a) 焦面上 (b) 沿光轴方向的归一化强度曲线。

Fig12. Calculated intensity profiles in (a) the focal plane and (b) along the optical axis for the $R-TEM_{01}^*$ (dotted curve), $R-TEM_{11}^*$ (dashed-dotted curve), $R-TEM_{31}^*$ (dashed curve), and $R-TEM_{51}^*$ (solid curve) beams under the 4π tight focusing with $NA=1$. The peak intensity for each mode is normalized to 1.

The focal electric fields for a 4π high numerical aperture (NA) focusing system with both the doughnut and higher order Laguerre-Gaussian (LG) radially polarized (RP) beams are investigated in the case of $NA=1$, and the full width at half-maximum values of the focal spots are calculated. Compared with the single-lens high NA focusing configuration, a sharper spot, whose size is reduced efficiently in the transverse as well as the axial direction, can be formed. Such size reduction is attributed to not only the destruction

interference of the longitudinal component caused by the π phase shift between any two adjacent rings of the incident higher-order LG RP beam coming from one particular direction but also the perfect destruction interference of the radial component formed by the two counter-propagating incident beams.

通过 Eu^{3+} 离子作为荧光探针研究了镧系元素掺杂的 $\beta-PbF_2$ 纳米颗粒。三价稀土离子以取代 Pb^{2+} 格位的方式掺入纳米晶中, 并且发现稀土掺杂浓度可以诱导稀土离子位置对称性从 O_h 到 D_{4h} 的畸变。通过荧光和 X 射线衍射分析, 低浓度稀土离子掺杂的纳米颗粒具有 Pb_3EuF_9 立方相结构, 其点群和空间群分别是 O_h ($m-3m$) 和 $Pm-3m$ (NO. 221)。然而随着掺杂浓度的增加, Pb_3EuF_9 立方相结构逐渐转变为具有点群和空间群分别为 D_{4h} ($4/mmm$) 和 $P4/mmm$ (NO. 123) 的 $PbEuF_5$ 四方相结构。特别是在中等浓度掺杂的时候我们第一次提出并证实了两种混合结构的存在。另外, 根据第一性原理中结合能的计算, 四方相结构的结合能比立方相结构的结合能低 $2.327eV$, 这意味着在高浓度掺杂的时候四方相结构比立方相结构更加的稳定, 更易形成。这个工作让我们更加全面深入的理解了镧系元素在氟化物纳米晶中的位置对称性以及它们在氟化物纳米晶中所处的晶格场环境。这对进一步稀土离子光学特性的研究, 比如结构对稀土离子发光的调控等, 有着重要的指导意义。

在以上工作的基础上制备了一系列不同稀土离子掺杂的玻璃陶瓷, 通过热处理获得了一系列不同稀土离子掺杂的纳米颗粒, 通过 XRD 对其结果进行了分析, 结果表明对于不同稀土离子的掺杂, 以上的结论同样适用。针对不同的稀土离子, 其半径与结构存在一定的约束关系。

By using Eu^{3+} as a fluorescence probe in Lanthanide-doped $\beta-PbF_2$ nano-particles, Ln^{3+} ions are substituted for Pb^{2+} sites and the doping concentration induces a site symmetry distortion from O_h to D_{4h} . By photoluminescence and XRD study, we

conclude that the structure of lowly doped nano-particles is cubic Pb_3EuF_9 (O_h ($m-3m$), $Pm-3m$ (NO. 221)). With the increase of doping concentration, the cubic Pb_3EuF_9 transforms to tetragonal PbEuF_5 (D_{4h} ($4/mmm$), $P4/mmm$ (NO. 123)). Particularly, the coexistence of both structures in moderately doped nano-particles is proposed and confirmed for the first time. The binding energy of the C and T structures differs with about 2.327 eV, which means that the T structure is more stable and easier to form in highly doped materials. Our work represents a significant advance towards a more comprehensive understanding of the site symmetry of Ln^{3+} ions in fluoride nano-particles, which would benefit the further research on the optical properties, such as fluorescence regulation and control of Ln^{3+} ions, and have great importance in the applications of this material in optical fields.

A series of rare earth (RE) doped oxyfluoride glasses with the composition of $(45-x) \text{SiO}_2-5\text{Al}_2\text{O}_3-40\text{PbF}_2-10\text{CdF}_2-x\text{RE}_2\text{O}_3$ ($x = 1, 5, 10, 15$) (mol%) were prepared by a traditional melt-quenching method. Glass ceramics (GCs) were obtained after thermal treatment and characterized by X-ray diffraction (XRD) to investigate the nanocrystal structure and distortion. Based on the RE-doping mechanism of Pb^{2+} - RE^{3+} substitution with interstitial F^- charge compensation, different phases can form via adjusting the dopant concentration. The cubic Pb_3REF_9 phase with $Pm3m$ space group plays a dominant part in low dopant concentration. The unit cell parameters decrease from 5.92 Å to 5.80 Å from Pr to Yb. Tetragonal PbREF_5 phases with $P4/mmm$ (No. 123) space group appear with increasing dopant concentration, and RE^{3+} has a typical D_{4h} ($4/mmm$) point symmetry. The “peak splitting” in the XRD spectra was found in GC doped with RE^{3+} ,

and the splitting distance gets smaller and smaller as the RE^{3+} ionic radius increases from Yb^{3+} to Dy^{3+} . This phenomenon was well explained by the structural distortion due to the difference in ionic radius between the host ion and the guest ion. Our work provides a comprehensive understanding towards nanocrystal structure at the atomic level and the RE^{3+} environment in oxyfluoride glass ceramics, which would benefit further optical investigations and practical applications.

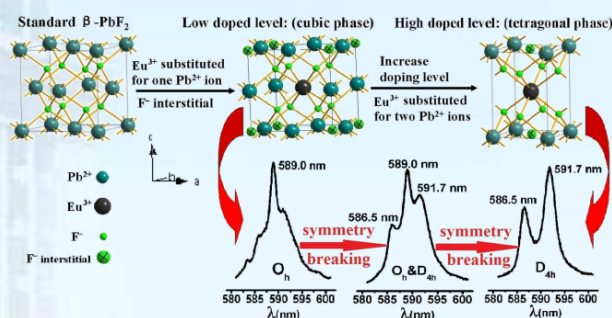


图 13. 不同 Eu 离子掺杂导致结构从 Pb_3EuF_9 到 PbEuF_5 的对称破缺示意图。

Fig13. Photoluminescence spectroscopy employing Eu^{3+} as the structural probe unambiguously revealed a doping concentration induced phase transition from lowly doped cubic Pb_3EuF_9 to highly doped tetragonal PbEuF_5 .

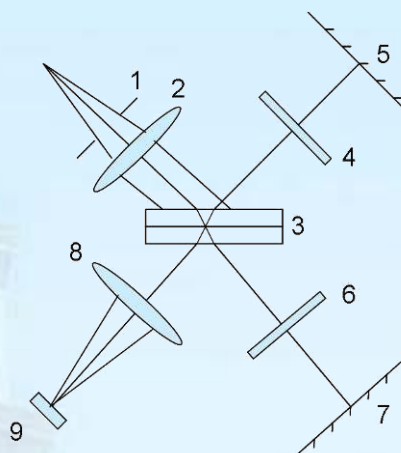
完成一种转动扫描式傅里叶变换光谱仪的专利申请工作, 该光谱仪具有如下特点: 转动装置位于光路的一臂, 光程补偿装置位于光路的另一臂, 不需为转动装置提供额外的空间开销, 可以使光谱仪体积缩小到半个手掌的大小。此外, 光谱仪通过旋转角的改变可以实现很细微的光程差改变, 通过最大旋转角、转动装置折射率等参数的设置可以实现光程差从纳米量级至毫米或厘米量级的改变。这种光谱仪最大特点为体积小, 重量轻, 扫描范围广, 实用性高, 是一种能够实现实时在线测量的便携式光谱仪。

完成一种 CCD 波长校准方法的专利申请工作, 该方法具有如下特点: 其目的是求得波长在多项式展开下能够满足给定误差要求时的最合理的展开项个数或拟合参数个数。其方法是将拟合参数个数作为变量, 利用已知的标准数据和给定的误差要求以

最小二乘的方式求得拟合方程,用说明书中所述的判定方式对拟合数据进行判定,最终找到最合适的拟合参数个数。该方法的主要优势在于对于波长拟合而言,不再是主观的默认一个展开项个数进行数据拟合,而是依靠给定的误差要求,找到最合适的展开项个数,这样既能保证误差精度,又不至于因为展开项过多而增大运算量,所以这是一种既精确又有效的波长校准方法。

Our invention is Micro-turbo Fourier Transform Spectrometer (MTFTS), a kind of Fourier transform spectrometer which achieves the changing of optical path difference by rotary scanning. The schematic is Fig 1. Component 1 is an aperture to control the diameter of incident light, which can be set according to the actual situation; Component 2 is a lens to generate parallel light; Component 3 is a beamsplitter which can separate a beam into two; Component 4 is the rotating device, driven by servo motor, which achieves the changing of optical path difference by rotary scanning. The material of component 4 can be chosen as for NIR. Component 5 and 7 are mirrors. If the angle between the beamsplitter and the incident beam is 45 degree, the incident beam will be on the way back to the original. Component 6 is the compensation device of optical path to compensate the optical path difference when the rotation angle of rotating device is zero. Its material is the same with rotating device. Component 8 is a lens and component is the detector. MTFTS has the advantage of small size, good stability and wide spectral range. With appropriate devices, it can be made as small as the palm of your hand. Optical path difference can increase from micrometer to millimeter with the rotation angle increasing and per 0.1 degree changing of rotation angle can cause the micrometer-order changing of optical path difference. For the rotating device, optical path difference will not be affected even

though it shifts along the direction perpendicular or parallel to the normal and is the same as compensation device.



This is a method of CCD wavelength calibration. The data collected by CCD is a series of coordinates which one coordinate is spectral signal intensity and the other one is pixel coordinate. When incident light is incident on the grating, the diffraction light is detected by CCD so wavelength is a function of pixel coordinate. According to the infinite series expansion, the function can be written as:

$$\lambda(x) = a_0 + a_1x + \Lambda + a_s x^s + \Lambda$$

It should be truncated as polynomial in practical applications and its coefficients can be determined according to the principle of least squares:

$$\lambda(x) = a_0 + a_1x + \Lambda + a_{l-1}x^{l-1}$$

Suppose n sets of data of standard wavelength λ_i and pixel x_i coordinate is given:

$$\begin{aligned} &(x_1, \lambda_1) \\ &\dots \\ &(x_n, \lambda_n) \end{aligned}$$

Our method is to provide a way to find a reasonable truncated number of polynomial with known data in a given error. Specific methods are as follows: Suppose the given error is Λ (for example, $\Lambda = 0.5 nm$), the number of fitting parameters is $N (N \leq n)$, X is the maximum of pixel coordinate.

- (1) Make $N = 2$ and it is linear fit.
- (2) In case of the number of parameters is N , we can get the fit coefficients a_0, Λ, a_{N-1} , so the fit function is:

$$\lambda^*(x) = a_0 + a_1x + \Lambda \Lambda + a_{N-1}x^{N-1}$$

(3) Put the coordinates x_1, x_2, \dots, x_n into the fit function in (2) and we can get the fit wavelength $\lambda_1^*, \lambda_2^*, \dots, \lambda_n^*$. Calculate the deviation with the standard wavelength.

(4) Consider the following two aspects:

- ① $|\lambda_i - \lambda_i^*| \leq \Lambda \quad \forall i = 1, 2, \dots, n$
- ② $\lambda'(x)$, derivative of $\lambda^*(x)$, is greater than zero in $[0, X]$. It is to maintain monotonically of $\lambda^*(x)$.

If two aspects above are true, N is the number of fit parameters which meet the requirement of the given error. So the wavelength fit function is:

$$\lambda(x) = a_0 + a_1x + \Lambda \Lambda + a_{N-1}x^{N-1}$$

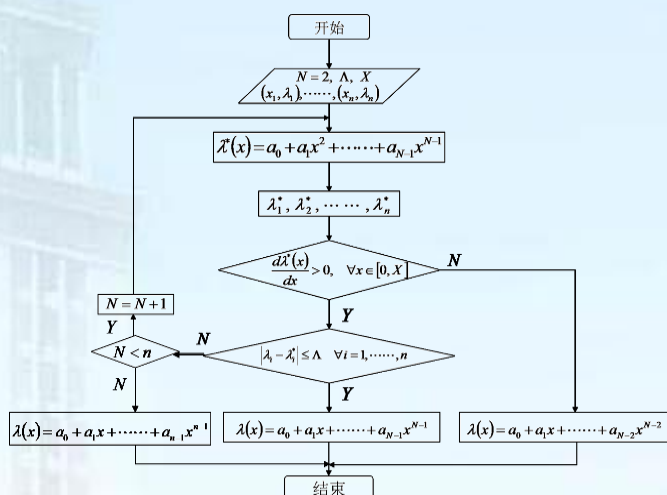
If ② is true but ① is false, if $N < n$, make $N = N + 1$ and repeat the step (2), (3), (4); If $N = n$, we consider the best fit function is:

$$\lambda(x) = a_0 + a_1x + \Lambda \Lambda + a_{n-1}x^{n-1}$$

As long as ② is false, we consider that there is no appropriate fit function under this given error, so we make:

$$\lambda(x) = a_0 + a_1x + \Lambda \Lambda + a_{N-2}x^{N-2}$$

Flow chart is shown below:



光场调控及其应用/Manipulation of Optical Fields and Its Application

负责人: 王慧田

本方向主要开展连续光和飞秒脉冲矢量光场和光学涡旋等新型光场的调控生成、焦场工程、非线性光学效应、微加工和微操纵等方向的研究。取得的代表性成果如下:

In this field, we mainly focused on the generation of the new optical fields such as vector fields and optical vortex by continuous wave and femtosecond pulse; the focusing engineering, the nonlinear effect, the micro manipulation and fabrication by the new optical fields. This year, we obtained some respective results as following.

随着矢量光场各种应用的提出,更加丰富的矢量光场的提出就有了必要性。我们成功地设计并生成了几种非柱对称的多偏振奇点矢量光场,包括具有类电磁场力线偏振分布的局域线偏振矢量光场、具有双极对称性的局域偏振矢量光场等。

As a series of applications of vector fields are presented, it is necessary to enrich the family of vector fields. We have successfully designed and generated several kinds of vector fields with several polarization singularities and without cylindrical symmetry. These vector fields include vector fields with polarization distributions similar to electric and magnetic field lines, vector fields with bipolar symmetry of linear polarization and so on.

我们利用已提出的矢量光场生成方案,设计并生成了具有类似于电磁场力线偏振分布的局域线偏振矢量光场,如图1所示。利用可用于控制矢量光场的附加自由度,新的焦场及其相关特性被发掘了出来。图2是类磁场线偏振分布的局域线偏振矢量光场的几种紧聚焦场强度分布的示意图。

With the method for the generation of vector fields presented before, we design and generate vector fields with polarization

distributions similar to electric and magnetic field lines, as shown in Fig. 1. With the help of new degree of freedom to control the vector fields, new kinds of tight focusing fields and their features are found. Fig. 2 shows the intensity patterns of tight focusing fields of vector fields with polarization distributions similar to magnetic field lines.

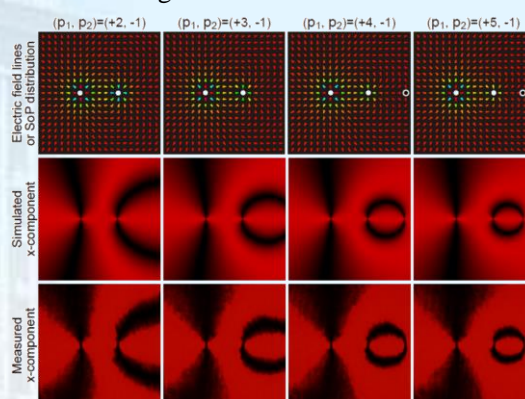


图1. 类双电荷电场力线偏振态分布的局域线偏振矢量光场。

Fig1. Vector optical fields with polarization distributions similar to electric field lines of two electric charges.

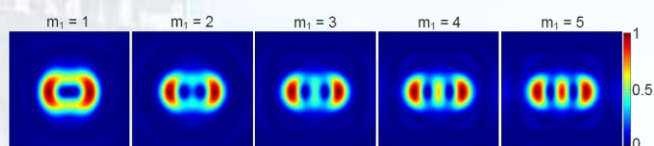


图2. 类磁场力线偏振分布的矢量光场的紧聚焦场强度分布图。

Fig2. Intensity distributions of the tightly focused vector optical fields with polarization distributions similar to magnetic field lines.

同时,我们还设计和生成了一类具有双极对称性的局域线偏振矢量光场,其打破了常见矢量光场的圆和椭圆对称性,如图3所示。这种矢量光场具有较高的灵活性和新颖的紧聚焦性质。通过调控偏振态分布,我们获得了具有较高品质因子的条状焦斑,其x和y方向的强度分布如图4所示。

Meanwhile, we design and generate a kind of vector optical fields with bipolar symmetry of linear polarization, which breaks the cylindrical and elliptic cylindrical

symmetry of most vector fields, as shown in Fig. 3. There is more flexibility for this kind of vector fields, and new tight focusing properties are found. We have also got a tight focusing pattern of a sharp line with high figure of merit through adjusting the distribution of polarization, and the intensity patterns of the focusing fields in x and y directions are shown in Fig. 4.

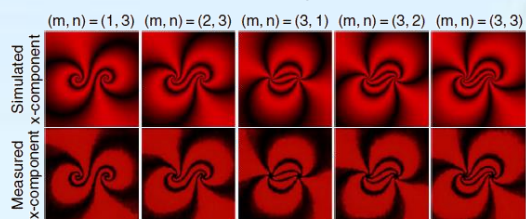


图3. 偏振态具有双极对称性的局域线偏振矢量光场。
Fig3. Vector optical fields with bipolar symmetry of linear polarization

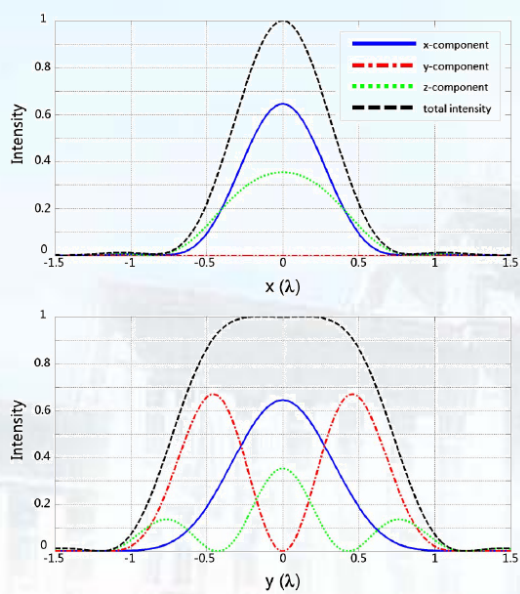


图4. 一种双极矢量光场的条状焦斑的 x 和 y 方向强度分布。
Fig4. Intensity profiles of a sharp line formed by a kind of tightly focused vector field with the bipolar symmetry of linear polarization.

发表论文/Publications in Journal

1. X.-D. Chen, Z.-B. Liu, W.-S. Jiang, X.-Q. Yan, F. Xing, P. Wang, Y. Chen, and J.-G. Tian, "The selective transfer of patterned graphene," *Scientific Reports* 3, 03216 (2013).*
2. K. Lou, S. X. Qian, Z. C. Ren, C. H. Tu, Y. N. Li, and H. T. Wang, "Femtosecond laser processing by using patterned vector optical fields", *Scientific Reports* 3, 02281 (2013).
3. M.C. Rechtsman, Y. Plotnik, J.M. Zeuner, D. Song, Z. Chen, A. Szameit and M. Segev, Topological Creation and Destruction of Edge States in Photonic Graphene, *Phys. Rev. Lett.* 111, 103901(2013)
4. Hua Cheng , Shuqi Chen, Ping Yu , Jianxiong Li, Boyang Xie, Zhancheng Li, and Jianguo Tian, "Dynamically tunable broadband mid-infrared cross polarization converter based on graphene metamaterial," *Appl. Phys. Lett.* **103**, 223102 (2013).
5. F. Xing, X.-D. Chen, Z.-B. Liu, Q. Zhang, X.-Q. Yan, Y. Chen, and J.-G. Tian, "Transparent and flexible multi-layer films with graphene recording layers for optical data storage," *Appl. Phys. Lett.* 102, 253501 (2013).
6. Z.-L. Li, W.-Y. Zhou, Y.-G. Liu, Q. Ye, Y. Ma, H.-F. Wei, and J.-G. Tian, "Highly efficient fluorescence detection using a simplified hollow core microstructured optical fiber", *Appl. Phys. Lett.* 102, 011136 (2013)
7. P. Wang, Z.-B. Liu, X.-D. Chen, F. Xing, W.-S. Jiang, B. Dong, W. Xin, and J.-G. Tian, "Accurate layers determination of graphene on transparent substrate based on polarization-sensitive absorption effect," *Appl. Phys. Lett.* 103, 181902 (2013).
8. Q. Ye, J. Wang, Z. Liu, Z.-C. Deng, X.-T. Kong, F. Xing, X.-D. Chen, W.-Y. Zhou, C.-P. Zhang, and J.-G. Tian, "Polarization-dependent optical absorption of graphene under total internal reflection," *Appl. Phys. Lett.* 102, 021912 (2013).
9. Hua Cheng , Shuqi Chen, Ping Yu, Xiaoyang Duan, Boyang Xie, and Jianguo Tian, "Dynamically tunable plasmonically induced transparency in periodically patterned graphene nanostrips," *Appl. Phys. Lett.* **103**, 203112 (2013).
10. Chengguo Ming, Feng Song, Xiaobin Ren, Liqun An, "Highly efficient reddish orange emission in Mn²⁺/Eu³⁺ co-doped phosphate glasses for greenhouse", *Appl. Phys. Lett.* 103, 041906 (2013).
11. Chengguo Ming, Feng Song, Liqun An, Xiaobin Ren, "Turning ultraviolet-green into red light in transparent phosphate glasses for greenhouses", *Appl. Phys. Lett.* 102, 141903 (2013).
12. Lei Wang, Wei Cai, Xinzheng Zhang, Penghong Liu, Yinxiao Xiang, and Jingjun Xu, "Mid-infrared optical near-field switching in heterogeneous graphene ribbons pairs", *Appl. Phys. Lett.* 103, 041604 (2013).
13. JunKu Liu, Qunqing Li, Mengxin Ren, Lihui Zhang, Mo Chen, Shoushan Fan. "Graphene as discharge layer for electron beam lithography on insulating substrate". *Appl. Phys. Lett.* 103, 113107 (2013). Mengxin Ren, Chongpei Pan, Qunqing Li, Wei Cai, Xinzheng Zhang, Qiang Wu, Shoushan Fan, and Jingjun Xu, "Isotropic spiral plasmonic metamaterial for sensing large refractive index change". *Opt. Lett.* 38, 3133-3136 (2013).
14. Mengxin Ren, Chongpei Pan, Qunqing Li, Wei Cai, Xinzheng Zhang, Qiang Wu, Shoushan Fan, and Jingjun Xu, "Isotropic spiral plasmonic metamaterial for sensing large refractive index change". *Opt. Lett.* 38, 3133-3136 (2013).

* 选录论文/Selected papers

15. Gui-Yang Chen, Feng Song, Hui-Tian Wang, "Sharper focal spot generated by 4π tight focusing of higher-order Laguerre–Gaussian radially polarized beam", *Opt. Lett.* 38(19), 3937–3940 (2013).
16. D. P. Yang, Z. P. Chen, F. Zhao, H. Y. Yu, T. H. Zhang, J. G. Tian, and J. J. Xu, "Observation of photorefractive surface waves in self-de focusing LiNbO₃:Fe crystal", *Opt. Lett.*, 38(16), 3093-3095 (2013).
17. Hua Cheng, Shuqi Chen, Ping Yu, Jianxiong Li, Li Deng, and Jianguo Tian, "Mid-infrared tunable optical polarization converter composed of asymmetric graphene nanocrosses," *Opt. Lett.* 38, 1567 (2013).
18. Xiaoyang Duan, Shuqi Chen, Hua Cheng, Zhancheng Li, and Jianguo Tian, "Dynamically tunable plasmonically induced transparency by planar hybrid metamaterial," *Opt. Lett.* 38, 483 (2013).
19. Zheng Cao, Xinyuan Qi, Guoquan Zhang and Jintao Bai, "Asymmetric light propagation in transverse separation modulated photonic lattices", *Opt. Lett.* 38(17), 3212-3215 (2013).
20. Wei-Guo Yan, Cui-Feng Ying, Xiang-Tian Kong, Zu-Bin Li, and Jian-Guo Tian,* "Fabrication and Optical Properties of Inclined Au Nanocup Arrays," *Plasmonics*, 8(4): 1607-1611 (2013).
21. Wei-Guo Yan, Xiang-Tian Kong, Zu-Bin Li, and Jian-Guo Tian, "Nanostructure fabricated by nanosphere lithography assisted with O₂ plasma treatment," *J. Nanosci. Nanotechnol.* 13(6), 4311-4315 (2013).
22. Liu Zhi-Bo, F. Ming, J. Wen-Shuai, X. Wei, W. Peng, S. Qi-Wen, L. Yan-Ge, D. N. Wang, Z. Wen-Yuan, and T. Jian-Guo*, "Broadband all-optical modulation using a graphene-covered-microfiber," *Laser Physics Letters* 10, 065901 (2013).
23. Cui-Feng Ying, Wen-Yuan Zhou, Yi Li, Qing Ye, Na Yang and Jian-Guo Tian, "Miniband lasing in a 1D dual-periodic photonic crystal", *Laser Phys. Lett.* 10, 056001 (2013)
24. L. J. Kong, Y. N. Li, S. X. Qian, S. M. Li, C. H. Tu, and H. T. Wang, "Encryption of ghost imaging", *Phys. Rev. A* 88, 013852 (2013).
25. X. Z. Zhang and Z. Song, "Non-Hermitian anisotropic XY model with intrinsic rotation-time reversal symmetry," *Phys. Rev. A* 87, 012114 (2013). Peilong Hong and Guoquan Zhang, "Subwavelength interference with an effective entangled source," *Phys. Rev. A* 88, 043838 (2013).
26. Zhaohui Zhai, Zhixiang Li, Jingjun Xu, and Guoquan Zhang, "Transfer and computation of optical topological charges via light pulse buffer memory in electromagnetically induced transparency solid", *Phys. Rev. A* 88, 035807 (2013).
27. Y. Hu, D. Bongiovanni, Z. Chen and R. Morandotti, Multipath multicomponent self-accelerating beams through spectrum-engineered position mapping, *Phys. Rev. A* 88, 043809 (2013).
28. Y. Pan, Y. N. Li, S. M. Li, Z. C. Ren, Y. Si, C. H. Tu, and H. T. Wang, "Vector optical fields with bipolar symmetry of linear polarization", *Opt. Lett.* 38, 3700-3703 (2013).
29. Yi Hu, Ming Li, Domenico Bongiovanni, Matteo Clerici, Jianping Yao, Zhigang Chen, José Azaña, and Roberto Morandotti, "Spectrum to distance mapping via nonlinear Airy pulses," *Opt. Lett.* 38, 380-382 (2013)
30. Yi Hu, Domenico Bongiovanni, Zhigang Chen, and Roberto Morandotti, "Periodic self-accelerating beams by combined phase and amplitude modulation in the Fourier space,"

- Opt. Lett. 38, 3387-3389 (2013)
31. X. Z. Zhang, L. Jin, and Z. Song, "Self-sustained emission in semi-infinite non-Hermitian systems at the exceptional point," *Phys. Rev. A* 87, 042118 (2013).
 32. Zhang, X. Z.; Song, Z., "Geometric phase and phase diagram for a non-Hermitian quantum XY model", *Phys. Rev. A* 88, 042108 (2013).
 33. S. M. Li, L. J. Kong, Z. C. Ren, Y. N. Li, C. H. Tu, and H. T. Wang, "Managing orbital angular momentum in second-harmonic generation", *Phys. Rev. A* 88, 035801 (2013).
 34. X. Dong, X. F. Zhou, G. R. Qian., Z. S. Zhao, Y. J. Tian, and H. T. Wang, "An ab initio study on the transition paths from graphite to diamond under pressure", *Journal of Physics: Condensed Matter* 25, 145402 (2013).
 35. Zhang, X. Z.; Song, Z., "Momentum-independent reflectionless transmission in the non-Hermitian time-reversal symmetric system", *Ann. Phys.* 339, 109 (2013).
 36. Y. Pan, S. M. Li, L. Mao, L. J. Kong, Y. N. Li, C. H. Tu, P. Wang, and H. T. Wang, "Vector optical fields with polarization distributions similar to electric and magnetic field lines", *Opt. Express* 21, 16200-16209 (2013).
 37. M. Q. Cai, C. H. Tu, H. H. Zhang, S. X. Qian, K. Lou, Y. N. Li, and H.T. Wang, "Subwavelength multiple focal spots produced by tight focusing the patterned vector optical fields", *Opt. Express* 21, 31469-31482 (2013).
 38. Ping Yu, Shuqi Chen, Jianxiong Li, Hua Cheng, Zhancheng Li, and Jianguo Tian, "Co-enhancing and -confining the electric and magnetic fields of the broken-nanoring and the composite nanoring by azimuthally polarized excitation," *Opt. Express* 21, 20611 (2013).
 39. Jianxiong Li, Shuqi Chen, Ping Yu, Hua Cheng, Xiaoyang Duan, and Jianguo Tian, "Realization of near-field linear nano-polarizer by asymmetric nanoaperture and bowtie nanoantenna," *Opt. Express* 21, 10342 (2013).
 40. Hui Guo, Hua Yu, Xinxing Zhang, Lifeng Chang, Zijian Lan, Yiming Li, and Lijuan Zhao, "Doping concentration induced phase transition in Eu^{3+} -doped $\beta\text{-PbF}_2$ nano-particles", *Opt. Express* 21(21), 24742-24752 (2013)
 41. Penghong Liu, Xinzheng Zhang, Zenghong Ma, Wei Cai, Lei Wang, and Jingjun Xu. "Surface plasmon modes in graphene wedge and groove waveguides", *Opt. Express* 21, 32432 (2013)
 42. Wending Zhang, Ligang Huang, Feng Gao,* Fang Bo, Guoquan Zhang, and Jingjun Xu, "Tunable broadband light coupler based on two parallel all-fiber acousto-optic tunable filters," *Opt. Express*, 21, 16621-16628 (2013).
 43. Feng Gao, Ravi Pant, Enbang Li, Christopher G. Poulton, Duk-Yong Choi, Stephen J. Madden, Barry Luther-Davies, and Benjamin J. Eggleton, "On-chip high sensitivity laser frequency sensing with Brillouin mutually-modulated cross-gain modulation," *Opt. Express*, 21, 8605-8613 (2013).
 44. Xiang-Tian Kong, Zu-Bin Li, and Jian-Guo Tian, "Mode converter in metal-insulator-metal plasmonic waveguide designed by transformation optics," *Opt. Express*, 21(8): 9437-9446 (2013).
 45. Q. Sheng, M. Feng, W. Xin, T. Han, Y. Liu, Z. Liu, and J. Tian, "Actively manipulation of operation states in passively pulsed fiber lasers by using graphene saturable absorber on microfiber," *Opt. Express* 21, 14859-14866 (2013).

46. Zang W-P, Yang Y, Zhao Z-Y, and Tian J-G, The effects of multiple scattering to optical forces on a sphere in an evanescent field. *Opt. Express*, 21,12373(2013)
47. Yang Y, Zang W-P, Zhao Z-Y, and Tian J-G, Morphology-dependent resonance of the optical forces on Mie particles in an Airy beam. *Opt. Express*, 21,6186-6195 (2013).
48. X. Yang, W. Q. Chen, P. Yao, T. H. Zhang,* J. G. Tian, J. J. Xu, "Observation of Surface dark Photovoltaic solitons", *Opt. Express*, 21(4), 4783-4789 (2013)
49. Z. H. Luo, F. L. Liu, Y. H. Xu, H. Y. Liu, T. H. Zhang, J. J. Xu, and J. G. Tian, "Dark surface waves in self-focusing media with diffusion and photovoltaic nonlinearities", *Opt. Express* 21(13), 15075-15080 (2013)
50. Kang Tan, David Marpaung, Ravi Pant, Feng Gao, Enbang Li, Jian Wang, Duk-Yong Choi, Steve Madden, Barry Luther-Davies, Junqiang Sun, and Benjamin J. Eggleton, "Photonic-chip-based all-optical ultra-wideband pulse generation via XPM and birefringence in a chalcogenide waveguide", *Opt. Express*, 21, 2003-2011 (2013).
51. Peilong Hong, Lei Xu, Zhaohui Zhai, and Guoquan Zhang, "High visibility two-photon interference with classical light," *Opt. Express* 21(12), 14056-14065 (2013).
52. Yi Liang, Zhuoyi Ye, Daohong Song, Cibo Lou, Xinzheng Zhang, Jingjun Xu, and Zhigang Chen, "Generation of linear and nonlinear propagation of three-Airy beams," *Opt. Express* 21(2) 1615-1622 (2013)
53. Zhandong Chen, Qiang Wu, Ming Yang, Jianghong Yao, Romano A. Rupp, Yaan Cao, and Jingjun Xu, "Time-resolved photoluminescence of silicon microstructures fabricated by femtosecond laser in air", *Opt. Express* 21, 193816 (2013)
54. Tian Tian, Yongfa Kong, Shiguo Liu, Wei Li, Shaolin Chen, Romano Rupp and Jingjun Xu, "Fast UV-Vis photorefractive response of Zr and Mg codoped LiNbO₃:Mo", *Opt. Express* 21(9), 10460-10466 (2013).
55. Hui Guo, Hua Yu, Xin-Xing Zhang, Li-Fen Chang, Zi-Jian Lan, Yi-Ming Li and Li-Juan Zhao, "Doping concentration induced phase transition in Eu³⁺-doped β -PbF₂ nano-particles", *Opt. Express* 21(21), 24742-24752 (2013). (IF=3.546)
56. Yanling Liu, Feng Song, Jun Zhang, Zhaozheng Lv, Jiadong Liu, Yin Yu, Hongyan Zhao, Huitian Wang, "Tunable local surface plasmon resonance in liquid-crystal-coated Ag nanoparticles", *Phys. Lett. A* 377(16-17), 1199-1204 (2013).
57. Qi Jiwei, Li Yudong, Yang Ming, Wu Qiang, Chen Zongqiang, Peng Jingyang, Liu Yue, Wang Wudeng, Yu Xuanyi, Sun Qian, and Xu Jingjun, "Fabrication of nanowire network AAO and its application in SERS", *Nanoscale Res. Lett.*, 8, 495 (2013)
58. Wei Li, Tianxiang Cao, Zhaohui Zhai, Xuanyi Yu, Xinzheng Zhang, and Jingjun Xu, "Influence of evanescent waves on the voxel profile in multipulse multiphoton polymerization nanofabrication", *Nanotechnology* 24, 215301 (2013).
59. Qi Jiwei, Li Yudong, Yang Ming, Wu Qiang, Chen Zongqiang, Wang Wudeng, Lu Wenqiang, Yu Xuanyi, Xu Jingjun and Sun Qian, "Large-area high-performance SERS substrates with deep controllable sub-10-nm gap structure fabricated by depositing Au film on the cicada wing", *Nanoscale Res. Lett.*, 8, 437 (2013)
60. Yinxiao Xiang, Xinzheng Zhang, Wei Cai, Lei Wang, Cuifeng Ying, and Jingjun Xu. "Optical bistability based on Bragg grating resonators in metal-insulator-metal plasmonic waveguides", *AIP Advance* 3, 012106 (2013).
61. Xian Wu, Leiting Pan, Ying Liu, Pengchong Jiang, Imshik Lee, Irena Drevensek-Olenik,

- Xinzheng Zhang, and Jing-Jun Xu, "Cell-cell communication induces random spikes of spontaneous calcium oscillations in multi-BV-2 microglial cells", *Biochem. Biophys. Res. Commun.* 431, 664-669 (2013)
62. Jianxiong Li, Shuqi Chen, Ping Yu, Hua Cheng, Lunjie Chen, and Jianguo Tian, "Indirectly Manipulating Nanoscale Localized Fields of Bowtie Nanoantennas with Asymmetric Nanoapertures," *Plasmonics* **8**, 495 (2013).
63. Cui-Feng Ying, Wen-Yuan Zhou, Yi Li, Qing Ye, Na Yang and Jian-Guo Tian, "Multiple and colorful cone-shaped lasing induced by band-coupling in a 1D dual-periodic photonic crystal", *AIP Advances* 3, 022125 (2013)
64. Qing Ye, Wenyuan Zhou, Jin Wang, Chunping Zhang, Jianguo Tian, "Study on effective probe depth of optical coherence tomography system by Monte Carlo simulation", *Optik* 124, 4909-4911(2013)
65. Jin Wang, Qing Ye, Zhichao Deng, Tengqian Sun, Wenyuan Zhou, Jianchun Mei, Chunping Zhang, Jianguo Tian, "Study of dynamic pressure-induced refractive index change using derivative total reflection method", *J. Biomed. Opt.* 18(11), 117005(2013)
66. X. Yang, X. K. Ren, C. X. Ma, T. H. Zhang,* J. G. Tian, J. J. Xu, "The regulation of the photorefractive surface solitons in photorefractive crystal", *J. Opt. Soc. B*, 30(5), 1194 - 1199 (2013)
67. An-Chang Shi and Bao-Hui Li, "Self-assembly of diblock copolymers under confinement", *Soft Matter* 9, 1398-1413 (2013). (IF=3.909)
68. Jin Ge, Li-Juan Zhao, Hui Guo, Zi-Jian Lan, Li-Fen Chang, Yi-Ming Li and Hua Yu, "Structure and distortion of lead fluoride nanocrystals in rare earth doped oxyfluoride glass ceramics", *Phys. Chem. Chem. Phys.* 15, 17281 (2013). (IF=3.829)
69. Ji-Hua Xu, Yu-Yua Yin, Zheng Wang, Run Jiang*, Bao-Hui Li and An-Chang Shi, "Self-assembled morphologies of ABA triblock copolymer brushes in selective solvents," *J. Chem. Phys.* 138, 114905(1-12) (2013). (IF=3.164)
70. Yanling Liu, Feng Song, Jiadong Liu, Jun Zhang, Yin Yu, Hongyan Zhao, "Enhancement of luminescent emission in $\text{Er}^{3+}/\text{Yb}^{3+}$ co-doped $\text{Y}_2\text{Ti}_2\text{O}_7$ films with Ag/Au nanoparticles", *Chem. Phys. Lett.* 565, 98-101 (2013).
71. Z.-B. Liu, Z. Guo, X.-L. Zhang, J.-Y. Zheng, and J.-G. Tian, "Increased optical nonlinearities of multi-walled carbon nanotubes covalently functionalized with porphyrin," *Carbon* 51, 419-426 (2013).
72. X.-D. Chen, Z.-B. Liu, C.-Y. Zheng, F. Xing, X.-Q. Yan, Y. Chen, and J.-G. Tian, "High-quality and efficient transfer of large-area graphene films onto different substrates," *Carbon* 56, 271-278 (2013).
73. Yin Yu, Feng Song, Chengguo Ming, Jun Zhang, Fengxiao Wang, "Photoluminescence properties of $\text{Tm}^{3+}/\text{Tb}^{3+}/\text{Eu}^{3+}$ tri-doped phosphate glass and glass ceramics for white-light-emitting diodes", *Appl. Opt.* 52(23), 5606-5610 (2013).
74. Yin Yu, Feng Song, Chengguo Ming, Jiadong Liu, Wei Li, Yanling Liu, Hongyan Zhao, "Color-tunable emission and energy transfer in $\text{Tm}^{3+}/\text{Dy}^{3+}/\text{Sm}^{3+}$ tri-doped phosphate glass for white light emitting diodes", *Opt. Commun.* 303, 62-66 (2013).
75. Hongyan Zhao, Feng Song, Jun Zhang, Fengxiao Wang, Jiadong Liu, Yanling Liu, "Fluorescence quenching of osthole by silver nanoparticles", *J. Opt. Soc. Am. B*, 30(9), 2387-2392 (2013).

76. Hongyan Zhao, Feng Song, Fengxiao Wang, Jiadong Liu, Yanling Liu, Jun Zhang, Guiyang Chen, Shujing Liu, "The Role of Silver and Gold Nanoparticles in Enhancing Luminescence of Europium Complexes", *J. Nanosci. Nanotechnol.* 13, 1–6 (2013).
77. Hongyan Zhao, Feng Song, Shujing Liu, Guiyang Chen, Chen Wei, Yanling Liu, Jiadong Liu, "A Fluorescence Spectroscopy Study of Traditional Chinese Medicine Angelica", *Opt. Spectrosc.* 115(4), 530–536 (2013).
78. Jin Ge, Lijuan Zhao, Hui Guo, Zijian Lan, Lifeng Chang, Yiming Li, and Hua Yu, "Structure and distortion of lead fluoride nanocrystals in rare earth doped oxyfluoride glass ceramics", *Phys. Chem. Chem. Phys.* 15, 17281 (2013)
79. Wenqiang Lu, Chengming Jiang, Daniel Caudle, Chaolong Tang, Qian Sun, Jingjun Xu, and Jinhui Song, "Controllable growth of laterally aligned zinc oxide nanorod arrays on a selected surface of the silicon substrate by a catalyst-free vapor solid process - a technique for growing nanocircuits", *Phys. Chem. Chem. Phys.* 15, 13532-13537(2013).
80. Wending Zhang, Ligang Huang, Feng Gao, Fang Bo, Guoquan Zhang* and Jingjun Xu, "All-fiber tunable Mach-Zehnder interferometer based on an acousto-optic tunable filter cascaded with a tapered fiber" *Optics Communications*, 292, 46-48(2013).
81. Lei Xu, Yi Yin, Fang Bo, Jingjun Xu, Guoquan Zhang, "Transverse localization of light in the disordered one-dimensional waveguide arrays in the linear and nonlinear regimes", *Opt. Commun.* 296, 65-71 (2013).
82. Huo, Ming-Xia; Li, Ying; Song, Z. H. I.; et al., "A Quantum simulator for probing Mott lobes via the AC Josephson effect", *Int. J. Quantum Inform.* 11, 1350049 (2013).
83. Hu, W. H.; Jin, L.; Song, Z., "Dynamics of one-dimensional tight-binding models with arbitrary time-dependent external homogeneous fields", *Quantum Information Processing* 12, 3569 (2013).
84. Jun Qian, Chen-xu Liu, Wu-deng Wang, Jing Chen, Yu-dong Li, Jing-jun Xu, and Qian Sun, "Effect of Edge Rounding on the Extinction Properties of Hollow Metal Nanoparticles", *Plasmonics* 8, 955-962 (2013).
85. Xinhui Tan, Junliao Wang, Wei Cai, Tao Meng, Yinxiao Xiang, Wei Li, and Xinzheng Zhang, "Coherence preservation during light-surface plasmon polaritons-light transformation", *Science China Physics, Mechanics and Astronomy*, 56(9), 1679-1683 (2013)
86. Leiting Pan, Kun Song, Fen Hu, Wenwu Sun, and Imshik Lee, "Nitric oxide induces apoptosis associated with TRPV1 channel-mediated Ca²⁺ entry via S-nitrosylation in osteoblasts", *European Journal of Pharmacology* 715, 280-285 (2013)
87. Zhandong Chen, Qiang Wu, Ming Yang, Baiquan Tang, Jiangong Yao, Romano A. Rupp, Yaan Cao, and Jingjun Xu, "Generation and evolution of plasma during femtosecond laser ablation of silicon in different ambient gases", *Laser and particle beams* 31, 539 (2013)
88. Blaz Tasic, Wei Li, Antoni Sánchez-Ferrer, Martin Copic, Irena Drevensek-Olenik, "Light-Induced Refractive Index Modulation in Photoactive Liquid-Crystalline Elastomers", *Macromol. Chem. Phys.* 214(23), 2744–2751 (2013).
89. Qiang Wu, Qingquan Chen, Bin Zhang, and Jingjun Xu, "Terahertz phonon polariton imaging", *Front. Phys.* 8 (2), 217–227 (2013)
90. Yong-Qiang Cao, Yan-Long Yu, Peng Zhang, Lan-Lan Zhang, Tao He and Ya-An Cao, "Enhanced visible-light photocatalytic activity of TiO₂ by nitrogen and nickel-chlorine modification", *Separation and Purification Technology* 104, 256-262 (2013). (IF=2.894)

91. Qiong-Qiong Hou, Fan-Jie Meng and Jia-Ming Sun, "Electrical and optical properties of Al-doped ZnO and ZnAl₂O₄ films prepared by atomic layer deposition", *Nanoscale Research Letters* 8, 144 (2013). (IF=2.524)
92. Peng Chi, Zheng Wang, Yu-Yua Yin, Bao-Hui Li, An-Chang Shi, "Finite-length effects on the coil-globule transition of a strongly charged polyelectrolyte chain in a salt-free solvent", *Phys. Rev. E* 87, 042608 (1-6) (2013). (IF=2.313)
93. Yan-Long Yu, En-Jun Wang, Ji-Xiang Yuan and Ya-An Cao, "Enhanced photocatalytic activity of titania with unique surface indium and boron species", *Applied Surface Science* 273, 638-644 (2013). (IF=2.112)
94. Liang Gong, Yong-Chun Shu, Jing-Jun Xu, Qin-Sheng and Zhan-Guo Wang, "Numerical analysis on quantum dots-in-a-well structures by finite difference method", *Superlattices and Microstructures*, 60, 311-319 (2013). (IF=1.564)
95. K. Lou, S. X. Qian, Y. N. Li, C. H. Tu, and H. T. Wang, "Grating-assisted surface plasmons resonance in 2D microstructures induced by femtosecond vector fields", *Proc. SPIE* 8796, 2nd International Symposium on Laser Interaction with Matter (LIMIS 2012), 87960Y (2013).
96. Xue Cao, Yong-Chun Shu, Yong-Neng Hu, Guang-Ping Li and Chang Liu, "Integrated process of large-scale and size-controlled SnO₂ nanoparticles by hydrothermal method", *Transaction of Nonferrous Metals Society of China*, 23,725-730 (2013). (IF=0.917).
97. Shiqiang Xia, Daohong Song, Liqin Tang, Cibo Lou, and Yigang Li, "Self-trapping and oscillation of quadruple beams in high band gap of 2D photonic lattices," *Chin. Opt. Lett.* 11, 090801- (2013)
98. Chen Zong-Qiang, Qi Ji-Wei, Chen Jing, Li Yu-Dong, Hao Zhi-Qiang, Lu Wen-Qiang, Xu Jing-Jun and Sun Qian, "Fano Resonance Based on Multimode Interference in Symmetric Plasmonic Structures and its Applications in Plasmonic Nanosensors" *Chin.Phy.Lett.*30, 057301(2013).
99. Xie Nan, Gong Hui-Qi, Zhou Zhi, Guo Xiao-Dong, Yan Shi-Chao, Sun Qian, Xing Sirui, Wu Wei, Pei Shin-shem, Bao Jiming³, Shan Xin-Yan², Guo Yang and Lu Xing-Hua, "Visualization of a Maze-Like Reconstruction of Graphene on a Copper Surface at the Atomic Scale", *Chin.Phy.Lett.*30, 056802(2013)
100. Zhenhua Wang, Yue Wu, Xinzheng Zhang, Zhiqiang Yun, Wei Li, and Jingjun Xu, "Quantitative analysis of the self-absorption and reemission effects on the emission spectrum of photoluminescence in right-angle excitation- detection configuration", *Chin. Phys. B* 22(11), 113301-7 (2013)
101. Zongqiang Chen, Jing Chen, Yudong Li, Jun Qian, Jiwei Qi, Jingjun Xu, Qian Sun, "Highly Efficient Narrow-band Plasmonic Waveguide Filter Based on Cascaded Slot Cavities", *Chin. Opt. Lett.* 11(11), 112401 (2013)
102. Juanying Zhao, Peng Zhang, Dongmei Deng, Cibo Lou, Daohong Song, Jingjiao Liu, Zhigang Chen. Self-accelerating and self-breathing Bessel-like beams along arbitrary trajectories. *Chin. Opt. Lett.*, 11(11): 110701 (2013)
103. 张学智, 冯鸣, 张心正, "基于自相位调制效应的硅基中红外全光二极管", *物理学报* 62(2) 024201-7 (2013).
104. 云志强, 魏汝省, 李威, 罗维维, 吴强, 徐现刚, 张心正, "6H-SiC 的飞秒激光超衍射加工", *物理学报* 62(6), 068101 (2013).
105. 任梦昕, 许京军, "表面等离子体激元增强非线性的原理及应用", *激光与光电子学进展*

50, 080002 (2013).

106. 郭丽梅, 匡元江, 杨晓丹, 于彦龙, 姚江宏, 曹亚安, “偏硼酸铯催化剂光催化还原 CO_2 合成 CH_4 ”, 物理化学学报, 29, 397-402 (2013)。 (IF=0.869)
107. 张鹏, 赵路松, 姚江宏, 曹亚安, “不同浓度 Sn^{4+} 离子掺杂 TiO_2 的结构、性质和光催化活性”, 物理化学学报, 29, 1305-1312 (2013)。 (IF=0.869)
108. 郭丽梅, 匡元江, 杨晓丹, 于彦龙, 姚江宏, 曹亚安, “偏硼酸铯/碳酸铯复合催化剂光催化还原 CO_2 合成 CH_4 ”, 物理化学学报, 29, 1558-1565 (2013)。 (IF=0.869)
109. 徐纪华, 蒋润, 尹玉华, 王铮, 李宝会, “锚定非对称 ABA 三嵌段共聚物在选择性溶剂中自组装行为的模拟退火研究”, 高分子学报, 10, 1277-1284 (2013)。 (IF=0.677)
110. 王富章, 陈彬, 孙军, 窦飞飞, 张玲, 胡永钊, 许京军, “低应力铌酸锂电光调 Q 开关的研究”, 人工晶体学报, 42(7), 1315-1318 (2013)。
111. 张鹏, 于彦龙, 匡元江, 曹亚安, “Si 掺杂 TiO_2 催化剂的结构和可见光催化活性研究”, 影像科学与光化学, 31, 295-304 (2013)。

出版专著:

1. Hui-Tian Wang, Chapter2: Vector Optical Fields and Their Novel Effects, World Scientific Publishing company 9814449881 (2013).
2. 刘智波, 石墨烯——一种新型碳纳米材料 (第四章), 科学出版社 9787030375384 (2013)。

专利/Patents

申请专利/ Patents Applied

- [1] 201310005489.7; 一种基于石墨烯偏振特性的多层膜光存储方法; 发明; 刘智波, 邢飞, 田建国。(2013.1.7)
- [2] 201310001215.0; 基于新型微结构光纤的高效荧光检测; 发明; 周文远, 李志莉, 刘艳格, 田建国。(2013.1.22)
- [3] 201310007951.7; 一种飞秒激光直写制备微孔阵列的系统与方法; 发明; 李勇男, 娄凯, 钱升霞, 涂成厚, 王慧田。(2013.03)
- [4] 201310061246.5; 一种快速、简易制备大面积单层胶体微球阵列的方法; 发明; 李祖斌, 闫卫国, 田建国。(2013.4)
- [5] 201310201407.6; 一种多线胶体金试纸条定量分析图像处理方法; 发明; 叶青, 梅剑春, 田建国。(2013.5.24)
- [6] 201310201408.0; 胶体金试纸定量分析中的参照定时分析方法; 发明; 叶青, 梅剑春, 田建国。(2013.5.24)
- [7] 201310201409.5; 多波长毛细管电泳荧光激发装置; 发明; 叶青, 梅剑春, 田建国。(2013.5.24)
- [8] 201310201410.8; 双光源照明金标免疫层析试纸检测分析方法; 发明; 叶青, 梅剑春, 田建国。(2013.5.24)
- [9] 201320295194.3; 双光源照明金标免疫层析试纸检测分析装置; 实用新型; 叶青, 梅剑春, 田建国。(2013.5.24)
- [10] 201310244383.2; 选择性填充光子晶体光纤方法; 发明; 周文远, 李志莉, 刘艳格, 马跃, 叶青, 田建国。(2013.7.15)
- [11] 2013101904827; 一种高性能表面增强拉曼散射基地的制作方法; 发明; 齐继伟。(2013.7.22)
- [12] 201310244381.3; 空间频率生物芯片; 发明; 周文远, 门双仁, 惠王伟, 叶青, 田建国。(2013.8.20)
- [13] 201310366961.X; 一种石墨烯选择性定点转移方法; 发明; 刘智波, 陈旭东, 田建国。(2013.8.21)
- [14] 201310444659.1; 一种 CCD 波长校准的方法; 发明; 徐晓轩, 李昊宇, 王斌。(2013.09.27)
- [15] 201310511543.5; 一种透明基座上石墨烯层数测量方法; 发明; 刘智波, 王鹏, 田建国。(2013.10.24)
- [16] 201310511626.4; 一种基于石墨烯的单细胞传感方法; 发明; 刘智波, 邢飞, 田建国。(2013.10.24)
- [17] 201310524507.2; 磁颗粒荧光聚集检测装置; 发明; 叶青, 邓志超, 王瑾, 孙腾骞, 张春平, 田建国。(2013.10.28)

- [18] 201310524601.8; 基于全内反射法的宽光谱范围物质色散的自动测量装置; 发明; 叶青, 邓志超, 王槿, 孙腾骞, 张春平, 田建国。(2013.10.28)
- [19] 201310528913.6; 微型转动扫描傅里叶变换光谱仪; 发明; 徐晓轩, 李昊宇, 王斌。(2013.11.01)
- [20] 201310297706.4; 一种AZO纳米分体和AZO烧结体的制备方法; 发明; 舒永春。(2013.11.12)
- [21] 201210543892; 一种硫掺杂硅纳米颗粒的制备方法; 发明; 吴强, 杨明, 左一平, 陈战东, 姚江宏, 孔勇发, 唐柏权, 许京军。(2013.3.20)
- [22] 201210543908; 一种大面积表面增强拉曼散射基底的制备方法; 发明; 吴强, 杨明, 齐继伟, 马寅星, 陈战东, 张心正, 孙骞, 许京军。(2013.4.10)

授权专利/ Patents Approved

- [1] ZL201110064158.1; 掺铈铈酸锂多孔材料制备方法及其制备材料; 发明; 张心正, 石凡, 孔勇发, 许京军, 陈绍林, 王丕东, 张玲, 孙骞。(2013.1.9)
- [2] ZL201010615872.0; 一种高活性硼酸铟复合氮掺杂二氧化钛光催化剂; 发明; 曹亚安, 袁继翔。(2013.6.19)
- [3] ZL201010219274.1; 一种高效率类硼酸铟光催化剂; 发明; 曹亚安, 杨晓丹。(2013.7.17)
- [4] ZL201210203315.7; 一种近化学计量比钽酸锂晶体的制备方法; 发明; 孙军, 许京军, 李威, 杨金凤, 张玲, 孔勇发, 张华。(2013.12.11)
- [5] ZL201210203084.X; 一种近化学计量比铈酸锂晶体的制备方法; 发明; 孙军, 许京军, 李威, 张华, 张玲, 孔勇发, 杨金凤。(2013.12.11)
- [6] ZL 201320295195.8; 光纤式小体积金标免疫层析试纸检测仪; 实用新型; 叶青, 梅剑春, 田建国。(2013.10.9)
- [7] ZL 201320295193.0; 多波长毛细管电泳荧光激发器; 实用新型; 叶青, 梅剑春, 田建国。(2013.11.27)

国际合作与交流/International Cooperation and Exchange

来访人员名单/Visitors List

序号	姓名	国家或地区	单位	技术职称	报告题目	来访时间	来访目的
1.	Alfons van Blaaderen	荷兰	Utrecht University	教授	Manipulating Complex Colloids with Electric Fields	2013.1.3	学术交流
2.	Irena Drevenšek Olenik	斯洛文尼亚	斯特藩研究所	副教授		2013.1.19-2013.2.13	合作研究
3.	Romano Rupp	奥地利	维也纳大学	教授		2013.1.19-2013. 2.13	合作研究
4.	Michael Meingassner	奥地利	维也纳大学	硕士生		2013.1.18-2013.1.31	合作研究
5.	Peter Hertel	德国	Univ. of Osnabrueck	教授	Assorted Lectures on Physics; Lectures on Fundamental Optics	2013.4.25-6.5	讲学
6.	宋金会	美国	阿拉巴马大学工程学院冶金材料工程系/信息技术材料中心	助理教授	基于纳米氧化锌阵列的绿色能源系统	2013.5.3	工作访问 学术交流
7.	An-Chang Shi	加拿大	McMaster University	教授		2013.5.16-20	工作访问 学术交流
8.	Lucija Coga	斯洛文尼亚	斯特藩研究所	博士生	Self-organization of lipoguanosine derivatives on water surface and after transfer to solid substrates	2013.5.19-6.1	合作研究

9.	Qiang (David) Wang	美国	Colorado State University	副教授		2013.6.20-22	工作访问 学术交流
10.	Liqun Gu	美国	密苏里大学	副教授		2013.7.3-25	访问
11.	曾汉奇	香港	香港中文大学	教授		2013.7.11-13	工作访问 学术交流
12.	Juliane Andrea Tschentscher	德国	奥斯纳布鲁克大学	硕士生	Improvement of the experimental conditions of the z-scan- experiment with 100fs-laser pulses - I	2013.9.3-9.30	合作研究
13.	Pia Baeune	德国	奥斯纳布鲁克大学	硕士生	Improvement of the experimental conditions of the z-scan- experiment with 100fs-laser pulses - II	2013.9.3-9.30	合作研究
14.	Andrii ILYIN	乌克兰	乌克兰科学院物理所	研究员	Nonlinear dynamics of grating recording in dye-doped chiral nematic liquid crystals	2013.10.10-11.9	合作研究
15.	Daniel R. Grischkowsky	美国	Oklahoma State University	教授	THz Photonics: The Synergy of Ultrafast Optics, Electronics, Micro-Microwaves, and Quasi-Optics	2013.10.21	工作访问 学术交流
16.	吴强	爱尔兰	爱尔兰理工学院	教授		2013.11.14	学术交流

出访人员名单/Personnel exchange Researchers List

序号	姓名	国家或地区	单位	职称或职位	出访时间	出访目的
1.	楼慈波	德国	汉堡军大	副教授	2011.4-2013.4	访问学习
2.	高峰	澳大利亚	悉尼大学 CUDOS研究室	副教授	2012.4-2013.3	合作研究
3.	宋峰	香港		教授	2013.1.14-2013.1.21	学术交流
4.	宋峰	瑞士	瑞士洛桑联邦理工学院	教授	2013.4.1-2013.4.7	IPT2013 竞赛
5.	宋峰	印度尼西亚	印度尼西亚教育部和SURYA学院	教授	2013.5.4-2013.5.13	第14届亚洲物理奥林匹克竞赛
6.	李宝会	美国	加州大学河滨分校 (University of California, Riverside)	教授	2013.6.26-2013.7.1	访问交流
7.	宋峰	丹麦	丹麦理工大学	教授	2013.7.7-2013.7.16	第44届国际物理奥林匹克竞赛
8.	宋峰	台湾	国立台湾师范大学	教授	2013.7.24-2013.7.31	IYPT 竞赛
9.	鄢小卿	瑞士	洛桑联邦理工学院	讲师	2013.8.24-12.10	合作交流
10.	宋峰	俄罗斯	俄罗斯科学院激光物理研究所	教授	2013.8.24-2013.9.1	学术交流
11.	张心正	乌克兰	切尔诺维茨大学	教授	2013.9.17-9.22	国际会议
12.	李祖斌	美国	Northeastern University	副教授	2013.9-2014.9	访问学者

研究生交流情况/Personnel exchange Students List

序号	姓名	国家或地区	单位	博士生/硕士生	出访时间	出访目的
1.	王垒	美国	Rice University	博士生	2013.10.01-2013.12.31	合作研究
2.	崔伟	斯洛文尼亚	斯特藩研究所	硕士生	2013.7.15-2013.8.15	合作研究
3.	刘悦	美国	Rutgers, The State	博士生	2012.9	联合培养

			University of New Jersey			
4.	韦晨	美国	亚利桑那大学	博士生	2011.7-2013.7	联合培养

引进人才名单/New Staff

序号	姓名	性别	出生年月	职称	研究方向
1	胡毅	男	1983.6	副教授	非线性光学

国内、国际会议报告/Talks at Conferences

- 1 Guoqiang Zhang " Manipulation of optical topological charges via atomic coherence gratings in Pr³⁺:YSO crystal based on electromagnetically induced transparency effect", The 14th conference on photorefractive effects, materials and devices, Winchester, UK, 2013 Sep 3-6 (**invited talk**).
- 2 Zhigang. Chen, "Optimal Control of Self-Accelerating Beams",15th Photonic North Conference, Ottawa, June 3-5, 2013. (**invited talk**)
- 3 Zhigang. Chen, "Nonlinear spatial beam dynamics in optical systems" workshop on "Nonlinear Schrödinger equation: theory and applications", Heraklion, Crete, May 20 – 24, 2013 (**invited talk**)
- 4 Yongfa Kong, Shiguo Liu, Shaolin Chen, Jingjun Xu, The effects of high-valent dopants on lithium niobate crystals, International Workshop on Stoichiometric Lithium Niobate, Goslar, Germany, September, 18-20 (2013). P 25-27 (**invited talk**)
- 5 Liqin Tang, Yan Xu, Xinzhen Zhang, Sanming Yi, Yinxiao Xiang, Daohong Song, Jingjun Xu*, "Balanced extended-modes in quasi-periodic photonic lattices", the 11th International Conference on Correlation Optics, Chernivtsi, Ukraine, Sep. 18-21 (2013) (invited talk)
- 6 Baohui Li, "A simulation study of the coil-globule transition of a strongly-charged polyelectrolyte chain in a salt-free solvent", The 9th China-Korea Bilateral Symposium on Polymer Materials, Changsha, China, July 14-18(2013). (**invited talk**)
- 7 Baohui Li, "A simulation study of the coil-globule transition of a polyelectrolyte chain in solution", Emergent and Adaptive Behaviors in Soft Matter and Living Systems, Xiamen, China, September 15-18, 2013. (**invited talk**)
- 8 Shuqi Chen, Xiaoyang Duan, Haifang yang, Hua Cheng, Junjie Li, Wenwei Liu, Changzhi Gu, and Jianguo Tian, "Polarization insensitive and wide-angle plasmonically induced transparency by planar metamaterial," TechConnect World, Maryland, U.S.A., May 13-16 (2013).
- 9 Feng Gao, Ligang Huang, Guoqiang Zhang and Jingjun Xu, "Locating High sensitivity window in Brillouin mutually modulated cross gain modulation sensing", The 14th conference on photorefractive effects, materials and devices, Winchester, UK, 2013 Sep 3-6.
- 10 Feng Gao, Ravi Pant, Enbang Li, Christopher G. Poulton, Duk-Yong Choi, Stephen J. Madden, Barry Luther-Davies, and Benjamin J. Eggleton, "On-chip high sensitivity laser frequency sensing with Brillouin mutually-modulated cross-gain modulation," CLEO, San Jose CA USA, 2013 Jun 9-14.
- 11 Zongqiang Chen, Jing Chen, Yudong Li, Jingjun Xu, and Qian Sun, "Narrow-band filter based on cascaded nanodisks embedded in an Metal-insulator-metal waveguide ", International Conference on Nonlinear Optics, Bellevue, WA, USA, July 14-18(2013).

- 12 Baohui Li, "Coil-globule transition of a strongly-charged polyelectrolyte chain in a salt-free solvent: A Replica Exchange Monte Carlo Study", The 87th Colloid and Surface Science Symposium, Riverside, California, USA, June 23-26, 2013.
- 13 Honde Liu, Rong Zhang, Shoujun Zheng, Xiaoyao Zhang, Shiguo Liu, Shaolin Chen, Yongfa Kong, Jingjun Xu, "The study of light assisted poling in Mg-doped LiNbO₃", International Conference on Photorefractive effects, materials and devices (PR'13), Winchester, United Kingdom, September, 4-6(2013).
- 14 Yongfa Kong, Tian Tian, Shiguo Liu, Shaolin Chen, Jingjun Xu, The photorefractive properties of high-valent ions doped lithium niobate crystals, International conference on photorefractive effects, materials and devices (PR'13), Winchester, England, Sep. 4-6 (2013). P34.
- 15 Xinyu Ge, Yongfa Kong, Feifei Xin, Guoquan Zhang, Wei Li, Jingjun Xu, The ultraviolet photorefractive in Sn-doped lithium niobate crystals, International conference on photorefractive effects, materials and devices (PR'13), Winchester, England, September, 4-6 (2013). P32.
- 16 Dahuai Zheng, Yongfa Kong, Shiguo Liu, Shaolin Chen, Liwei Wang, and Jingjun Xu, The photorefractive characteristics of bismuth-oxide doped lithium niobate crystals, International conference on photorefractive effects, materials and devices (PR'13), Winchester, England, September, 4-6 (2013). P82
- 17 Tongqing Sun, Yu Zhang, Shaolin Chen, Yongfa Kong, Jingjun Xu, "Growth, morphology, thermal characteristic and spectroscopic properties of Nd³⁺ doped KGdP₄O₁₂ crystal, a new promising laser material", The 17th International Conference on Crystal Growth and Epitaxy, Warsaw, Poland, August 11-16, 2013.
- 18 Peilong Hong and Guoquan Zhang, "Subwavelength interference with classical light," in CLEO/Europe-IQEC 2013 Conference, IA-P.29, May 12-16, 2013, Munich, Germany. (Poster)
- 19 Yi Liang, Daohong. Song, Cibo. Lou, Xinzhen. Zhang, Jingjun. Xu, and Zhigang. Chen, "Generation and propagation of partially spatially incoherent Airy beams," in Conference on Lasers and Electro-Optics(CLEO), San Jose, USA ,June 9-14, 2013 (oral talk)
- 20 Zhandong Chen, QiangWu, Ming Yang, and Jingjun Xu, "Time-resolved study of femtosecond laser-induced plasma on silicon," Frontiers in Optics/Laser Science 2013 (FIO/LS 2013), Orlando, USA, Oct. 6-10, (2013) (Oral).
- 21 Ming Yang, Qiang Wu, Jiwei Qi, Zhandong Chen, and Jingjun Xu, "A large area polymer-based substrate with broadband absorption for surface enhanced Raman scattering", San Jose, CA, USA, June 9-14 (2013) (Poster)
- 22 Leitong Pan, Cunbo Li, Pengchong Jiang, Xinzhen Zhang, Jingjun Xu, "Ultraviolet Irradiation Induces Membrane Rigidity in Human Erythrocytes", 11th International Conference on Photonics and Imaging in Biology and Medicine, Wuhan, China, May 26-29 (2013) (Poster)

- 23 Wei Cai, Penghong Liu, Lei Wang, Xinzheng Zhang, Jingjun Xu, "Surface plasmons in graphene wedge and groove waveguides," The 6th International Conference on Surface Plasmon Photonics, Ottawa, Canada (2013.5.26-31) (Poster)
- 24 Lei Wang, Wei Cai, Xinzheng Zhang, Jingjun Xu, "Terahertz optical near-field switching in heterogeneous graphene ribbon pairs," The 6th International Conference on Surface Plasmon Photonics, Ottawa, Canada (2013.5.26-31) (Poster)
- 25 Yinxiao Xiang, Xinzheng Zhang, Wei Cai, Jingjun Xu, "Optical bistability based on Bragg grating resonators in metal-insulator-metal plasmonic waveguides," The 6th International Conference on Surface Plasmon Photonics, Ottawa, Canada (2013.5.26-31) (Poster)
- 26 宋峰, "稀土掺杂发光和光纤激光器特性", 第 3 届中俄激光物理、基础与应用光子学暑期学校, 俄罗斯 (2013.8.24-9.1). (大会报告)
- 27 许京军, 任梦昕, 蔡卫, 张心正, "Novel nonlinear optical effects in plasmonic metamaterials", 第八届全国激光技术与光电子学学术会议, 上海, 2013.03 (邀请报告)
- 28 刘智波 鄢小卿 邢飞 叶青 田建国"全内反射结构下石墨烯光学性质的偏振依赖"中国物理学会 2013 年秋季学术会议, 厦门 (2013.9.12-9.15)。 (邀请报告)
- 29 蔡卫, 王垒, 刘鹏翊, 张心正, 许京军, "Surface Plasmons in Various Graphene Structures", 泰山学术论坛——先进催化材料专题, 中国济南 (2013.11.14-16) (邀请报告)
- 30 李宝会, "嵌段共聚物受限自组装", Symposium on Soft Matter, 上海 (2013.11.30-12.1)。 (邀请报告)
- 31 孙甲明, "纳米层状结构硅基电致发光器件的原子层尺度构建及其光电性能研究", 第 13 届全国发光学学术会议, 南京 (2013.4.20-23)。 (邀请报告)
- 32 李勇男, "矢量光场特性及其应用研究", 2013 年中国光学学会学术大会, 长沙 (2013.8.16-18)。 (邀请报告)
- 33 李宝会, "聚电解质单链构象转变的模拟研究", 2013 年全国高分子学术论文报告会, 上海 (2013.10.12-16)。 (分会邀请报告)
- 34 任梦昕, 许京军, "等离子超材料中的非线性光学效应", 天津市物理学会年会, 天津, 2013.05 (口头报告)
- 35 潘雷霆, 孟桂先, 李任植, 张心正, 许京军, "新 Fluo-3 AM 染色方法改进贴壁细胞核钙成像", 第十三次中国生物物理学术大会, 南昌 (2013.10.28-11.1) (口头报告)
- 36 潘雷霆, 杨淑英, 张心正, 许京军, "532 nm 激光对滑膜细胞致死作用的研究", 第十三次中国生物物理学术大会, 南昌 (2013.10.28-11.1) (口头报告)
- 37 李文华, 王振华, 吴玉娥, 吴强, 张心正, "ZnS 飞秒超连续泵浦探测非简并双光子吸收研究", 中国物理学会秋季学术会议, 厦门 (2013.9.12-15) (口头报告)
- 38 刘智波, 邢飞, 鄢小卿, 叶青, 陈旭东, 田建国, "石墨烯在全内反射结构下的光学性质及其应用", 第五届全国光学青年学术论坛, 太原 (2013.7.31-8.4)。口头报告

- 39 吴玉娥, 王振华, 李文华, 吴强, 张心正, “利用泵浦-探测方法研究 ZnS 的超快特性”, 中国物理学会秋季学术会议, 厦门 (2013.9.12-15) (口头报告)
- 40 李思颀, 孔令军, 任志成, 李勇男, 涂成厚, 王慧田, “Orbital angular momentum and its conservation in second-harmonic generation”, 中国物理学会 2013 秋季物理学术会议, 厦门 (2013.9.12-15)。(光学分会口头报告)
- 41 潘岳, 蔡孟强, 李勇男, 涂成厚, 王慧田, “矢量光场紧聚焦对称性的分析与应用”, 中国物理学会 2013 秋季物理学术会议, 厦门 (2013.9.12-15)。(光学分会口头报告)
- 42 徐晓轩, 第二十届全国光谱仪器与分析监测学术研讨会, 中国江苏镇江, (2013.10)。
- 43 郭辉, 余华, 常丽芬, 等. “不同浓度稀土离子掺杂的微晶结构的研究”. 第 13 届全国发光光学学术会议, 南京(2013.4.20-23)
- 44 林妙玲, 赵丽娟, 兰子鉴, 常丽芬, 余华, “氟氧化物微晶玻璃散射效率的研究”, 第十七届全国光散射学术会议, 陕西西安 (2013.10.20-22)
- 45 张国权, 翟召辉, 李志向, 许京军, “原子相干光栅及其应用”, 第五届全国信息光学与光子学学术会议 (CIOP2013) (2013 年 11 月 26 日-30 日), 厦门。
- 46 唐莉勤, 徐燕, 张心正, 易三铭, 许京军“无序光子晶格中平衡扩展态的研究”, 泰山学术论坛——光电材料与器件专题, 邀请报告, 中国青岛 (2012.10.26-28)
- 47 潘雷霆, 许京军, “生物光学成像技术-时间与空间信息博弈”, 天津市物理学会年会, 天津, 2013.05 (口头报告)
- 48 任梦昕, 许京军, “等离激元超材料中的非线性效应”, 第五届全国光学青年学术论坛, 太原, 2013.08
- 49 任梦昕, 许京军, “非线性等离激元超材料”, 中国光学学会学术大会, 长沙, 2013.08
- 50 任梦昕, 许京军, 刘军库, 张立辉, 陈墨, 李群庆, 范守善, “互补结构双层超材料的制备及其光学性质”, 国际强激光与物质相互作用及其应用研讨会, 苏州, 2013.10
- 51 潘雷霆, 陈定璿, 李存波, 张心正, 许京军, “基于光刻微加工技术的牛血管间质干细胞体外自组织图案控制的研究”, 第十三次中国生物物理学术大会, 南昌 (2013.10.28-11.1)
- 52 潘雷霆, 吴限, 张心正, 许京军, “BV-2 小胶质细胞间钙波传递特性的研究”, 第十三次中国生物物理学术大会, 南昌 (2013.10.28-11.1)
- 53 于彦龙, 曹亚安, “N-TiO₂/InBO₃ 复合催化剂的制备及其光催化性能”, 第 2 届光功能材料与光电化学学术研讨会, 武汉 (2013.11.12-15)。
- 54 郭丽梅, 曹亚安, “Ni-NiO/Ni₃(BO₃)₂ 复合催化剂光催化还原 CO₂ 生成 CH₄ 的研究”, 第 2 届光功能材料与光电化学学术研讨会, 武汉 (2013.11.12-15)。
- 55 孙甲明, 侯琼琼, 刘犇, 邢晓东, “硅基电致发光器件的原子层尺度构建及其性能研究”, 第 8 届全国硅基光电子材料及器件研讨会, 杭州 (2013.6.19-22)。
- 56 刘犇, 邢晓东, 刘晓芳, 孙甲明, “氧化铟薄膜的原子层沉积生长及其性能研究”, 第 8 届全国硅基光电子材料及器件研讨会, 杭州 (2013.6.19-22)。

- 57 林妙玲, 赵丽娟, 兰子鉴, 常丽芬, 余华, “氟氧化物微晶玻璃散射效率的研究”, 第 17 届全国光散射学术会议, 西安 (2013.10.20-22)。
- 58 郭辉, 余华, 常丽芬等, “不同浓度稀土离子掺杂的微晶结构的研究”, 第 13 届全国发光光学学术会议, 南京 (2013.4.20-23)。
- 59 刘犇, 侯琼琼, 邢晓东, 刘晓芳, 孙甲明, “原子层沉积制备稀土 Tb 掺杂 SiO₂ MOS 器件及其电致发光性质的研究”, 第 13 届全国发光光学学术会议, 南京 (2013.4.20-23)。
- 60 邢晓东, 刘犇, 侯琼琼, 刘晓芳, 孙甲明, “Tb₂O₃ 稀土薄膜的原子层沉积生长及其发光性能研究”, 第 13 届全国发光光学学术会议, 南京 (2013.4.20-23)。
- 61 蔡孟强, 涂成厚, 李勇男, 王慧田, “矢量光场阵列的紧聚焦及其微加工特性”, 中国物理学会 2013 秋季物理学术会议, 厦门 (2013.9.12-15)。(光学分会张贴报告)
- 62 任志成, 李思崑, 李勇男, 涂成厚, 王慧田, “Pancharatnam-Berry phase related to vector beams bearing helical phase”, 中国物理学会 2013 秋季物理学术会议, 厦门(2013.9.12-15)。(光学分会张贴报告)

学术组织与期刊任职/Academic Service

国内学术组织任职/Service to the Domestic Professional Societies

序号	姓名	任职机构	职位	任期
1	许京军	中国高校知识产权研究会	副理事长	2008-
2	许京军	中国光学学会	理事	2006-
3	许京军	天津市光学学会	副理事长	2010-
4	许京军	天津市激光技术学会	副理事长	2010-
5	许京军	应用光学国家重点实验室	主任	2009-
6	孔勇发	中国材料研究学会青年工作委员会	理事	2011—2014
7	宋峰	天津市物理学会	常务理事兼秘书长	2008.7-
8	宋峰	天津市激光技术学会	副理事长	2009-2014
9	田建国	天津市光学学会	常务理事	
10	孙骞	天津市光电子学会	常委	2006-
11	张天浩	天津市照明学会	常务理事	2008-2012
12	宋峰	中国仪器仪表学会光电技术与系统成分会	常务理事	2007.6-
13	孔勇发	中国硅酸盐学会晶体生长与材料分会	理事	2012-2015
14	孙甲明	中国物理学会发光分会	委员	2010—2014
15	孙甲明	全国掺杂纳米发光学会	委员	2010—2014
16	孙骞	中国光学学会光电技术委员会	委员	2006-
17	徐晓轩	中国仪器仪表学会近红外光谱专业分会	专业委员	2013—2016
18	孙军	国家标准化管理委员会人工晶体标准化技术委员会	委员	2012.9—
19	宋峰	科学出版社	第二届教材建设委员会物理学科委员	2010.10-2015.12
20	宋峰	信息科学部	第五届专家咨询委员会学术秘书	2011.4-2014.4
21	宋峰	“军用固体激光技术”国防重点实验室学术委员会	委员	2007.8-
22	宋峰	全国中学生物理竞赛委员会	常委	2010.4-
23	徐晓轩	中国仪器仪表学会物理光学仪器专业委员会	专业委员	2013—2016

国内外期刊任职/Service to the Journals

序号	姓名	任职机构	职位	任期
1	许京军	journal of Optics	topic editor	
2	许京军	Frontiers of Physics in China	编委	2008-2011
3	宋 峰	Applied Optics	编委	2009-2012
4	吴强	Scientific Reports	Topic Editor	
5	许京军	《光学学报》	副主编	2008-
6	宋 峰	《大学物理》	副主编	2009.5-
7	许京军	《红外与毫米波学报》	编委	
8	许京军	《物理》	编委	2007-2011
9	许京军	《物理学进展》	编委	2009-2012
10	许京军	Chinese Physics Letters	编委	2009-
11	许京军	《中国光学与应用光学》	编委	2008-
12	孔勇发	《激光技术》	编委	2010-2013
13	孔勇发	《人工晶体学报》	编委	2012-2016
14	张国权	《激光技术》	编委	2011-2014
15	张国权	《激光与光电子学进展》	编委	2010-2013
16	宋 峰	《清洗世界》	编委	2011-

获奖情况/Awards & Honors

光场的空域、频域和时域调控
教育部自然科学奖一等奖
获得者：王慧田



系列实用高温稳定性电光调 Q 激光系统的开发与应用
天津市科学进步奖一等奖
获得者：孙军



等离子体激元超颖材料中的巨非线性旋光效应
中国激光杂志社“2012 中国光学重要成果”
获得者：任梦昕 Eric Plum 许京军 Nikolay Zheludev

获奖教师/Award for excellent teachers

第 12 届天津青年科技奖
入选者：刘智波 孙 军

获奖学生/Award for excellent students

2012 年度第九届王大珩高校学生光学奖：任梦昕
第八届饶毓泰基础光学奖优秀奖：任梦昕
中国物理学会 2013 秋季物理学术会议优秀张贴报告：蔡孟强
南开大学优秀博士培育基金：李思颀

研究生国家奖学金： 博士生：邢 飞 陈贵阳 李思颀
硕士生：郭 辉 戈 进 曹天祥

南开大学优秀研究生党员标兵：李思颀
天津市三好学生：李思颀
南开大学优秀毕业生：陈宗强 张文定
南开大学三好学生：李思颀

南开大学奖学金：
一等奖学金：蒋文帅 李健雄 刘 颖 陈庆全 潘岳
二等奖学金：于 萍 陈旭东 李志莉 陈战东 洪佩龙 孔令军
三等奖学金：马晨欣 赵 芳

宝钢教育奖学金：兰子鉴
光华奖学金：杨 明 潘崇培
合展励学金：于彦龙
周恩来奖学金：李思颀

学位论文/Dissertations

1. 博士学位论文 Dissertation for Doctoral Degree

- [1] 张文定, 光纤中基于声光作用的光调控及其应用; 导师: 张国权
- [2] 翟召辉, 掺镨硅酸钪晶体中基于电磁感应透明的光脉冲存储与处理; 导师: 张国权
- [3] 陈宗强, 基于表面等离激元的若干纳米光子学器件; 导师: 孙骞
- [4] 郝志强, 亚波长金属结构中基于表面等离激元的光场调控; 导师: 孙骞
- [5] 谢楠, 超快激光耦合扫描隧道显微镜的研制和功能化材料的研究; 导师: 孙骞
- [6] 吴限, 基于钙耗散结构的多细胞体系小胶质细胞间信号通讯的研究; 导师: 许京军
- [7] 应翠凤, 低阈值高效率光子晶体激光研究; 导师: 田建国
- [8] 闫卫国, 金属微纳米结构的制备及光学性能的研究; 导师: 田建国
- [9] 孔祥天, 亚衍射表面等离激元波导的光学性质; 导师: 田建国
- [10] 赵欣, 氧化石墨烯及其杂化材料超快光学非线性研究; 导师: 田建国
- [11] 王瑾, 基于导数全内反射法的组织复折射率测量及应用研究; 导师: 田建国
- [12] 杨阳, 艾利光束消逝场对米氏小球的操控与捕获; 导师: 臧维平
- [13] 杨熹, 光折变表面孤子的激发和调控及其应用研究; 导师: 张天浩
- [14] 刘艳玲, 金属纳米膜和颗粒结构对稀土离子掺杂液晶发光性质的影响; 导师: 宋峰
- [15] 于音, 白光 LED 用稀土离子掺杂荧光材料的制备及光谱性能研究; 导师: 宋峰
- [16] 赵红艳, 金属纳米颗粒对中药有机成分蛇床子素和稀土离子 (Eu^{3+}) 发光影响的研究; 导师: 宋峰
- [17] 田甜, 掺铈铈酸锂系列晶体的生长及其光折变性能的研究; 导师: 孔勇发
- [18] 裴子栋, 铈酸锂的载流子调控和 pn 结; 导师: 孔勇发
- [19] 徐纪华, ABA 型三嵌段共聚物刷在选择性溶剂中自组装行为的模拟退火研究; 导师: 李宝会
- [20] 张新星, 离子液体及其极性溶剂混合液的溶剂化动力学研究; 导师: 赵丽娟
- [21] 张鹏, 新型高效半导体光催化材料的制备及光催化机理研究; 导师: 姚江宏
- [22] 娄凯, 飞秒矢量光场空间调控及其在微加工中的应用; 导师: 王慧田

2. 硕士学位论文 Dissertation for Master Degree

- [1] 张永哲, 铈酸锂晶体紫外光辅助畴反转研究; 导师: 张国权
- [2] 殷毅, 无序二维光子晶体薄板的透射性质研究; 导师: 张国权
- [3] 孙哲, Airy 光束的线性及非线性调控; 导师: 楼慈波
- [4] 马腾飞, 新型光诱导光子晶格的制备及离散孤子态的研究; 导师: 楼慈波
- [5] 马寅星, 基于黑硅的光电二极管的研究; 导师: 吴强
- [6] 易三铭, 激光直写 MTMO 掩模机理研究; 导师: 张心正
- [7] 云志强, 飞秒激光直写微纳加工研究, 导师: 张心正门双仁, 压缩感知在生物传感中的应用研究; 导师: 周文远
- [8] 周玉波, 偏振模色散及其补偿研究; 导师: 田建国
- [9] 马跃, 基于 MOF 的空间分辨免疫荧光检测系统; 导师: 田建国

- [10] 高原, 非线性随机系统与心率波动调控机制的研究; 导师: 张天浩
- [11] 彭秋明, 光折变表面波激发; 导师: 张天浩
- [12] 王秋明, 基于结构光的乳房三维形貌测量系统; 导师: 张天浩
- [13] 张阳, 光折变表面离散孤子研究; 导师: 张天浩
- [14] 张俊, 基于线扫描的物体表面重构; 导师: 宋峰
- [15] 王津津, 非线性光学自聚焦技术探测强背景噪声下的隐匿信号的研究; 导师: 宋峰
- [16] 周亮, 加速度传感器应用于步态判别和计步; 导师: 徐晓轩
- [17] 田万辉, 石墨烯与石墨炔体系振动性质; 导师: 徐晓轩
- [18] 郑守君; 铈酸锂铁电畴微结构制备及其性能研究; 导师: 孔勇发
- [19] 黄明; 掺钨铈酸锂晶体; 导师: 孔勇发
- [20] 乔晓龙, 嵌段共聚物受限在纳米球内的自组装行为的模拟研究; 导师: 李宝会
- [21] 谢桂娟, 6-硝基-BIPS 复合材料的制备及光学非线性研究, 导师: 曹亚安
- [22] 甄彦赞, 铈酸锂与掺杂二氧化钛复合薄膜的光折变性能研究, 导师: 曹亚安
- [23] 刘艳, 重金属对掺铒氟氧化物玻璃及微晶玻璃结构及近红外发光影响的研究; 导师: 赵丽娟
- [24] 侯琼琼, 原子层沉积方法制备稀土 Gd 掺杂 SiO_2 薄膜电致发光器件; 导师: 孙甲明
- [25] 王肖珩, 超声雾化气相沉积生长的 $\text{Zn}_{1-x}\text{Mg}_x\text{O}$ 薄膜性质的研究; 导师: 孙甲明
- [26] 靳亚粉, 利用溶胶-凝胶法制备稀土掺杂 SiO_2 发光材料研究; 导师: 孙甲明
- [27] 卢旭岑, ZnO 纳米结构的可控性制备及形成机理研究; 导师: 姚江宏
- [28] 张菁, 大面积、高质量二硫化钼二维结构的制备及其场效应晶体管器件; 导师: 姚江宏
- [29] 刘畅, 电解法制备纳米 Al_2O_3 粉体的研究; 导师: 舒永春
- [30] 贾翠乐, 染料敏化镍掺杂、硅掺杂二氧化钛太阳能电池的性能研究; 导师: 皮彪
- [31] 张华, 同成分铈酸锂晶体的扩散研究; 导师: 张玲
- [32] 杨金凤, 高质量近化学计量比铈酸锂晶体制备的研究; 导师: 黄存新
- [33] 李芳, 锶铈硼体系新化合物的探索及物性研究; 导师: 武莉
- [34] 张芳馨, 铈硼酸盐体系新化合物的探索及物性研究; 导师: 武莉